



Norwegian University of
Science and Technology

Vertical earthquake response of a Submerged Floating Tunnel including Sequake loading

Lars Amund Rudi Nerland
Matias Linde Røsvik

Civil and Environmental Engineering
Submission date: June 2017
Supervisor: Amir Kaynia, KT

Norwegian University of Science and Technology
Department of Structural Engineering



MASTER THESIS 2017

SUBJECT AREA: Earthquake engineering	DATE: 11. June 2017	NO. OF PAGES: 16 + 112 + 15
---	------------------------	--------------------------------

TITLE:

Vertical earthquake response of a Submerged Floating Tunnel including Seaquake loading

Vertikal jordskjelvrespons av Neddykket Rørbru inkludert last fra sjøskjelv

BY:

Matias Linde Røsvik
Lars Amund Rudi Nerland



SUMMARY:

This MS thesis investigates vertical seismic response in time domain on the proposed concept for a SFT with vertical tension leg design located at Bjørnafjorden. A 3D beam model is employed to conduct seismic analysis on the SFT by applying three vertical earthquake acceleration time series. The hydrodynamic properties of the SFT is applied according to numerical results from an analysis in the hydrodynamic software WADAM. A simplified sensitivity study is conducted on relevant effects for the structural response. Emphasis is given to investigate the load effect known as seaquake, originating from the propagation of primary waves in water due to seabed ground motion. Seaquake loading is calculated in a decoupled approach both analytically in frequency domain and numerically in time domain through a finite element analysis in ABAQUS.

The results show that seaquake loading results in only a modest increase in peak tether stresses, but a large amplification in accelerations. The seaquake effect is still somewhat uncertain as no structural coupling is introduced. The results show that vertical earthquakes of 475-year return period is not of critical importance to the SFT, while considering earthquakes of 10 000-year return period may lead to a too low safety margin for the tether stresses in the stiffest tether group.

RESPONSIBLE TEACHER: Prof. Amir M. Kaynia

SUPERVISOR(S): Prof. Amir M. Kaynia

CARRIED OUT AT: Department of Structural Engineering, NTNU

Preface

This thesis is the result of 20 weeks of work and concludes our Masters degree in Structural Engineering at Norwegian University of Science and Technology (NTNU). The thesis investigates effects of vertical earthquake ground motion on a submerged floating tunnel (SFT) proposal for the site of Bjørnafjorden. No SFT has yet been constructed, therefore getting insight on the structural concept and perhaps contribute to increasing knowledge on its robustness was inspirational for us. There seems to be a lack of research on how the seaquake phenomenon affects submerged structures, which sparked our interest to expanding our knowledge into a field in fluid dynamics relatively unknown to us beforehand as structural engineers.

We would like to thank our supervisor prof. Amir M. Kaynia for all his engagement, support and guidance in our work during the semester. Through inspiring lectures in earthquake design in a course in advanced structural dynamics he sparked our interest in earthquake engineering, which was decisive for the selection of our Master Thesis. He showed genuine interest in our thesis, and gave us valuable feedback even way past normal working hours. His guidance and advice was essential for the development of the thesis, and his help is gratefully acknowledged.

The numerical modelling of the seaquake phenomena proved more difficult than expected. A high amount of time and resources was spent developing and troubleshooting the numerical model of the primary waves in water. When the model finally behaved reasonable, time was too scarce to extend the model to the desired extent.

Throughout the whole semester, we have had great support and valuable feedback from prof. Svein N. Remseth. His advice in the development and troubleshooting of the numerical seaquake model has been essential in developing the model and interpreting results throughout the whole process. Much gratitude is also directed to Tore H. Søreide at Dr. Techn. Olav Olsen AS for the initiative of addressing the topic of vertical earthquake excitations on SFT as a master thesis, and all valuable follow-up and providing us with the design basis of the proposed SFT at the site of Bjørnafjorden. We also received highly valuable input from Associate Professor Erin Bachynski in the field of hydrodynamics, which provided necessary insight in evaluating the output from the investigation of the hydrodynamic properties of the SFT.

Trondheim, 11.06.2017

Matias Linde Røsvik and Lars Amund Rudi Nerland

Abstract

Norwegian Transport Plan for 2014-2023 has ambitions to make E39 along the Norwegian west coast from Kristiansand to Trondheim ferry free within 20 years. To make this possible, long and deep fjords must be crossed, where ordinary bridge technology is unsuitable. A submerged floating tunnel (SFT) is one of the relevant solution concepts. The main objective of this MS thesis is to investigate vertical seismic response in time domain on the proposed concept for a horizontally curved SFT with vertical tension leg design located at Bjørnafjorden. This fjord crossing is located close to the peak of the seismic hazard map for southern Norway.

The SFT is modelled as a 2D planar and 3D beam model with horizontal curvature in the finite element program ABAQUS, with equivalent properties extracted from a 3D shell model of the bridge girder. The response of the SFT is conducted on the 3D beam model, and excited with three earthquake acceleration time series. The acceleration time series originate from the vertical component of the 1985 Nahanni, 1976 Friuli and 1940 Imperial Valley earthquakes modified to match the EC8 design spectrum, and normalized to local peak ground acceleration. The hydrodynamic properties of the SFT in the beam models is applied according to numerical results in the hydrodynamic analysis software WADAM. A Simplified sensitivity study is conducted on the effects of structural damping, torsional representation, local tether stiffness and the earthquake wave passage effect. The results show torsional stiffness representation gives negligible effect on the peak response, while structural damping and the wave passage effect results in modest alterations of peak stresses in the tethers. It is also shown that reducing stiffness of selected tether groups can drastically alter the peak tether stresses for the SFT when excited from earthquakes.

Emphasis is given to investigate the load effect known as seaquake on a SFT, originating from the propagation of primary waves in water due to seabed ground motion. Seaquake loading is calculated in a decoupled approach both analytically in frequency domain and numerically in time domain through a finite element analysis in ABAQUS with acoustic elements. Seaquake loading is applied to the 3D beam model of the SFT for response analysis. Seaquake loading results in only a modest increase in peak tether stresses, but a large amplification in accelerations. The results differ from previous studies that have indicated large tether stresses may arise from a SFT subjected to seaquake. The seaquake effect is still somewhat uncertain as no structural coupling is introduced.

When considering earthquake at Bjørnafjorden with 10 000-year return period, the stresses in the stiffest tether groups are shown to come close to compression. As no other dynamic loads are considered this may represent a too low safety margin, suggesting that the response from earthquake in the stiffest tethers need to be addressed in design. When earthquakes with 475-year return period are considered, the structural response in terms of moments and stresses in the bridge girder are small and the stress in the tethers are moderate, thus earthquakes of this magnitude will not be of critical importance to the given SFT.

Sammendrag

Norsk Transport for 2014-2023 har ambisjoner om å gjøre E39 langs den norske vestkysten fra Kristiansand til Trondheim fergefri innen 20 år. For å gjøre dette mulig, må lange og dype fjorder krysses, hvor vanlig bruteknologi er uegnet. Neddykket rørbru er en av de relevante løsningskonseptene. Hovedformålet med denne master-avhandlingen er å undersøke vertikal seismisk respons i tidsdomene på det foreslåtte konseptet for en horisontalt kurvet rørbru med vertikal spennstagforankring ved Bjørnafjorden. Denne fjordkryssingen ligger nær den mest aktive seismiske sonen i Sør-Norge.

Rørbruen er modellert som en 2D og 3D-bjelkemodell med horisontal krumning i elementmetodeprogrammet ABAQUS, med ekvivalente egenskaper hentet fra en 3D-skallmodell av brobjelken i samme program. Responsen fra rørbruen er beregnet fra 3D-bjelkemodellen eksitert med tre jordskjelv-akselerasjonstidsserier. Akselerasjonstidsseriene stammer fra den vertikale komponenten av henholdsvis 1985 Nahanni, 1976 Friuli og 1940 Imperial Valley jordskjelvene, modifisert for å passe EC8 designspekteret, og normalisert til lokal maksimal grunnakselerasjon. De hydrodynamiske egenskapene til rørbruen i bjelkemodellene er påført i henhold til numeriske resultater fra det hydrodynamiske analyseprogrammet WADAM. Et forenklet følsomhetsstudie er utført på virkningen av konstruksjonsdemping, torsjonsrepresentasjon, lokal strekkstagsstivhet og bølgeforplantningseffekt av jordskjelvbølger. Resultatene viser at torsjonsrepresentasjon gir ubetydelig effekt på maksimalrespons, mens konstruksjonsdemping og bølgeforplantnings-effekten resulterer i moderate endringer av toppspenninger i strekkstagene. Det er også vist at redusert stivhet av utvalgte staggrupper kan drastisk endre maksimalspenningen i strekkstagene for rørbruen når den er påkjent av jordskjelv.

Det er lagt vekt på å undersøke lasteffekten kjent som sjøskjelv (seaquake) på en rørbru, som stammer fra forplantning av trykkbølger i vann på grunn av bevegelse i havbunnen fra jordskjelv. Sjøskjelvlasten er beregnet fra en ukoblet fremgangsmåte både analytisk i frekvensdomene og numerisk i tidsdomene gjennom en elementanalyse i ABAQUS med akustiske elementer. Sjøskjelvlasten er påsatt 3D-bjelkemodellen av rørbruen for responsanalyse. Sjøskjelvet resulterer i kun en moderat økning av maksimalspenningen i strekkstagene, men en stor forsterkning i akselerasjoner. Resultatene avviker fra tidligere studier som har indikert at sjøskjelv kan føre til store stagspenninger på rørbruer. Sjøskjelveffekten er fortsatt noe usikker da ingen strukturell kobling er introdusert i modellene.

Når man vurderer jordskjelv i Bjørnafjorden med 10 000-års returperiode, er spenningene i de stiveste strekkstaggruppene vist å komme nær trykkspenninger. Da ingen andre dynamiske belastninger er vurdert, kan dette utgjøre en for lav sikkerhetsmargin, noe som tyder på at respons i de stiveste strekkstagene fra jordskjelv bør adresseres i design. Ved vurdering av jordskjelv med 475-års returperiode er konstruksjonsresponsen i form av momenter og spenninger i brubjelken liten, og spenningen i stagene kun moderate. Jordskjelv av denne størrelsesorden vil derfor ikke være av kritisk betydning for den gitte rørbruen.

Contents

1	Introduction	1
1.1	Motivation for research	1
1.2	The SFT concept.....	3
1.2.1	The tension leg design.....	4
1.2.2	The pontoon design	4
1.2.3	Bridge girder	5
1.3	Earthquake induced fluid motion.....	6
1.3.1	Seaquakes	6
1.4	State of research for SFTs and seismic effects	7
1.4.1	SFT Hydrodynamic properties	7
1.4.2	Seaquake on large floating structures.....	9
1.4.3	Seaquake response of SFT.....	11
1.4.4	Summary of research.....	13
2	Theoretical background.....	15
2.1	Earthquakes.....	15
2.1.1	Natural earthquakes.....	15
2.1.2	Earthquake excitations.....	17
2.1.3	Eurocode 8: Design of structures for earthquake resistance	19
2.2	Fluid modelling.....	20
2.2.1	Computational Fluid Dynamics.....	20
2.2.2	Potential Flow	21
2.2.3	Numerical solution of potential flow theory	23
2.2.4	Analytical solution of resonance in water from pressure waves.....	26
2.2.5	Numerical solution of acoustic problems in ABAQUS.....	29
2.2.6	Impedance and reflection coefficient	31
2.3	Fluid structure effects.....	32
2.3.1	Added mass and structural eigenmodes	32
2.3.2	Hydrodynamic damping	34
2.3.3	Morison equation.....	35

3	Case study Bjørnafjorden.....	37
3.1	Design basis.....	37
3.2	Earthquake time series.....	44
3.2.1	Strong motion Friuli.....	47
3.3	Modelling strategy	48
4	WADAM modelling	49
4.1	CAD and meshing.....	49
4.1.1	Morison beam model	49
4.1.2	Panel Model.....	50
4.2	WADAM results.....	51
5	ABAQUS Acoustic Modelling.....	53
5.1	Developing acoustic model	53
6	ABAQUS Modelling.....	59
6.1	Modelling equivalent stiffness.....	59
6.1.1	The 3D shell element model.....	59
6.1.2	Equivalent Lateral stiffness	61
6.1.3	Equivalent torsional stiffness.....	62
6.1.4	Validating equivalent stiffness.....	64
6.2	Beam models.....	66
6.2.1	Eigenmode analysis	67
6.2.2	Applying structural damping.....	72
6.3	Time series response analyses	73
6.3.1	Spatial response of the initial model.....	74
6.3.2	Section response of the initial model.....	76
6.3.3	Behavior in the stiffest tether.....	79
6.4	Sensitivity study	81
6.4.1	Effect of Damping.....	81
6.4.2	Torsional effects.....	83
6.4.3	Earthquake wave passage effect	84
6.4.4	Effect of softer tethers.....	85
6.5	Applying seaquake.....	86
6.5.1	Analytical seaquake from frequency domain.....	87
6.5.2	Abaqus Acoustic time-domain pressure loading.....	89
6.5.3	Global response of seaquake strong motion Friuli time series.....	91
6.5.4	Global response of full length seaquake loading	93
6.5.5	Earthquake with higher return period	95

7	Discussion	97
7.1	Hydrodynamic properties of SFT	97
7.1.1	Added mass	97
7.1.2	Hydrodynamic damping	98
7.2	Eigenmodes	99
7.3	Seismic response of global beam model	100
7.4	Sensitivity study	102
7.4.1	Damping sensitivity	102
7.4.2	Torsional effects	102
7.4.3	Earthquake wave passage effect	103
7.4.4	Effect of softer tethers	103
7.5	Sequake	104
7.5.1	Numerical behavior	104
7.5.2	Sequake uncertainties	104
7.5.3	Comparison between analytical and time domain seaquake	106
7.5.4	SFT response from seaquake loading	106
7.6	Earthquake with high return period	108
8	Conclusions	109
8.1	Remarks and recommendations for further research	110
	References	111
	Appendix	A1

List of symbols

χ	Volumetric drag in acoustic elements
δ_{ij}	Kronecker delta function
ε	Strain
ε_v	Volumetric strain
Φ	Potential velocity function
γ	Structural importance class in EC8
ρ	Density
τ	Stress in Navier-Stokes equations
ν	Kinematic viscosity
ω	Angular frequency
ξ	Critical damping ratio
C	Damping
c	Primary wave velocity
C_D	Damping coefficient
C_M	Added mass coefficient
E	Youngs modulus
e_0	Total energy
F	Force
f	Frequency
H	Height
$H(\omega)$	Frequency response transfer function
i	Imaginary unit
I	Second moment of inertia
K	Stiffness
k	Wave number
K_s	Bulk modulus
L	Length
M	Mass
M	Moment
p	Pressure
q	Distributed load
Re	Reynolds number
t	Time
u	Position
\ddot{u}	Acceleration
\dot{u}	Velocity
V	Volume
X_i	Spatial coordinates

Abbreviations

ALS	Accidental Limit State
C/C	Center to center
CAD	Computer-aided design
CFD	Computational fluid dynamics
DNV	Det Norske Veritas
EC8	Eurocode 8: Design of structures for earthquake resistance
FEA	Finite Element Analysis
FE	Finite Element
FFT	Fast Fourier Transform
FSI	Fluid Structure Interaction
LAT	Lowest Astronomical Tide
MDOF	Multi Degree of Freedom
NBS	Norwegian Concil for Building Standardization
NPRA	Norwegian Public Roads Administration
NSE	Navier-Stokes equations
OO	Dr. techn. Olav Olsen AS
PGA	Peak Ground Acceleration
P-wave	Primary Wave
SDOF	Single Degree of Freedom
SFT	Submerged Floating Tunnel
SH-wave	Secondary Horizontal Wave
SRSS	Square root of the sum of squares
SSI	Soil Structure Interaction
SV-wave	Secondary Vertical Wave
S-wave	Secondary Wave
TLP	Tension Leg Platform
ULS	Ultimate Limit State

1 Introduction

1.1 Motivation for research

Norwegian Public Road Association (NPRA) has plans for a ferry free E39 along the west coast of Norway between Kristiansand and Trondheim. To make this project possible, long span bridges crossing deep fjords is necessary, where ordinary bridge technology is unsuitable, and underwater rock tunnels are unpractical due to the sea depth. A submerged floating tunnel (SFT) is a concept for crossing of water that has not yet been implemented anywhere, and is one of the concepts considered for crossing several of these fjords (Dunham, 2016).

Seven fjord crossings have lengths of more than 1300 meter and all of these have depths of more than 400 meters. Among these are Bjørnafjorden and Sognefjorden with lengths of 5000 m, and 3700 m respectively. For the most prestigious crossing, namely Sognefjorden, NPRA has a requirement of a 400 m wide span, 70 m sailing height, and 20 m draft. This could be a challenge for cable- and floating concepts. A feasibility study has however shown both a suspension bridge, a floating bridge, and a SFT solution to be possible (NPRA, 2012).

According to the seismic design code EC8, all bridges in seismic class IV should be evaluated with respect to earthquake response. For the case of building an SFT in high seismic risk zones knowledge about the structural behavior of SFTs exposed to seismic excitation is necessary. This master thesis will therefore focus on investigating dynamic effects from vertical seismic loading on a SFT. With regards to Bjørnafjorden, the NPRA has chosen to not go for the SFT concept, while different floating-, suspension- and cable-stayed bridge solutions will be further assessed (NPRA, 2016). However, since there is a comprehensive feasibility study with design basis and plans for the location of Bjørnafjorden, this master thesis will use these available data provided by Dr. Techn. Olav Olsen (OO) to study effects of vertical earthquakes on a SFT bridge.

According to NORSAR, mainland Norway is not very prone to earthquakes, however it is the area in northern Europe with the highest frequency of earthquakes (Norsar, 2016). To some extent there has been damages from earthquakes the past couple of hundred years, like the 1904 earthquake of magnitude 5.4 south of Oslo, where there were reports of some damages to buildings. There were also reports of disturbances on the water surface in the fjord felt in boats during the earthquake, most likely originating from the seaquake effect. Mainland Norway is not located on any plate boundaries, and the release of stresses from the post-glacial rebound seem to be of most significance for earthquakes in Norway. In Nordland the land rise is still at about 4 mm each year, building up significant tension in the earth crust. The two most active earthquake-zones in Norway is in Nordland and the west coast. This trend is clearly visible in Figure 1.1-1 where recorded earthquakes in Norway between 1979 and 2012 is shown. The project of ferry free E39 has several ambitious fjord crossings on the west coast, and in the heart of this coast lies Nordfjord. Here, there has been recorded two medium sized earthquakes in recent times. One in 1955 with a magnitude of 5.2 and another one in 1989 with magnitude of 5.1 (Bungum, 2017). In the earthquake zone map for return period of 475 years in the Norwegian annex EC8, the highest design values of earthquakes are in this area, slightly north of Bjørnafjorden. The horizontal acceleration has a value of $a_{g,40Hz}$ of 1 m/s^2 , while for Bjørnafjorden particularly, the value is roughly 0.9 m/s^2 (Standard Norge). The earthquake response of SFTs have been studied to some extent. However, there seems to be limited research on both the generation mechanism of seaquakes and the dynamic response of SFTs when subjected to seaquake loading.

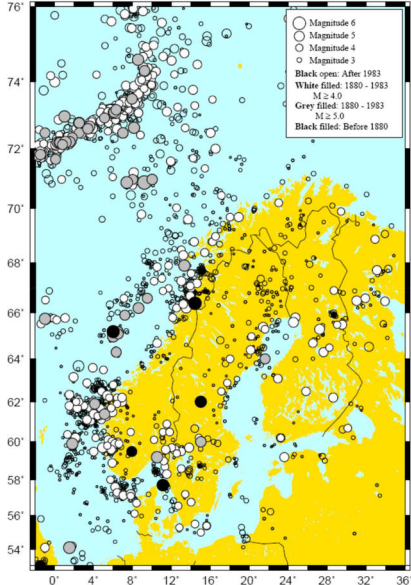


Figure 1.1-1: Earthquakes in Norway and surrounding areas from 1880 to 2012 (Norsar, 2016).

1.2 The SFT concept

A SFT is in principle one or multiple submerged tubes of desired shape, either suitably anchored to the seabed or to floating pontoons. An illustration for a tension leg design and a pontoon design is shown in Figure 1.2-1. Much like a traditional floating bridge, a SFT exploits the benefits of buoyancy for load carrying. Compared to a traditional floating bridge, by submerging the bridge, it will be less of an obstacle for ship traffic at the surface, as well as avoiding the most severe hydrodynamic loads from wind and surface waves. It could however be prone to different load cases than other bridges. Hydrodynamic forces from currents may induce large response from effects such as vortex induced vibrations, and for the case of Bjørnafjorden even impact loads from submarines are considered.

Since a SFT is completely submerged, the effect of the surrounding water on the structure has to be thoroughly investigated. In order to be able to evaluate the possible problems related to earthquake loading, it is necessary to have some theoretical background regarding the utilized theory on the structural behavior, different effects from the surrounding water, as well as the nature of earthquake excitations.

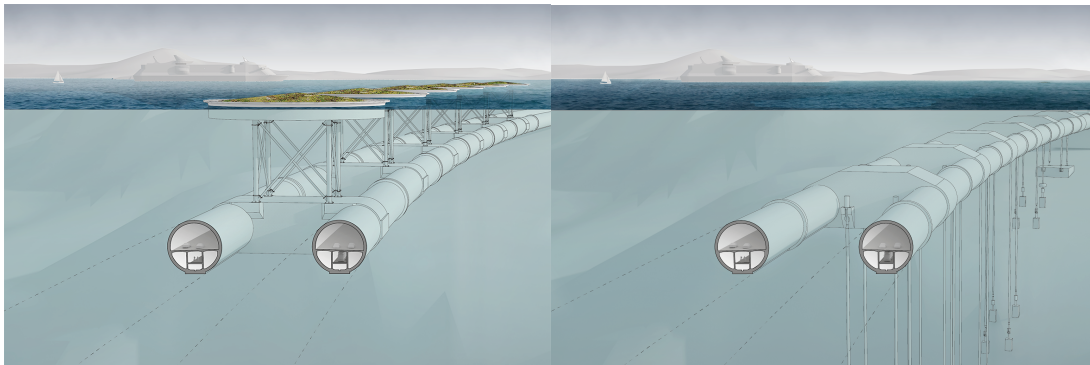


Figure 1.2-1: Illustrations of the pontoon solution and tension leg solution (NPRA).

1.2.1 The tension leg design

One of the proposals for the crossing Bjørnafjorden feature anchoring the SFT to the seabed by means of tethers, similar to the ones used for tension leg platforms such as Heidrun illustrated in Figure 1.2-2. These tension legs can be replaced after their service time, and the structure should withstand the extra forces due to this operation.

The SFT is designed with a net buoyancy, generating tension in the tethers. Several different anchoring layouts have been proposed for SFTs, such as inclined tethers or vertical tethers, as well as different combinations of these. From pure geometric considerations, vertical tethers will give higher stiffness to vertical motion, while the contribution to lateral stiffness is negligible. Inclined tethers contribute to the lateral stiffness of the bridge, however, at the cost of decreasing the vertical stiffness contribution. When it comes to earthquakes, vertical tethers will be able to transmit loads from vertical ground excitations, while the horizontal ground motion will have negligible impact on the tunnel except from the excitation at the two ends at shore. For inclined tethers, both vertical and horizontal ground motion will invoke forces to the SFT. Anchoring the SFT to the seabed also comes with the disadvantage of the anchoring system being prone to several different challenges, for instance underwater landslides which may cause dynamic impact loads on the anchoring system. High stress oscillations in the tethers may result in several undesirable effects such as fatigue, and should be considered for this design.

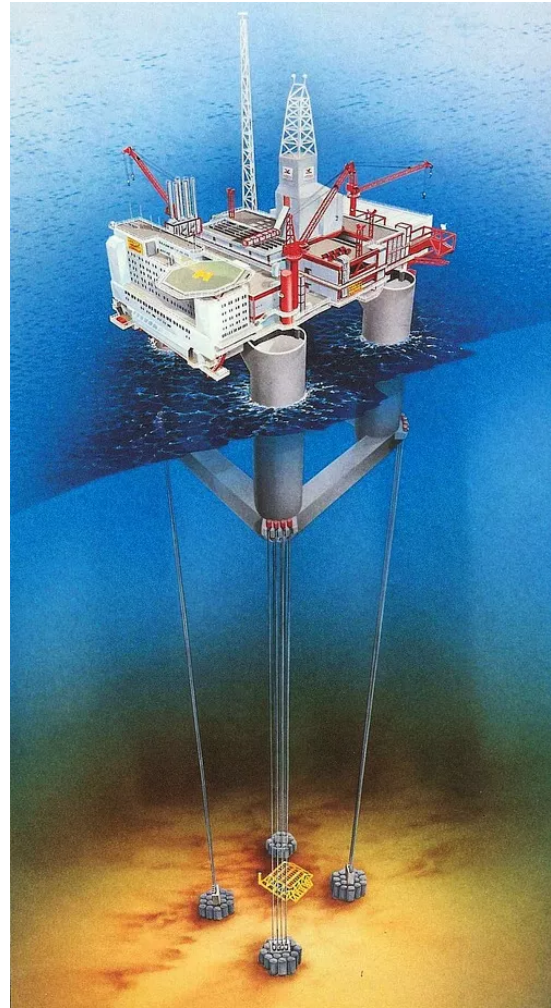


Figure 1.2-2: Illustration of the tension leg platform Heidrun located at the Halten bank off the coast of mid-Norway (Norsk Oljemuseum, 2017).

1.2.2 The pontoon design

In the pontoon solution, the SFT has slight negative buoyancy, and is anchored to the floating pontoons. In this case, the pontoons provide the necessary additional vertical load carrying capacity. As for the case of only vertical tethers, the pontoon solution yields negligible contribution to lateral stiffness, which has to be provided by the bridge girder itself. By not being connected to the seabed, the bridge girder, except for the ends, is isolated from ground motion and underwater landslides. However, as the pontoons are floating at the surface, these are susceptible to for instance ship-impacts, and are prone to higher hydrodynamic loads from waves and wind, as well as seaquakes. The effects of ship-impact are proposed solved by having a weak link between the pontoon and the bridge, as well as designing the bridge operating with the case of a missing pontoon. This design is not evaluated in this thesis.

1.2.3 Bridge girder

The bridge girder may have different shapes. The most common solutions are either a straight or laterally curved bridge. By using a curved bridge girder with fixed ends, the lateral stiffness is increased due to lateral loads being transferred to axial forces in the girder, instead of pure bending moment as in a straight girder. This is analogous to vertical loads in arch bridges. Some designs may require significant lateral stiffness from the bridge girder, requiring a high second moment of inertia. The lateral stiffness may be increased by having a wide bridge girder, for instance by using two separate tubes, and ensuring interaction between them by connecting the tubes with some sort of truss system.

The type of end anchoring will impact the structural behavior of the SFT. For the solution proposed by OO both ends are assumed to be fixed. In the case of a SFT being used in an area with high seismic activity, it may be necessary to isolate the supports from the earth movement by means of some sort of energy dissipation device.

1.3 Earthquake induced fluid motion

The effect of ground motion from earthquakes may induce different excitations of water. Motion of the seabed will induce motions in the water above. In enclosed reservoirs, a vertical resonant behavior called sloshing may be observed. When induced by earthquakes, this is called seismic seiches, and is a standing gravity wave phenomena, similar to the motion in a cup of coffee when shaken. Observations of norwegian lakes and fjords in the time periods of certain earthquakes, such as the 1755 Lisbon earthquake, and the 1950 Assam earthquake, indicate that seismic seiches have occurred in Norway with estimated amplitudes up to 1 m according to eye witnesses (Norwegian Council for Building Standardization (NBS), 1998). Due to the SFT being completely submerged, such small amplitudes of seiches are hard to envision giving significant vertical loads on the SFT, and seismic seiches will therefore not be considered further in this thesis. Another, and perhaps the most well-known earthquake induced effect in water, is tsunamis, which is a horizontal wave effect. It is worth noting that tsunamis may be produced from rockslides in enclosed water reservoirs such as fjords, and this may thus be of design concern for the bridges in some of the fjord crossings. Regardless, tsunamis, will not be considered in this thesis. When the seabed is excited from an earthquake, however, a less known effect of seaquake, also called sea shock, may occur. This effect is due to vertical pressure waves propagating through the water from vertical motion at the seabed.

1.3.1 Seaquakes

Fluids such as water are incapable of transferring shear forces, due to low viscosity, so when the seabed is excited from an earthquake, it may only generate compression waves propagating through the fluid. The pressure wave effect in the fluid from earthquake motions at the seabed are from here on referred to as seaquake. Because of the relatively high bulk modulus of water, at approximately 2.15 GPa, very large pressure is needed to change the volume of the fluid significantly. As a result, the motion of the water surface generated by an earthquake on the seabed may be hard to observe, as the surface motion can be dominated by other surface waves such as wind generated waves. However, this does not mean that the seaquake does not affect floating structures. There are several examples of boats experiencing these pressure waves from seaquakes. The most notable may be the Norwegian ship 'MT Ida Knudsen' which suffered severe damage to its hull and machinery to such extent that it had to be condemned and rebuilt after experiencing what was likely a seaquake off the coast of Portugal in 1969. At the time of the event, the boat was located only 20 km away from the epicenter of a 7.8 magnitude earthquake off the coast near Gibraltar (Ambraseys, 1985). Also, several ferry boats in the Osaka Bay during the Kobe earthquake in Japan 1995 reported experiencing two separate violent vertical shocks during the earthquake. At the same event ultrasonic wave height meters showed tsunamis of only about 5 cm (Uenishi & Sakurai, 2013). This indicates that the effect of seaquakes is different from that of a tsunami, and that it has the ability to induce vertical dynamic response in floating structures. The seaquake phenomenon is commonly observed close to the epicenter, and has also been reported at more modest sized earthquakes. Reports from the 1904 Oslofjord earthquake state the disruption of the sea surface, as if it was boiling, and the quake was felt aboard ships, like they were touching the bottom (Norwegian Council for Building Standardization (NBS), 1998). For a SFT, these shock loads may be of some concern in seismic response analysis, especially if the SFT is located close to a fault line.

1.4 State of research for SFTs and seismic effects

The SFT concept was considered in Norway in the early 80s for the crossing at the fjord Høgsfjorden. In 1998 this concept got an approval as a technical solution for this project, but was not selected as the final solution (NPRA, 2012). In other countries several SFTs has been proposed, including crossing the Messina Strait (Martire, Faggiano, Mazzolani, Zollo, & Stabile, 2010), Baja California (Faggiano, Panduro, Rosas, & Mazzolani, 2016), and the Qiongzhou strait (Shengzhong et.al., 2016), all of which are located in high seismicity zones. It is evident that there is interest in research within the seismic behavior of SFTs.

Some research on the effect of seaquake exists, it appears quite a lot have been done in the field of large floating structures, and much less on submerged structures, especially the SFT concept.

1.4.1 SFT Hydrodynamic properties

Paik et. al. considered added mass and damping on a SFT. The study used hydrodynamic coefficients, obtained from solving a 2D diffraction problem, on a 3D structural analysis of the SFT in the time domain. The article concludes that the effect of depth affects radiation damping to a greater extent than added mass (Paik, Oh, Kwon, & Chang, 2004). The effect of depths on radiation damping from the article is given in Figure 1.4-1, where it is clearly illustrated that increasing the submerged depth reduces the frequency at which the peak for radiation damping is located. It is also evident that the radiation damping goes towards zero for very low or very high frequencies. The depth dependence of added mass is given in Figure 1.4-2, where the frequency dependency decreases with increasing depth, and for a high frequency goes towards a constant value. The studied frequency of external wave ranges from 0.05 to 5.0 rad/sec. Remark the coefficients presented in Figure 1.4-1 and Figure 1.4-2 are apparently not given as ratios.

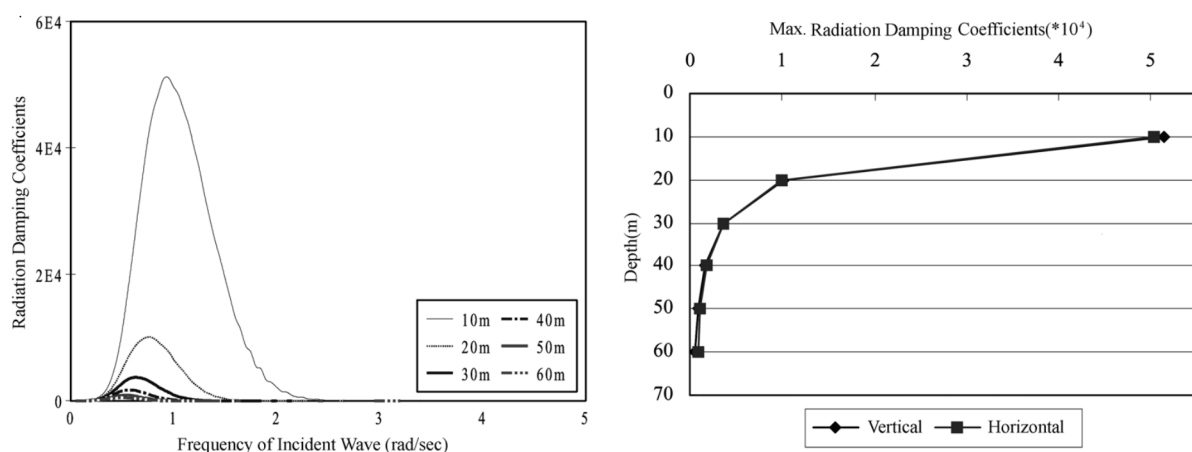


Figure 1.4-1: Horizontal radiation damping with respect of frequency (left) and maximum values of radiation damping with depth (right) (Paik et al., 2004).

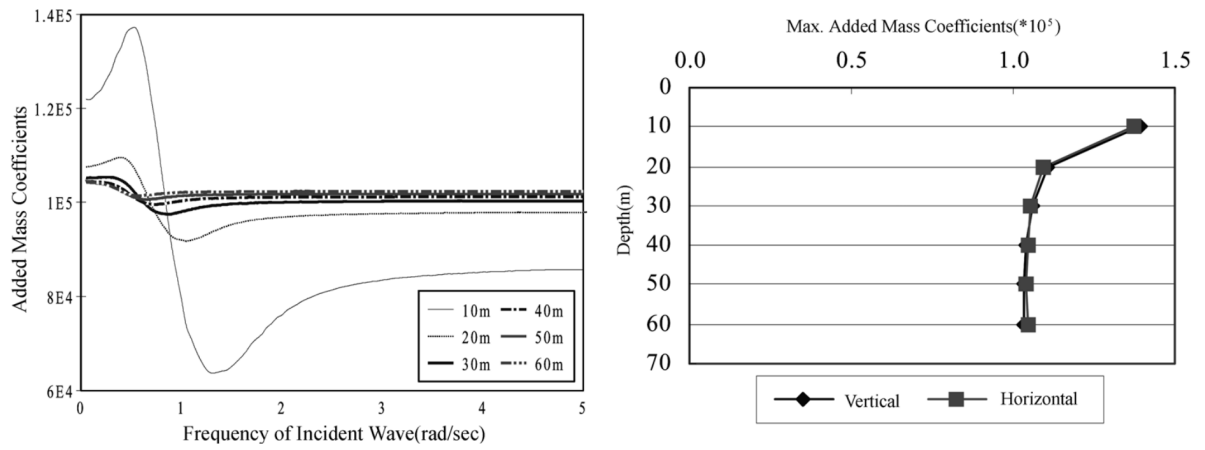


Figure 1.4-2: Horizontal added mass with respect of frequency (left) and added mass coefficient with depth (right) (Paik et al., 2004).

1.4.2 Seaquake on large floating structures

Hamamoto studied the response on a large circular floating island from both wind waves and seaquake. The seaquake loading was modeled as a stationary random process, although earthquake ground motion is in general non-stationary. The hydrodynamic pressure from seaquake was calculated through potential theory. For long return period, it is concluded that seaquake response for bending moments becomes significantly larger than wind wave response. It is concluded that seaquakes are occasionally amplified by the mooring system. The seaquake excites higher order modes of vibration than wind forces do. Figure 1.4-3 show a stochastic power spectral density function of external loads from seaquakes (Hamamoto, 1995).

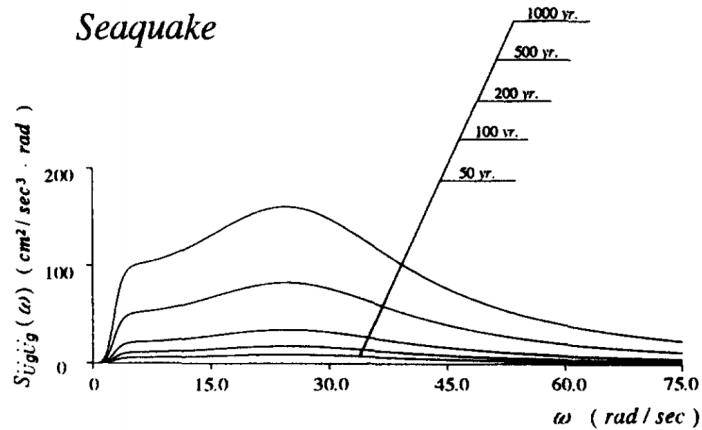


Figure 1.4-3: Stochastic power spectral density function of external loads from seaquakes (Hamamoto, 1995).

A more extensive study was conducted on large floating structures in both frequency and time domain (Inoue, Murai, Noma, & Aoki, 2002). The time domain analysis was studied in the FEA software ANSYS by assuming acoustic wave propagation. An analysis was done in 2D of a seabed of width 10 km, with the excitation being a harmonically oscillating point source of width 100 m. Both horizontal and moderately inclined seabed was analyzed. The wave propagation results for inclined seabed is shown in Figure 1.4-4. It was concluded that pressure waves propagate towards deeper waters. The study also included a time-domain simulation of the Tokachi-oki earthquake and the pressure loading on a large floating structure. It was concluded that the seaquake phenomena can be modelled numerically with acoustic elements in a FEA model, and larger floating structures give increasingly higher pressures on the bottom plate of the structure.

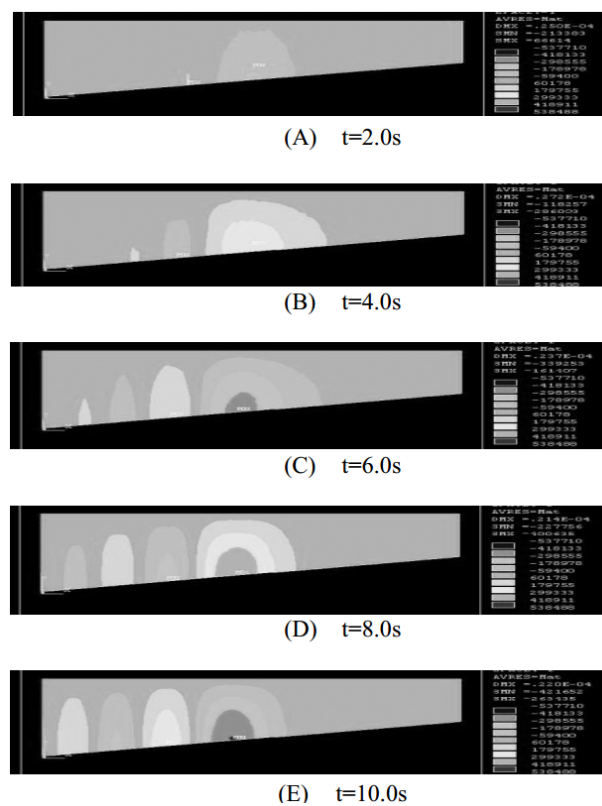


Figure 1.4-4: Results from time domain analysis of pressure distributions around the hypocenter with a mildly inclined seabed (Inoue et al., 2002).

1.4.3 Seaquake response of SFT

In 2010 Martire et al. investigated the SFT solution for the Messina Strait Crossing during a seismic event. The study includes both synchronous and multi-support excitation through time domain analysis, with synthetic accelerograms generated from simulation of the fault break mechanism. The accelerograms simulate the 1908 Messina earthquake, through the code AXITRA by using a 1D flat-layered medium propagation model. The study also includes propagation of vertical ground motion in the water. This is obtained through kinematics water data recorded during the fault rupture simulation at a grid of stations in the water layer. FSI is accounted for through the Morison equation, using the derived velocities and accelerations of the seaquake. It is indicated that multi-support excitations may excite vibration modes at higher frequencies more than synchronous excitation does. The article states that for long crossings, the shorter cables near shore attract large axial forces during a seismic event, due to the larger stiffness, shown in Figure 1.4-5. Further investigations are suggested to study more in detail the role of vertical ground motion propagating into water, as well as the issue of cable groups close to the shore (Martire et al., 2010).

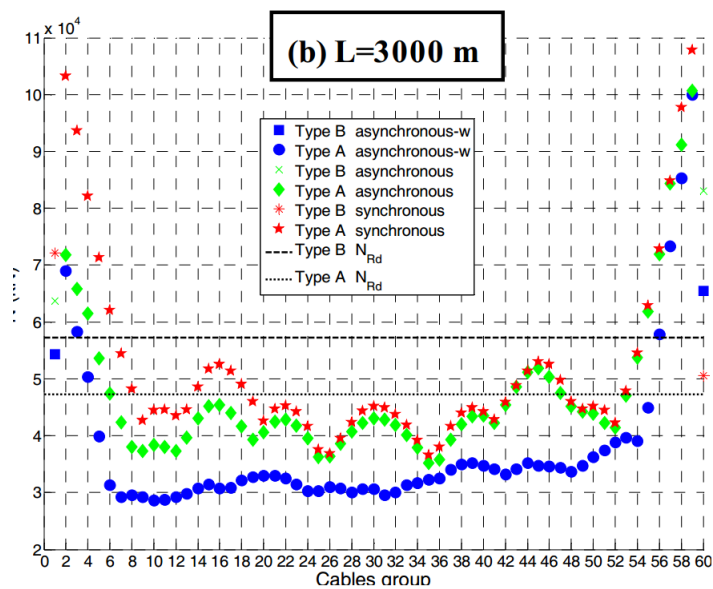


Figure 1.4-5: Distribution of axial force in the cables with inclined (A) and vertical (B) cables. Different earthquake excitations are also given. The large axial force in cables near shore is clearly illustrated (Martire et al., 2010).

Perotti et. al. studied non-linear dynamic response of SFT to earthquake and seaquake excitation. Seaquake is included in the study, derived from the velocity potential deduced from the 1D wave equation. Seabed is assumed rigid, and FSI is accounted for by using Morison equation on the relative velocity of the SFT with respect to the water. The SFT is modelled as straight bridge with no curvature, and longitudinal restraint devices are studied. The bars are analyzed with elastic and inelastic behavior. It is concluded that the seaquake effect can significantly increase the vertical response of the tunnel in all sections. The calculated vertical displacement in the mooring bars are shown in Figure 1.4-6. It is however noted that the seaquake is in this case modelled from 1D wave propagation with no energy dissipation, which both are conservative assumptions. The seabed is assumed rigid, which also will lead to a conservative solution. It is concluded that a model refinement of the seaquake excitation seems to be necessary (Perotti, Shi, Domaneschi, & Martinelli, 2013).

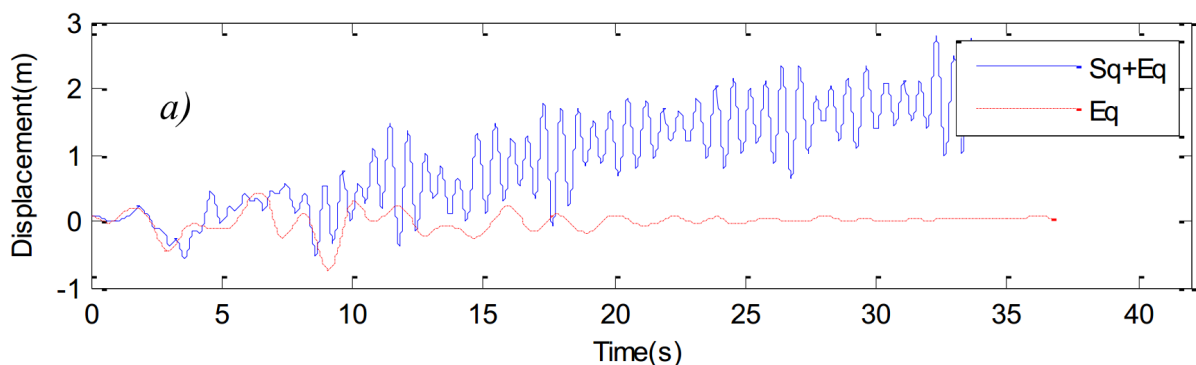


Figure 1.4-6: Vertical displacement at mid-span for inelastic bars during earthquake alone and seaquake in addition to the earthquake (Perotti et al., 2013).

In 2016 Martinelli et. Al. studied vibration mitigation and seaquake effects for SFTs under seismic motion. They found that seaquake effects mainly induced response in vertical direction, and that it increased the probability of damage due to higher stresses in the tunnel, as well as higher deformations in mooring bars. The authors suggesting a need to pay larger attention to seaquake excitation in future SFT designs. The velocity field is derived from potential theory and Morison equation is utilized to account for FSI of the tunnel (Martinelli, Domaneschi, & Shi, 2016).

In 2016, J. Mirzapour, M. Shahmardani & S. Tariverdilo investigated seismic response of submerged floating tunnel under support excitation. Seaquake was considered as water oscillations from seabed motion with a stationary bridge by means of 2D and 3D velocity potential functions. Further they transferred the forces as a line load generated from the pressure resulting from Bernoulli's equation on the velocity potential, and integrating along the tunnel surface. Spatial variation of ground motion was simulated by cross spectral density accounting for wave propagation along the tunnel length. It was concluded that the effect of spatial variation of ground motion on maximum values of the SFT displacement is very significant (Mirzapour, Shahmardani, & Tariverdilo, 2016).

1.4.4 Summary of research

To sum up the state of research, studies on seaquake loading on SFTs call for model refinement of the seaquake loading. The assumption of rigid seabed is frequently used to calculate SFT seaquake loading, however, how adequate this assumption is somewhat uncertain. As mentioned, Martire et. al. suggests to further study in detail the role of vertical ground motion propagating into water, as well as cable groups close to the shore attracting large stresses. A suitable model refinement for seaquake loading may be to adopt the procedure of Inoue et. al. using finite element analysis with acoustic elements to model the shock-effect from pressure waves in the water in time domain. This has apparently not been done for a long structure with varying seabed depth. A load generation procedure using a finite element analysis with acoustic elements also gives the opportunity to study the effects of the bedrock and eventual sediment properties on the pressure waves.

2 Theoretical background

2.1 Earthquakes

Earthquakes are the effect of shaking of the earth surface, and can be either man made or natural. Rock slides, volcanoes, nuclear explosions, change in groundwater or pore pressure due to dams, and geological fault slips can all create violent shaking of the earth surface (Kramer, 1996). Naturally caused earthquakes are among the most destructive natural disasters, accountable for several hundred thousand human lives. For instance, in 1979, an earthquake in Tangshan-province in China of magnitude 7.8 caused an estimated 700 000 casualties. In addition, earthquakes may cause tsunamis, such as the destructive 2004 Indian ocean tsunami. In 1908 a moment magnitude 7.5 earthquake with accompanying tsunami devastated the Messina area in Italy, estimated to cause 83 000 casualties, and the Kanto earthquake in Japan 1923, magnitude 7.9, is estimated to 99 000 casualties. Structural damage is the leading cause of death and economic loss in many earthquakes (Kramer, 1996). In other to mitigate the consequences of large earthquakes, proper design requirements and understanding of seismic behavior of structures is necessary to achieve sufficient earthquake-resistant design of structures.

2.1.1 Natural earthquakes

The most common type of natural earthquakes occurs as a result of the sudden release of energy from stresses in the earth crust during a fracture. The plane in which this fracture is caused is called a fault and the size can range from a couple of meters to several kilometers. The energy, and thus the size of an earthquake, is dependent on the stresses in the crust released and the size of the fault. The duration of the earthquake felt on the surface is limited, and it depends on how long the fault slip lasts, as well as direction of rupture and the area of the fault that has been ruptured. A larger area will send out vibration from different locations in the earth surface, which will arrive to the surface at different points in time. Large faults and stress buildups typically occur in tectonic plate boundaries, which is the explanation for why most of the biggest earthquakes occur in places like for instance California, Alaska, Chile and Japan, which all lie close to tectonic plate boundaries. This trend of earthquakes close to tectonic plate boundaries is clearly visible in the seismicity map shown in Figure 2.1-1.

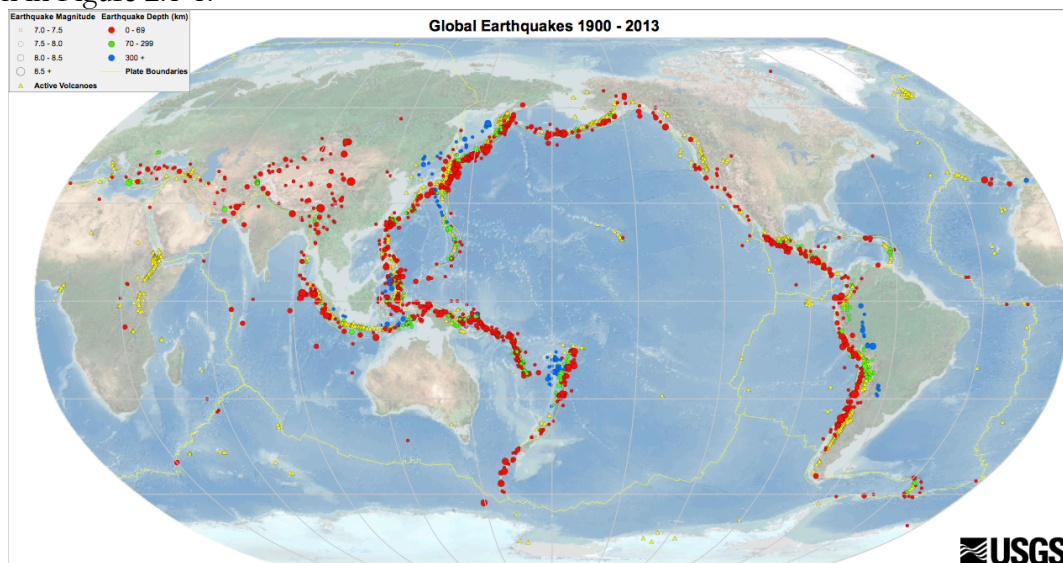


Figure 2.1-1: Worldwide seismicity map from 1900-2013 (USGS, 2017). Dots represent epicenters of significant earthquakes.

Wave types

Earthquake-waves can be divided into two types, body waves and surface waves. The four most important waves for earthquake engineering are illustrated in Figure 2.1-2. There are two types of body waves, primary waves (P-waves) which act as a pressure wave, and secondary waves (S-waves) which are shear type waves. The P-waves are analogous to sound waves, as pressure waves which are capable of travel through both solids and fluids. The S-waves however cause shear deformation in the medium of travel, meaning the particle motion is perpendicular to the direction of travel. Liquids, such as water are incapable of transferring shear forces, due to low viscosity, and thus S-waves cannot travel through most fluids.

S-waves are often divided into two components by the direction of particle movement, where the SV component consists of vertical plane particle movement, and SH of horizontal plane particle movement. The speed of body-waves is dependent on the stiffness of the medium they travel through, and since geological materials are stiffer in compression than shearing, P-waves propagate faster than S-waves (Kramer, 1996).

The other type of waves are surface waves. These propagate along the earth surface, and their amplitude decrease roughly exponentially with depth. Surface waves result from the interaction between body waves and the surface. These types of waves are more prominent than the body waves at distances far away from the earthquake source. For engineering purposes, the two most important surface waves are Rayleigh and Love waves. Rayleigh waves result from the interaction between SV-waves and P-waves at the surface. The particle movement of Rayleigh waves involve both vertical and horizontal components, and consist of a sort of rolling motion. Love waves consist of only in-plane movement, and have no vertical component in the particle motion. These waves are created from interaction between SH-waves and a soft surficial layer (Kramer, 1996).

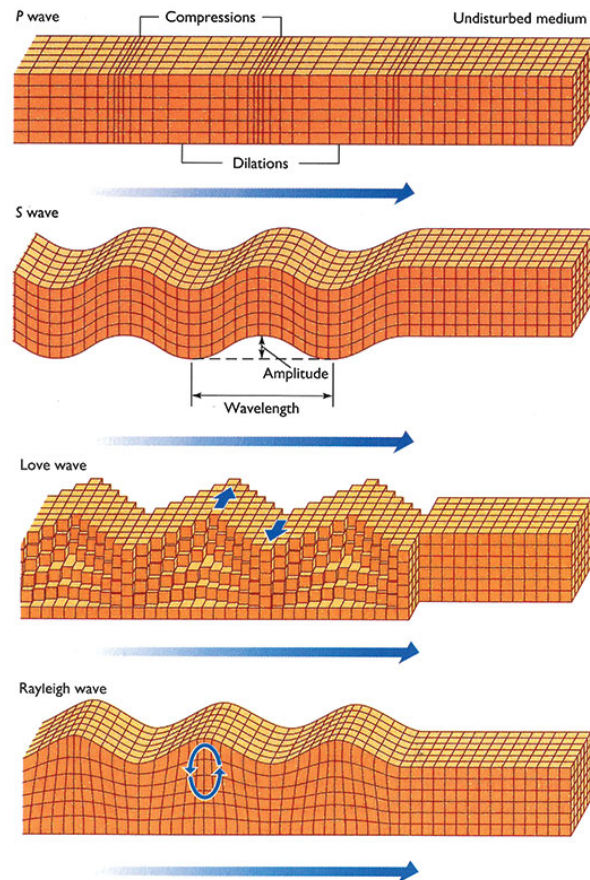


Figure 2.1-2: Illustration of wave types (Construction & Design, 2017).

2.1.2 Earthquake excitations

Earthquake motions are of an irregular and transient dynamic nature. The excitation experienced on the surface depends on several factors, such as the fault break mechanism and size, the properties of the bedrock and soil layers through which the seismic waves travel and the location of the site in relation to the fault. The dynamic interaction between the soil and the structure may as well influence the response, referred to as soil-structure interaction (SSI).

Soil amplification

In some cases, the earthquake excitations may be amplified through the soil layers. An earthquake in Mexico City in 1985 resulted in two close locations experiencing fundamentally different ground acceleration spectrums, which was a consequence of different soil properties. At SCT, the location with marine sediments consisting of quite deep soft clay, experienced a strong amplification of the earthquake excitation compared with UNAM, the location on bedrock, as shown in Figure 2.1-3. For the area with marine soil, the amplification was largest around the period of 2 seconds, corresponding closely to the anticipated fundamental eigenperiod of buildings with height around 15 stories. As a result, these buildings experienced large amounts of damage (Romo & Seed, 1986).

The soil behavior acts as a filter on the earthquake excitation, and it can result in an amplification or reduction of the ground motion. In the case of earthquake excitations hitting the eigenfrequencies of the dynamic soil system, the ground motion at the top of the soil may be several times larger than that of the bedrock. This effect is accounted for in the EC8 by utilizing a soil amplification factor. For the case of a seaquake, pressure waves through water may be amplified similarly, through constructive interference of the pressure waves.

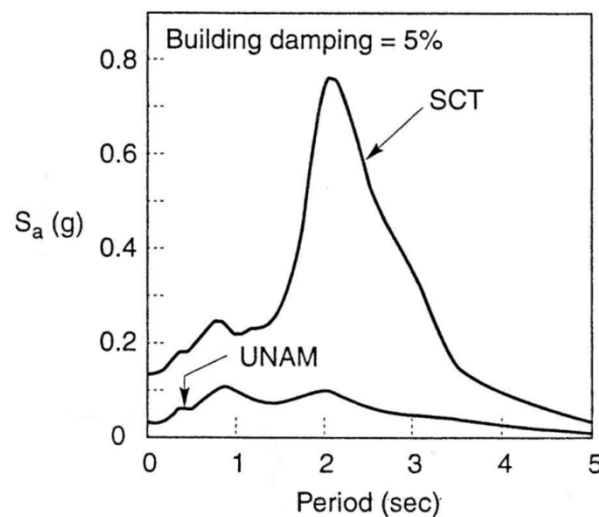


Figure 2.1-3: Acceleration spectrum of the Earthquake in Mexico 1985 of the two different locations (Romo & Seed, 1986).

Asynchronous ground motion

The distance from the hypocenter to a location on the surface can govern the duration as well as the relation of response between the surface and the hypocenter. The surface response is affected by the magnitude of the different types of ground waves, as given in 2.1.1, such as primary waves, Rayleigh waves and love waves. The arrival time of the different wave types will vary due to the difference in ground waves speed between the wave types, resulting in a change in characteristics of the seismic motion as a function of distance. In addition, when a seismic wave travels over a distance through ground, its properties change in both amplitude and frequency, because of for instance reflection and refraction due to inhomogeneous soil. This is often referred to as non-uniformity in the seismic excitation. For long structures, such as bridges, the seismic waves may arrive at the supports at different points in time. The waves will also have travelled through different soil conditions, resulting in asynchronous support excitations which may significantly alter the earthquake response of the structure. Previous studies on asynchronous excitation of SFT's have shown that such excitation may lead to significant excitation of SFT modes with negligible effective modal mass that would not be excited from synchronous ground motion (Martire et al., 2010). For instance, sinusoidal modes with an even number of waves will have zero effective modal mass, but may be excited from asynchronous ground motion.

When a rupture occurs along a fault the direction of rupture will also give different excitation characteristics in different directions due to the Doppler effect, where wave frequency increases in the direction of travel of the rupture, and decreases in the opposite direction. This directionality effect is illustrated in Figure 2.1-4 and may result in a strong fling pulse in the direction of the fault rupture due to overlapping pulses.

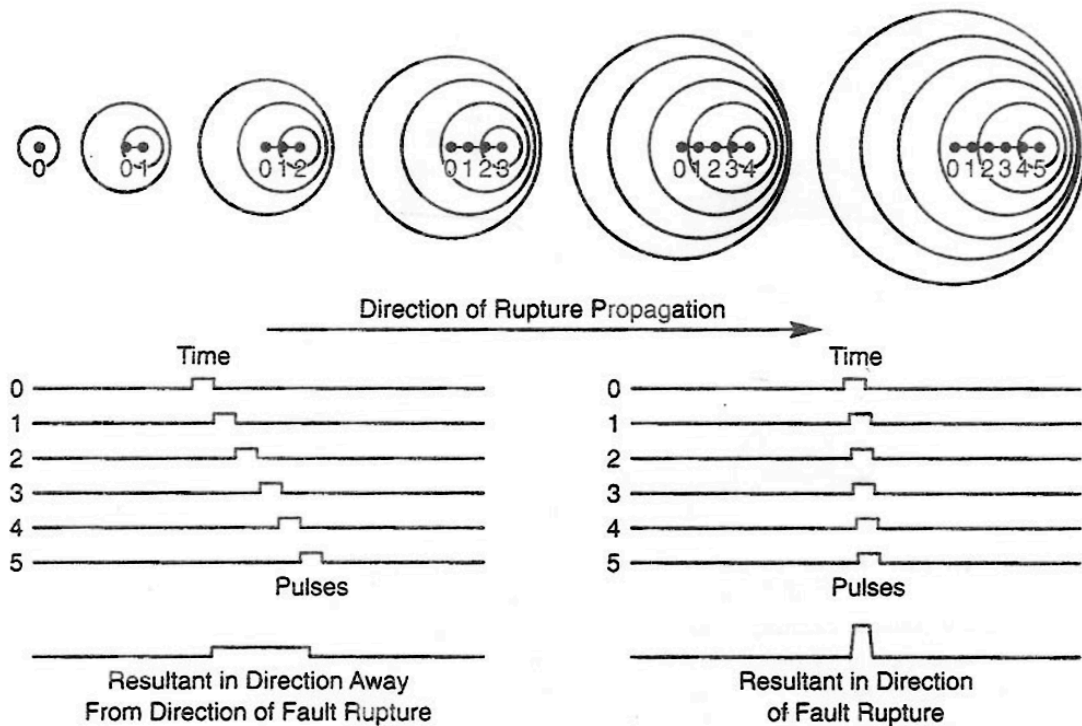


Figure 2.1-4 Schematic illustration of directivity effect on ground motion at sites towards and away from direction of fault rupture (Kramer, 1996).

2.1.3 Eurocode 8: Design of structures for earthquake resistance

It is necessary to have good building codes to account for seismic action, in order to reduce the consequences of an earthquake. A structure subjected to an earthquake experiences no external load, only a base acceleration, which from Newton's second law yields the excitation force of the system mass times acceleration. For an elastic SDOF system the response from an earthquake acceleration time series is thus dependent on the system mass, stiffness and damping, assuming effects such as forces from soil-structure interaction are neglected. The response can then be reduced to depend on eigenfrequency and critical damping ratio only. For a given earthquake time series one can therefore calculate a response spectrum, by plotting the highest response value for a given damping ratio and varying eigenfrequency. Often the response spectrum is plotted against period instead of frequency. Ideally, one can thus calculate the response of any given SDOF system undergoing seismic excitations from the response spectrum of the given ground motion time series. However, in practice, several other properties may affect the response of the structure. These are for instance soil-structure interaction (SSI), soil amplification, asynchronous ground motion and nonlinear structural behavior such as ductility. EC8 tries to incorporate these effects by different means, such as behavior factor for ductility, and soil amplification factor for the response spectrum method. The effects of SSI are more difficult to assess since the structural response and the response of the adjacent soil from earthquake excitations are coupled. EC8 offers several possible ways to account for seismic actions, both through analysis of spatial models with earthquake time series as loading, and through using simplified earthquake response spectrum, depending on type of structure, and structural importance.

Design by Modal solution and Response Spectrum Method

Most MDOF dynamic systems can be decoupled into an uncoupled system by modal decomposition, and thus be solved as several SDOF systems. As mentioned, the response of SDOF system to a specific earthquake time series only depends on eigenperiod and damping ratio. EC8 offers different idealized elastic earthquake acceleration response spectrums intended for design. When a modal response analysis is conducted, EC8 requires that the accumulated effective mass of the modes in the analysis need to be at least 90 %, and all modes with effective mass larger than 5 % of the total mass must be included.

For vertical earthquakes, EC8 gives separate spectrums from the horizontal ones. The peak ground acceleration in the vertical direction is given as a ratio to the peak ground horizontal acceleration. When solving a structural system by modal decomposition and response spectrum method, information about when the responses occur in the different modes are lost. As a result, a way of combining the modal responses to get a design response for the total structure is needed. According to EC8, for modal response calculations of structures with sufficiently separated eigenperiods, responses from different modes can be combined with the “square root of the sum of squares” (SRSS) method.

Time integration of EQ series

In addition to offering response spectrums EC8 offers representation of the seismic action through either synthetic, simulated or recorded earthquake acceleration time history. If synthetic accelerograms are used, they shall be generated to match the elastic response spectrums given in EC8. The same accelerogram is not to be used in both horizontal directions. Whether simulated, recorded or synthetic accelerograms are used, a minimum of three time-series are to be used. Time integrating offer several advantages from design in the frequency domain. Through time-domain analysis non-linearities and asynchronous excitations may be studied. Time-domain analysis also provide insight into physical behavior of the structure with possibility to visualize instantaneous and time variation of the response.

2.2 Fluid modelling

To investigate the behavior of a submerged structure, it is important to have sufficient understanding of fluid mechanics. Fluid mechanics is an entire branch of physical science, in which different fluid behavior is studied. For fluid dynamics, this can be the study of motions and forces within the fluid itself, or for fluid structure interaction (FSI). Having adequate models for FSI is essential for the design of structures in water such as offshore structures, shore-based structures such as quays, or for the present study, submerged structures. Fluid behavior can be examined either experimentally, or numerically. Fluid dynamic problems are often mathematically complex, and thus simplifications are often made to deal with the specific nature of the problem of interest. A brief discussion of a few fluid modelling approaches is presented in the following sections.

2.2.1 Computational Fluid Dynamics

Computational fluid dynamics (CFD) is a branch of fluid mechanics, where the aim is to simulate fluid flow problems by using numerical analysis. Most CFD analyses are based on solving some form of simplification of the Navier-Stokes equations (NSE). The equations are derived by applying Newton's second law to a fluid element, along with the assumption of mass and energy conservation. The NSE equations are given as mass conservation through the continuity equation, Newton's second law as the momentum equation, and energy conservation, shown in compact form using tensor notation in equations (2.1), (2.2) and (2.3).

$$\frac{\partial \rho}{\partial t} + \frac{\partial}{\partial x_j} (\rho \dot{u}_j) = 0 \quad (2.1)$$

$$\frac{\partial}{\partial t} (\rho \dot{u}_i) + \frac{\partial}{\partial x_j} (\rho \dot{u}_j \dot{u}_i + p \delta_{ij} - \tau_{ij}) = 0 \quad (2.2)$$

$$\frac{\partial}{\partial t} (\rho e_0) + \frac{\partial}{\partial x_j} (\rho \dot{u}_j e_0 + \dot{u}_j p + q_j - \dot{u}_i \tau_{ij}) = 0 \quad (2.3)$$

Table 2.2-1 Parameters used in Navier-Stokes equations.

ρ	Fluid density
t	Time
x	Coordinates
\dot{u}	Fluid velocity
p	Pressure
τ	Stress
e_0	Total energy
i,j	Tensor indices for direction with values from 1,2 and 3

The equations are very complex, and are a set of coupled differential equations describing the relation between pressure, temperature, velocity and density of a fluid moving in three dimensions and time. As partial differential equations, one could imagine they could be solved analytically, however, in practice they prove to be too difficult to solve (NASA, 2017b). In fact, as this problem remains mathematically unsolved, the Clay Mathematics institute of Cambridge, Massachusetts has listed it as one of the seven Millenium prize problems, with a prize of 1 million USD for each problem solved (Clay Mathematics Institute of Cambridge, 2017). For CFD however, several different techniques for solving the equations numerically exists, such as finite differences, finite volume, finite element and spectral methods. For this thesis the existence of these methods for solving fluid flow problems are acknowledged, but they will not be further assessed. A possible approach is to use further simplifications to the equation set until there is a group of equations possible to solve. By neglecting the effect of viscosity in NSE for instance we arrive at the simpler Euler equations (NASA, 2017a), which when solved gives an approximation to the of a fluid problem that may in some applications be adequate. Euler equations are given in (2.4), (2.5) and (2.6) with the same notations as in NSE.

$$\frac{\partial \rho}{\partial t} + \frac{\partial}{\partial x_j} (\rho \dot{u}_j) = 0 \quad (2.4)$$

$$\frac{\partial}{\partial t} (\rho \dot{u}_i) + \frac{\partial}{\partial x_j} (\rho \dot{u}_j \dot{u}_i + p \delta_{ij}) = 0 \quad (2.5)$$

$$\frac{\partial}{\partial t} (\rho \mathbf{e}_0) + \frac{\partial}{\partial x_j} ((\rho \mathbf{e}_0 + p) \dot{u}_j) = 0 \quad (2.6)$$

2.2.2 Potential Flow

For several fluid dynamic applications, it is sufficient to assume the fluid behaves irrotationally and with zero viscosity (inviscid). Irrotational fluid means that the curl of the gradient is always equal to zero, simply meaning every fluid particle is not rotating. This allows us to define a potential function $\phi(x,y,z)$ which satisfies the fundamental laws of fluid dynamics, namely the continuity equation, conservation of moment and conservation of energy. By neglecting viscosity effects, these are given in the Euler equations (2.4), (2.5) and (2.6).

By defining the fluid velocity V as the gradient of a potential function ϕ , the flow is inherently irrotational, shown in equation (2.8). This follows from the vector identity in equation (2.7). The potential function is from now on denoted the velocity potential function, and is the basis of potential flow theory.

$$\nabla \times \nabla \Phi = \mathbf{0} \quad (2.7)$$

$$\nabla \Phi = V \rightarrow \nabla \times V = \mathbf{0} \quad (2.8)$$

For an incompressible fluid, the continuity equation (2.4) with constant density in time and space, inserted for potential flow results in the Laplace equation in equation (2.9).

$$\nabla V = \mathbf{0} \rightarrow \nabla^2 \Phi = 0 \quad (2.9)$$

The irrotational flow assumption is clearly incorrect where vorticity effects of the flow are large, for example in the case of vortex induced vibrations. For a fluid flow near a boundary, around for instance a cylinder, there is a boundary layer where viscous effects dominate. Disregarding vorticity effects like vortex shedding, the flow sufficiently far away from the boundary layer is reasonable to assume as inviscid as the viscous forces acting on the fluid in this region are expected to be small. It is important to note that fluid modelling by potential flow can never be exact for a problem with boundary layers.

Potential flow may however be applicable where the boundary layer effect is acceptable to neglect, for instance for waves or fluid flows outside of the boundary layer surrounding an immersed object in a large fluid medium such as a fjord or an ocean. An illustration of potential flow streamlines is given in Figure 2.2-1. Based on the Laplace equation, the potential theory is applicable for this type of fluid dynamic problems. To calculate properties for structures in water such as hydrodynamic added mass and damping, the potential flow theory is central in computer software for large volume structures.

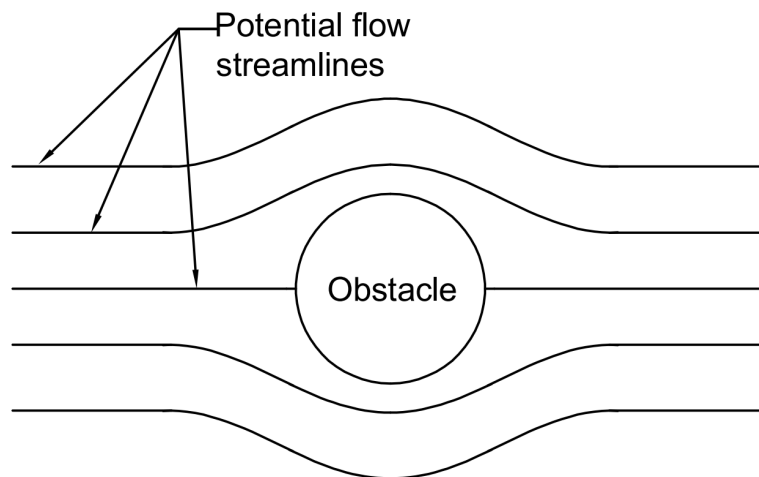


Figure 2.2-1: Illustration of potential flow streamlines around an obstacle.

2.2.3 Numerical solution of potential flow theory

The hydrodynamic analysis software WADAM is used in this thesis for the calculations of hydrodynamic properties of the SFT. A brief introduction to the theory of linear numerical solutions to potential flow theory utilized in the program code is presented in this subchapter. WADAM uses a panel model, where the body is discretized into panels, for the potential flow theory solution and it can calculate wave-structure interaction for fixed and floating structures of arbitrary shape. The panel model is designed to solve a boundary-value problem for the interaction of water-waves with bodies for finite or infinite water depth. The wave amplitude is assumed small compared to the wave length. Another assumption is that the oscillatory amplitude of the body motion is of the same order as the wave amplitude. The bodies may be modelled as fixed, constrained or neutrally buoyant and they may be bottom mounted, submerged or surface piercing. The theory presented here is based on the WAMIT theory manual which is the body-wave interaction code used in WADAM (Lee, 1995).

Problem description

The flow is assumed to be incompressible, inviscid and irrotational, and it is governed by the velocity potential $\phi(x, t)$, which satisfies Laplace's equation, equation (2.10), in the fluid domain. Laplace's equation implies continuity for incompressible potential flow, and is the basis for the important superposition principle which makes it possible to add different flows together resulting in a complicated flow. The fluid velocity is the gradient of the velocity potential, shown in equation (2.11).

$$\nabla^2\Phi = 0 \quad (2.10)$$

$$V(x, t) = \nabla\Phi = \frac{\partial\Phi}{\partial x}i + \frac{\partial\Phi}{\partial y}j + \frac{\partial\Phi}{\partial z}k \quad (2.11)$$

Here, i, j and k are unit vectors in the coordinate directions. Pressure is given from Bernoulli Equation (2.12) where ρ is the density, z is the depth, t is time and g is the gravitational constant.

$$p(x, t) = -\rho \left(\frac{\partial\Phi}{\partial t} + \frac{1}{2} \nabla\Phi \cdot \nabla\Phi + gz \right) \quad (2.12)$$

First order boundary Value Problem

The total first-order velocity potential ϕ satisfies the Laplace equation in the fluid domain and linearized boundary conditions. The linear free-surface condition and the condition at sea bottom for finite water depth are given in equation (2.13) and (2.14). Here, ν is described in equation, and originates from the dispersion relation in equation (2.22).

$$\phi_z - \nu\phi = 0 \text{ at } z = 0 \quad (2.13)$$

$$\phi_z = 0 \text{ at } z = -h \quad (2.14)$$

$$\nu \equiv \frac{\omega^2}{g} \quad (2.15)$$

The conditions at the body surface fulfil the boundary value problems given in equation (2.16) and (2.17). Equation (2.18) defines n_k used in equation (2.16), where \mathbf{n} is the unit normal vector in each direction and \mathbf{x} is the position on the body. It is assumed that the normal vector points out of the fluid domain. The velocity potential function is split into different parts. Scattering potential ϕ_s is the disturbance to the potential originating from the fixed body position. The incident wave has the velocity potential function ϕ_i .

$$\frac{\partial \phi_k}{\partial n} = n_k, \quad k = 1, 2, \dots, 6 \quad (2.16)$$

$$\frac{\partial \phi_s}{\partial n} = -\frac{\partial \phi_i}{\partial n} \quad (2.17)$$

$$\begin{aligned} \mathbf{n} &= (n_1, n_2, n_3) \\ \mathbf{x} &= (x_1, x_2, x_3) \\ (n_4, n_5, n_6) &= \mathbf{x} \times \mathbf{n} \end{aligned} \quad (2.18)$$

When walls, for instance a ship, are in the analysis, the velocity potential is under the boundary condition that the fluid velocity through the wall is zero, shown in equation (2.19).

$$\frac{\partial \phi}{\partial n} = 0 \quad (2.19)$$

First order problem solution

In order to solve the first order boundary value problem, the first order incident wave in (2.20) is considered with one frequency component ω .

$$\Phi_i = \frac{igA}{\omega} Z(kz) e^{-ik(x \cos \beta + y \sin \beta)} \quad (2.20)$$

This is a plane progressive wave with wave heading angle β , angular frequency ω , complex wave amplitude A and Z is the depth dependence of the flow and z is the depth. Equation (2.21) gives depth dependence for a certain depth h with corresponding wave number κ . The dispersion relation connecting wave number k with angular frequency ω is given in equation (2.22).

$$Z(kz) = \frac{\cosh(k(z+h))}{\cosh(kh)} \quad (2.21)$$

$$k \tanh(kh) = \frac{\omega^2}{g} \equiv v \quad (2.22)$$

The radiation potential, ϕ_R is due to motion of the body. The sum of scattering potential ϕ_s and the incident wave potential is the diffraction potential ϕ_D .

The total velocity potential function is given in equation (2.23).

$$\Phi = \Phi_i + \Phi_s + \Phi_R = \Phi_D + \Phi_R \quad (2.23)$$

The radiation potential is a linear combination of the components due to motions in all six degrees of freedom as shown in equation (2.24). ξ_k is the complex amplitude of the oscillatory motion in mode k and ϕ_k the corresponding unit-amplitude radiation potential. The six modes are denoted as surge, sway, heave, roll, pitch and yaw.

$$\Phi_R = i\theta \sum_{k=1}^6 \xi_k \phi_k \quad (2.24)$$

The reflected wave ϕ_I^r is to be added to describe the total wave field given in equation (2.25).

$$\Phi = \Phi_I + \Phi_I^r + \Phi_S + \Phi_R = \Phi_D + \Phi_R \quad (2.25)$$

The scattering and the radiation potentials are subject to a radiation condition stating that the wave energy associated with the disturbance due to the body is carried away from the body in all directions in the far field.

Integral equations

The boundary problem is solved in WADAM by the integral equation method. The velocity potential, ϕ_k , on the body boundary is obtained by solving the integral equation given by equation (2.26).

$$2\pi\phi_k(\mathbf{x}) + \iint_{S_B} d\xi \phi_k(\xi) \frac{\partial G(\xi, \mathbf{x})}{\partial n_\xi} = \iint_{S_B} d\xi n_k G(\xi, \mathbf{x}) \quad (2.26)$$

S_B denotes the surface of the body, G is Green's Functions, and ξ is the linear perturbation function. The integral equations given in equation (2.26) are solved by the panel method. An ensemble of panels represents the wetted surface. The unknowns are assumed to be constant over each panel and the integral equation is set at the center of each panel. The integration over a panel is carried out using either one or four-point Gauss quadrature.

Forces

The expressions for first order forces are derived from direct integration of fluid pressure over the body boundaries. The pressure integrations are given by Bernoulli's equation (2.12) and may be approximated by Taylor expansion. In this work, the static and dynamic force and moment are given in equation (2.27), obtained by integration of the first order pressure over the wetted surface of the body, S_B .

$$\begin{aligned} \mathbf{F} &= \iint_{S_B} P(\mathbf{x}) \mathbf{n} dS \\ \mathbf{M} &= \iint_{S_B} P(\mathbf{x}) (\mathbf{x} \times \mathbf{n}) dS \end{aligned} \quad (2.27)$$

The derivation of Taylor expansion of pressure, static and dynamic forces and moments are given in the theory manual. General expressions for hydrostatic force and moment are given in equation (2.28) with center of buoyancy (x_b, y_b) , volume V and unit vectors i, j and k .

$$\begin{aligned} \mathbf{F} &= \rho g V k \\ \mathbf{M} &= \rho g V (y_b i - x_b j) \end{aligned} \quad (2.28)$$

2.2.4 Analytical solution of resonance in water from pressure waves.

Undamped case

Assuming the water behaves irrotational, incompressible and inviscid, propagation of primary waves can be modelled with the wave equation. Incompressible behavior is reasonable when the particle velocities are low compared to the speed of sound in the medium. Feynman developed the wave equation in (2.29) for one dimensional case (Kramer, 1996).

$$\frac{\partial^2 u}{\partial x^2} - \frac{1}{c^2} \frac{\partial^2 u}{\partial t^2} = 0 \quad (2.29)$$

Where c is the speed of sound in water given in the equation (2.30). K_s is the bulk modulus and ρ is the density.

$$c = \sqrt{\frac{K_s}{\rho}} \quad (2.30)$$

The water is considered overlaying rigid bedrock, as shown in Figure 2.2-2. Assuming constant wave speed, and solving the equation assuming harmonic solution gives vertical displacement expressed in equation (2.31).

$$u(z, t) = Ae^{j(\omega t + kz)} + Be^{j(\omega t - kz)} \quad (2.31)$$

A and B is the amplitude of the waves travelling in up- and downward direction and ω is the angular frequency, k is the wave number for a given frequency shown in equation (2.32).

$$k = \frac{\omega}{c} \quad (2.32)$$

Inserting zero pressure at the sea surface as boundary condition gives equation (2.33).

$$\begin{aligned} p(0, t) &= K_s \varepsilon_v(0, t) = K_s \left(\frac{\partial u}{\partial z} \right)_{z=0} = 0 \\ \rightarrow K_s ik \left(Ae^{ik(0)} - Be^{-ik(0)} \right) e^{i\omega t} &= 0 \end{aligned} \quad (2.33)$$

Resulting in the nontrivial solution $A=B$ for the displacement. The displacement u is the solution for a standing wave by constructive interference of the upward and downward waves from (2.34) (Kramer, 1996).

$$u(z, t) = 2A \underbrace{\frac{e^{ikz} + e^{-ikz}}{2}}_{\cos(kz)} e^{i\omega t} = 2A \cos(kz) e^{i\omega t} \quad (2.34)$$

An amplification function can be given for the water surface in equation (2.35) or in an position z under the surface in equation (2.36), where motion at depth H corresponds to the seabed motion.

$$H(\omega) = \frac{|u_{\max}|_{z=0}}{|u_{\max}|_{z=H}} = \frac{2Ae^{i\omega t}}{2A\cos(kH)e^{i\omega t}} = \frac{1}{\cos(kH)} = \frac{1}{\cos\left(\frac{\omega H}{c}\right)} \quad (2.35)$$

$$H(\omega) = \frac{|u_{\max}|_{z=z}}{|u_{\max}|_{z=H}} = \frac{2A\cos(kz)e^{i\omega t}}{2A\cos(kH)e^{i\omega t}} = \frac{\cos(kz)}{\cos(kH)} = \frac{\cos\left(\frac{\omega z}{c}\right)}{\cos\left(\frac{\omega H}{c}\right)} \quad (2.36)$$

With the corresponding eigenfrequencies for the displacement given in equation (2.37). Note that velocities as differentials of displacement will have a corresponding eigenfrequencies of the amplification with factors of even numbers instead of odd due to the sine nature of $H(\omega)$ for velocities.

$$f_i = \frac{2i-1}{4} \frac{c}{H} \quad (2.37)$$

$$\rightarrow f_1 = \frac{c}{4H}$$

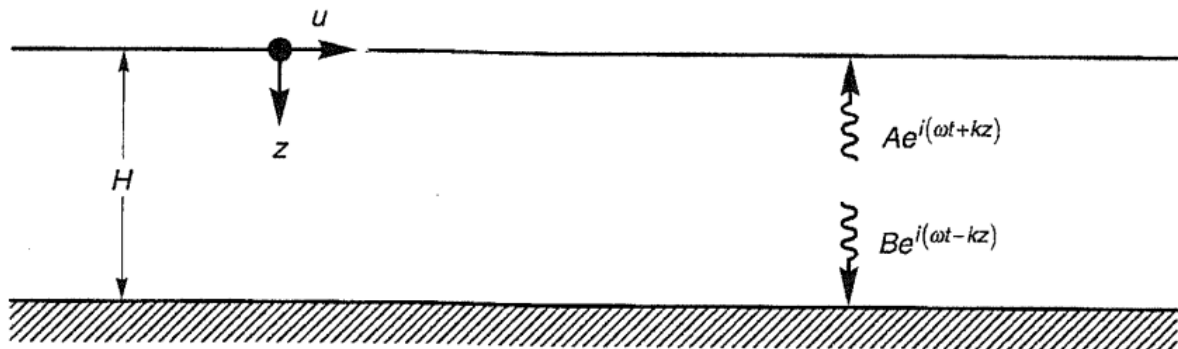


Figure 2.2-2: Water with thickness H overlying rigid bedrock. System equivalent for soil in Figure 7.3 (Kramer, 1996).

Damped case

By assuming the damping in the primary wave system can be treated similar to classical dynamic system with viscous dashpot damping behavior, the wave equation including damping is given in equation (2.38).

$$\rho \frac{\partial^2 u}{\partial x^2} = K_s \frac{\partial^2 u}{\partial t^2} + \eta \frac{\partial^3 u}{\partial t \partial x^2} \quad (2.38)$$

In the previous equation, η is the dashpot force per velocity. This results in equation (2.39) similar to the solution for displacement as in the undamped scenario, except for a complex wave number.

$$u(\mathbf{z}, t) = A e^{i(\omega t + k^* z)} + B e^{i(\omega t - k^* z)} \quad (2.39)$$

The complex speed of sound in water, c^* is given in equation (2.40) including critical damping ratio ξ . The complex wave number, k^* , includes the complex wave speed. Remark that all following simplifications neglects the quadratic terms of the damping ratio ξ .

$$\begin{aligned} c^* &= \sqrt{\frac{K_s^*}{\rho}} = \sqrt{\frac{K_s(1+i2\xi)}{\rho}} \approx \sqrt{\frac{K_s}{\rho}} (1+i\xi) = c(1+i\xi) \\ k^* &= \frac{\omega}{c^*} = \frac{\omega}{c(1+i\xi)} = \frac{\omega(1-i\xi)}{c(1+\xi^2)} \approx \frac{\omega}{c}(1-i\xi) \end{aligned} \quad (2.40)$$

Resulting in the nontrivial solution given in equation (2.41), analogous to the undamped case.

$$u(\mathbf{z}, t) = 2A \underbrace{\frac{e^{ik^*z} + e^{-ik^*z}}{2}}_{\cos(k^*z)} e^{i\omega t} = 2A \cos(k^*z) e^{i\omega t} \quad (2.41)$$

Rewriting results in the equation (2.42) for the amplification function for displacements:

$$H(\omega) = \frac{u_{\max, z=0}}{u_{\max, z=H}} = \frac{1}{\cos\left(\frac{\omega H}{c^*}\right)} \approx \frac{1}{\cos\left(\frac{\omega H}{c}(1-i\xi)\right)} \quad (2.42)$$

Finally, for an arbitrary position z under the water surface the complex displacement amplification function is given in equation (2.43).

$$H(\omega) = \frac{u_{\max, z=0}}{u_{\max, z=H}} = \frac{\cos\left(\frac{\omega z}{c^*}\right)}{\cos\left(\frac{\omega H}{c^*}\right)} \approx \frac{\cos\left(\frac{\omega z}{c}(1-i\xi)\right)}{\cos\left(\frac{\omega H}{c}(1-i\xi)\right)} \quad (2.43)$$

2.2.5 Numerical solution of acoustic problems in ABAQUS

The propagation of pressure waves in water can be estimated numerically through time domain finite element analysis in ABAQUS with acoustic elements (Dassault Systmes Simulia Corp, 2017). In general, acoustic elements are used for modelling of sound propagation problems in acoustic mediums. Acoustic analyses are suitable to model shock or pressure waves in a fluid, for instance originating from an underwater explosion, or for seaquakes from seabed ground motion.

Acoustic analysis in ABAQUS can be purely acoustic or a coupled between acoustic and structural elements. The acoustic elements are defined with only one active degree of freedom, which is pressure, given as nodal output POR in ABAQUS. For a coupled structural analysis, the nodes on the interface between the structural and acoustic elements also have the structural respective degrees of freedom, for instance displacement. Acoustic mediums are most commonly a fluid, where stress is purely hydrostatic, i.e. no shear stress, and pressure is proportional to volumetric strain. For most acoustic engineering analyses, the initial stress in the acoustic medium has negligible physical effect on the acoustic waves.

The equilibrium equations used in acoustic analyses are for small motions of a compressible, adiabatic fluid with velocity-dependent moment losses given in (2.44).

$$\frac{\partial p}{\partial \mathbf{x}} + \chi(\mathbf{x}, \theta_i) \dot{\mathbf{u}} + \rho(\mathbf{x}, \theta_i) \ddot{\mathbf{u}} = 0 \quad (2.44)$$

Here, p is the pressure in the fluid, \mathbf{x} is the spatial position, \mathbf{u} is the fluid position, ρ is the fluid density, χ is the volumetric drag and θ are other field variables such as temperature. An example of the use of other field variables is to combine a predefined field for temperature with temperature dependent material properties such as density. The volumetric drag is the force per unit volume per velocity and can be applied to give an exponential decay of the wave amplitude as a function of distance. It must not be confused with the Morison drag force given in 2.3.3. The spatial gradient of the volumetric drag to mass density are neglected, which is a fair approximation for homogeneous fluids.

The fluid is assumed to be inviscid and compressible, giving the pressure equation (2.45). The bulk modulus K_s of the acoustic medium gives the relation of dynamic pressure p to the volumetric strain ε_v .

$$p = -K_s \varepsilon_v \quad (2.45)$$

Adequate mesh refinement is central to achieve accurate result in acoustic analysis. Abaqus manual recommend that ten, at least six representative internodal intervals of the acoustic mesh should be included into the shortest acoustic wavelength of the analysis. For linear elements, the internodal interval is defined as the element size. For time domain analysis, it is reasonable to estimate the wavelength using the highest frequency present in the loading. Required element length L_{\max} is given in equation (2.46) with respect of max frequency f_{\max} , wave speed c and minimum internodal intervals per acoustic wavelength n_{\min} .

$$L_{\max} < \frac{c}{n_{\min} f_{\max}} \quad (2.46)$$

Boundary conditions

There are several options to define boundary conditions to an acoustic model. The most intuitive boundary condition is to directly prescribe the field variables at surfaces. For instance, acoustic pressure may be set to zero at a given surface.

ABAQUS provides acoustic infinite elements, which can transmit energy out of the finite element mesh that will never return to the domain during the analysis. These elements can behave as a nonreflecting radiating boundary condition and is often used in problems in which the region of interest is small compared to the surrounding medium. The infinite elements allow the finite element fluid region to be reduced in such cases, while maintaining accuracy. For three-dimensional analysis, acoustic infinite elements are defined as shell elements with a reference point defining the direction of the infinite domain.

The location of the reference point is the basis for defining the “radius” and “node ray” for the acoustic infinite elements given in Figure 2.2-3. The direction of wave energy transmission out of the element is defined by the node rays, and therefore strongly depends on the location of the reference point.

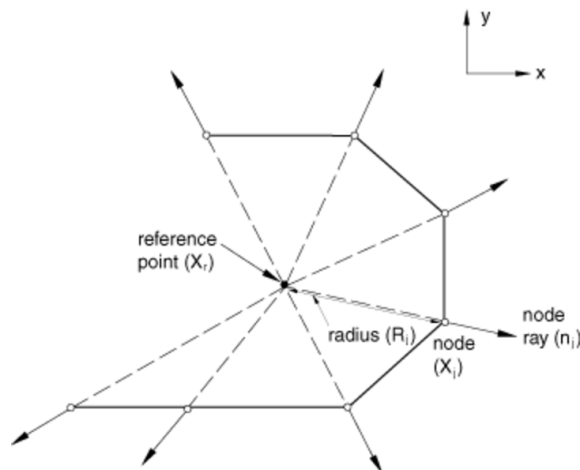


Figure 2.2-3: Illustration of reference point and “node ray” for acoustic infinite elements (Dassault Systèmes Simulia Corp, 2017) .

The node ray is the unit vector in direction of the line between the reference point and the nodes at the infinite elements. The node rays are used to compute the smallest dot product of the unit node ray and the unit normal of all acoustic elements surrounding the node. The boundaries with infinite elements are optimized by making the boundary between the finite and infinite elements as close to being orthogonal to the normal of the infinite elements as possible.

Loads

Incident wave loading is one way to apply incident wave loading on an acoustic model. The source of the incident wave is defined by a source node, and the incident load is applied at the loaded surface given with a standoff node. The incident wave can be given as either spherical, planar or diffuse. A diffuse wave is a field of planar waves from multiple angles. The wave can be applied with an acceleration or pressure amplitude time history at the standoff node with a corresponding reference value.

2.2.6 Impedance and reflection coefficient

Acoustic waves hitting boundaries between acoustic mediums will result in reflections and transmissions of the wave. The ratio of reflected wave to transmitted wave is called the reflection coefficient and is determined from the acoustic properties of the two mediums at the boundary. The reflection coefficient is given in equation (2.48) and is a relative ratio between the individual impedances of the two adjacent mediums. Impedance is a measure of the fluids resistance to motion (Long, 2014). The subscript 1 is used for the medium in which the incident wave originates, and subscript 2 for the medium it reaches at the boundary. For a negative reflection coefficient, the acoustic wave changes sign upon reflection. The specific impedance Z for a medium is given in equation (2.47), where p is the pressure, ρ is the density, c is the speed of sound and \dot{u} is the fluid particle velocity. This equation may be used to calculate acoustic pressure if the fluid particle velocity is known.

$$Z = \frac{p}{\dot{u}} = \rho c \quad (2.47)$$

$$R = \frac{\rho_2 c_2 - \rho_1 c_1}{\rho_2 c_2 + \rho_1 c_1} \quad (2.48)$$

For instance, the reflection coefficient from water to air is close to -1, meaning almost all energy is reflected and almost none is transmitted into the air.

2.3 Fluid structure effects

A submerged structure will behave differently from a similar structure in air, especially in terms of its dynamic properties. The fluid affects properties such as effective mass, damping and eigenfrequencies. The following sections will focus on the added mass and damping effect on a fluctuating submerged construction.

2.3.1 Added mass and structural eigenmodes

The acceleration-proportional hydrodynamic forces on a body is act as an inertia force, analogly to Newtons second law of motion. From an engineering point of view, one can imagine that some of the fluid surrounding an immersed body oscillates along with the body. Added mass is a way of approximating the inertia forces involved with fluid structure interaction, as the mass of the accelerated fluid times acceleration is the inertia force acting on the structure from the fluid. The particles adjacent to the body will accelerate to different degrees depending in their position relative to the body, so it must be noted that added mass is a weighted integration of the mass of the accelerated fluid (Newman, 1977).

The added mass coefficient, C_M , is simply the ratio of fluid mass accelerating in phase with the body to, usually, the mass of the displaced fluid volume. For instance an added mass ratio of one means that the mass of water accelerating with the body is equal to the displaced volume. There are theoretical values for hydrodynamic mass of cross sections for structures in 2-D, under the assumption of a long stiff structure and infinite fluid, given in Figure 2.3-1. When the assumptions deviate significantly from the physical case, such as for a soft deformable structure or a very confined fluid in for instance shallow water, these theoretical values of course becomes less accurate.

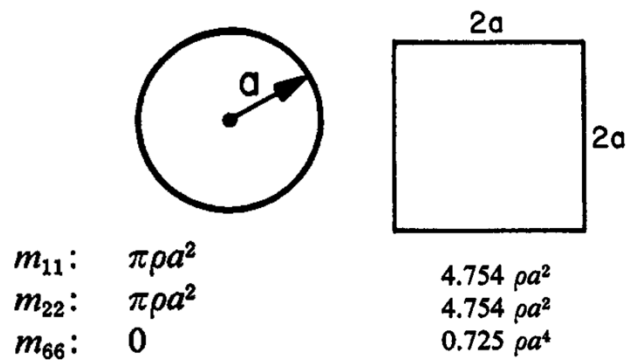


Figure 2.3-1: Added mass coefficients for circle and square cross section excerpted from Table 4.3 in *Marine Hydrodynamics* of J.N. Newman (Newman, 1977).

The added mass coefficient depends on the geometry of the body, and if the geometry of the body is non-symmetrical, the added mass may be strongly dependent on the direction of the oscillation. Two special cases can be used to exemplify this. The first being a flat plate normal to the direction of oscillation, where the added mass will go towards infinity relative to the displaced fluid mass. The other special case is the opposite, where the body is long in the oscillatory direction, and the added mass will be significantly smaller than the displaced fluid mass.

The added mass of a body will be influenced if the body is oscillating close to a free surface or another body. For some cases and assumptions, there exist theoretical values for added mass as a function of relative depth from a free surface. Added mass for a single circular cross section as a function of the relative distance from the free surface to the radius of the circle is given in Figure 2.3-2. The added mass coefficient is shown for heave or sway motion, corresponding to vertical or horizontal oscillation in the figure.

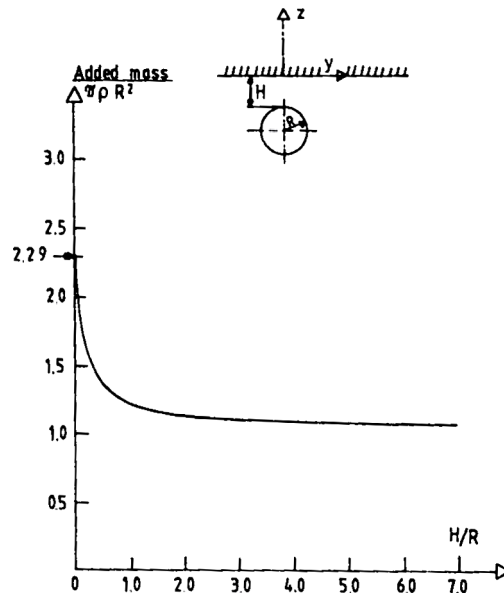


Figure 2.3-2 Added mass for a circular cross section as given in Figure 3.11 (Faltinsen, 1990) as a function of relative depth from free surface. The added mass coefficient is shown for heave or sway motion, corresponding to in plane vertical or horizontal oscillation in the figure.

Added mass is an important hydrodynamic property, as it affects structural behavior significantly, for instance eigenfrequencies. The properties of dry eigenmodes and wet eigenmodes of a submerged body can be considerably different due to the deviating values of total oscillating mass and hydrodynamic stiffness. The equations for eigenfrequencies are given in (2.49)

$$\begin{aligned}\omega_{n,dry} &= \sqrt{\frac{K}{M}} \\ \omega_{n,wet} &= \sqrt{\frac{K_{wet}}{M_{wet}}}\end{aligned}\tag{2.49}$$

2.3.2 Hydrodynamic damping

In structural dynamics, applying damping on a dynamic system as idealized viscous dashpot behavior to account for the dissipating energy in the system is common. However, in hydrodynamics, viscous damping is used to refer to the damping related to the forces originating from the viscosity of the fluid.

A submerged body will experience additional damping compared to a body in air, due to the hydrodynamic damping forces. Drag damping is an example of a hydrodynamic viscous damping force, which is often approximated as proportional to the relative fluid-structure velocity \dot{u} as shown in equation (2.50). By considering the contribution of these damping forces one might be able to design a more optimal structure for certain load cases, compared to the case when the hydrodynamic damping is neglected.

$$F_D = C_D \dot{u} \quad (2.50)$$

Radiation damping

Radiation damping is created from the coupling of the body and the surrounding fluid, generating radiative waves in the fluid. This effect depends on parameters such as water density, water depth, distance from fluid surface, relative velocities, and oscillating frequency of the structure. From this follows that the radiation damping is larger in fluids such as water when compared to air, due to differences in fluid properties such as density. The loss of energy due to the creation of radiative waves and can be resolved by doing numerical potential theory considerations (Newman, 1977). In the software WADAM, this is referred to as “potential damping” due to originating from potential theory considerations. The dominating factor contribution to the amount of lost energy in radiation damping is the generation of gravity waves at the free surface. For some periods gravity waves travelling on the surface are easy to excite, and therefore radiation damping is expected to be largest in this frequency area. At lower and higher frequencies, far away from the frequency range of easily excited gravity waves, the radiation damping is expected to be close to zero due to almost no formation of gravity waves.

Viscous damping

Viscous damping in a fluid is the opposing force from the fluid on the structure originating from the viscous properties of the fluid. The definition of viscosity is the resistance of the fluid to oppose shear deformation, alternatively the resistance of motion on one layer over the adjacent one (Chandrasekaran, 2015). For slender and long bodies, viscous damping may dominate the damping of the system. For instance, a spar buoy, in which the draft is large compared with the diameter, the viscous damping is particularly important for resonance in the heave direction. Viscous damping is a nonlinear force, and increases with parameters such as surface roughness of the body and relative velocity of the fluid. Viscous damping is not limited to shear effects, but may also originate from effects of vortex shedding, where energy is dissipated in the wake of a structure. Engineering models such as the Morison equation, further explained in 2.3.3, simplify the damping forces from shear forces on the structure and vortex effects into a single parameter for drag damping. For some engineering cases, it is sufficient to linearize the damping around velocities that are expected in the structure.

2.3.3 Morison equation

The most known engineering simplification of wave force on slender structures is the semi empirical Morison Equation. Newman suggest a diameter-wavelength ratio of 0.1 to 0.2 to be the upper limit for slender body approximation (Newman, 1977). Morison equation, (2.51), states that the total hydrodynamic force on a solid is equal to the inertia force and drag force added together. The accuracy of the result of this equation strongly depends on the quality of the input of the empirical drag- and added mass coefficients, C_D and C_M , of the body.

$$F = \rho C_M V \ddot{u} + \frac{1}{2} \rho C_D A \dot{u} |\dot{u}| \quad (2.51)$$

In equation (2.51), ρ is the density of the fluid, V is the volume of the structure, \ddot{u} is the relative acceleration of the structure, \dot{u} is the relative velocity of the structure, and A is the area associated with the drag coefficient.

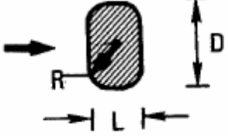
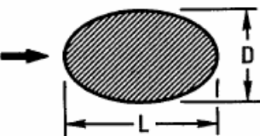
Note that in Morison equation the drag forces are all the opposing forces proportional to the square of the relative velocity of the fluid, both shear and pressure forces. The viscous damping referred to in 2.3.2 is shear forces only, being just one part of the total drag on a body exposed to a moving fluid. Drag force associated with pressure is also known as form drag. A common area used for the drag force is the projected area in the streamline direction (Crowe, 2009). Morison equation disregards the inherent interaction between drag and inertia forces. Nevertheless, for engineering purposes Morison's equation is often still used. Radiation damping is not included in Morison drag damping, and for relevant cases must be evaluated by numerical potential theory modelling as mentioned in 2.3.2.

The coefficients C_M and C_D are experimentally examined for different shapes, material roughness, speeds, Reynolds Number given in equation (2.52), etc., and further scaled up to the size of the realistic structure. These experiments can be done in a physical basin or numerically for instance with Computational Fluid Dynamics (CFD) software. The drag coefficient of the SFT will change over time and increase with increasing marine growth, and is thus difficult to evaluate a correct value for the lifespan of the SFT. For some cases, marine growth will be beneficial since it will increase damping, however, if drag forces are of a concern, this same effect will be undesired. Marine growth will also increase both mass of the structure and its added mass coefficient. DNV has listed recommended drag and added mass coefficients for offshore structures of different shapes, which is probably adequate for the present study (DNV, 2010a). Excerpts of these values used in modelling in this study are shown in Table 2.3-1.

$$Re = \frac{\dot{u} \cdot L_c}{\nu} \quad (2.52)$$

Reynolds number is defined as a ratio of the inertial forces to the viscous forces. L_c is the characteristic length and ν is the kinematic viscosity. Reynolds number is a central property when determining the transition between laminar and turbulent flow, and is frequently used as a scaling parameter for drag-coefficients for different geometrical shapes.

Table 2.3-1: Excerpted values of drag coefficients for a rectangle and ellipse from Appendix E in DNV's Recommended Practice for Environmental Conditions and Environmental Loads (DNV, 2010b).

4. Rectangle with rounded corners	L/D	R/D	C_D	L/D	R/D	C_D	
	0.5	0	2.5	2.0	0	1.6	
		0.021	2.2		0.042	1.4	
		0.083	1.9		0.167	0.7	
		0.250	1.6		0.50	0.4	
	1.0	0	2.2	6.0	0	0.89	
		0.021	2.0		0.5	0.29	
		0.167	1.2				
		0.333	1.0				
	$Re \sim 10^5$						
	14. Ellipse			D/L	$C_D (Re \sim 10^5)$		
			0.125	0.22			
			0.25	0.3			
			0.50	0.6			
			1.00	1.0			
			2.0	1.6			

3 Case study Bjørnafjorden

3.1 Design basis

As mentioned earlier, the plans for crossing Bjørnafjorden with a SFT has already been rejected in favor of other bridge proposals. There are however documentation and drawings for several SFT proposals considered by OO, both pontoon and tension leg designs. The tension leg solution is most prone to vertical ground accelerations, as the vertical ground motion will cause stresses propagating through the tethers. The seismic activity in Norway is in general modest, but Bjørnafjorden lies fairly close to the peak in the seismic hazard map. Figure 3.1-1 shows seismic zones in southern Norway for return period of 475 and 10 000 years. For this case study, only one of the proposed SFT's with tether anchors will be analyzed.

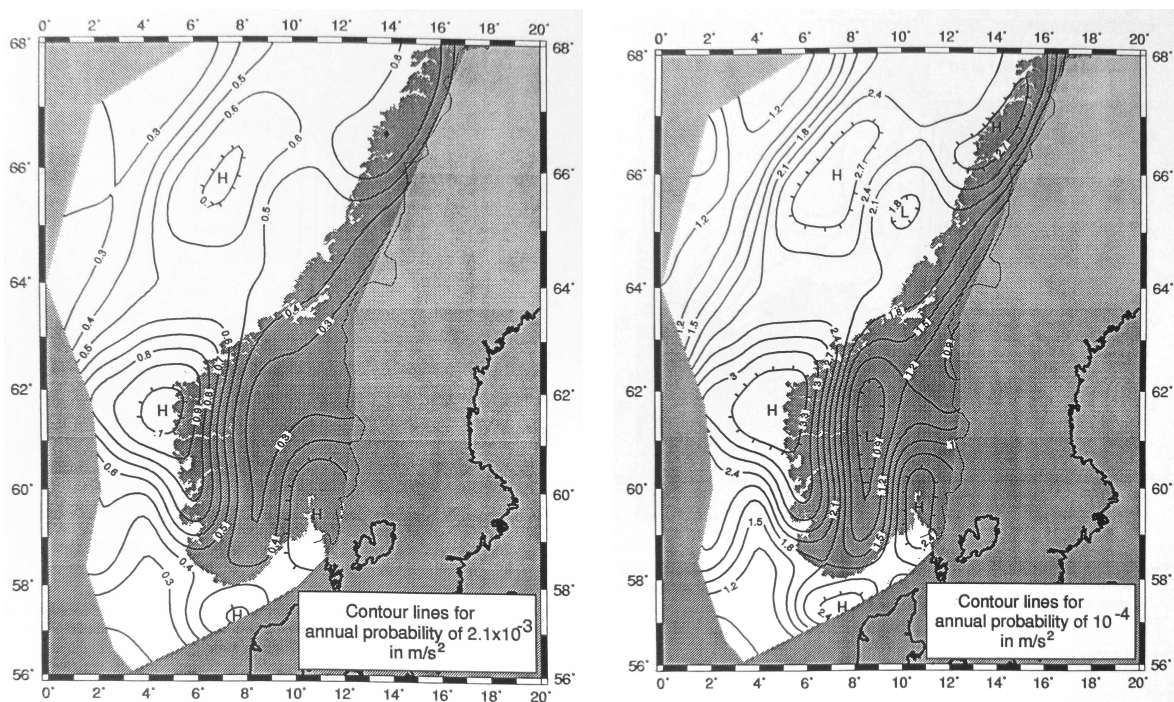


Figure 3.1-1: Seismic zones in southern Norway, a_{g40Hz} in m/s^2 for return period of 475 years (left) and 10 000 years (right). The grid is given in coordinates, where Bjørnafjorden is located at approximately 60,5 degrees North and 5 degrees East (Norwegian Council for Building Standardization (NBS), 1998).

The SFT for this study crosses Bjørnafjorden from Svarvhella in the south to Røtinga in the north, having a total curved length of 5373 m, with a curvature radius of 6000 m. The SFT is submerged with a top elevation of the bridge at 30 m below lowest astronomical tide (LAT). The seabed topology is varying, the south end is in general relatively shallow with depths at around 100-200 meters, followed by a sudden increase in depth to about 500 meters. The depth profile of the seabed as well as a plane view of the SFT is shown in Figure 3.1-2. The load bearing capacity is assured by the use of buoyancy and vertical tethers. The bridge is designed to be ballasted to a static net buoyancy of about 10% of the total weight of the structure. The net buoyancy is balanced with tension in the tethers. All figures in the length direction are presented with south to the left and north to the right.

3.1 Design basis

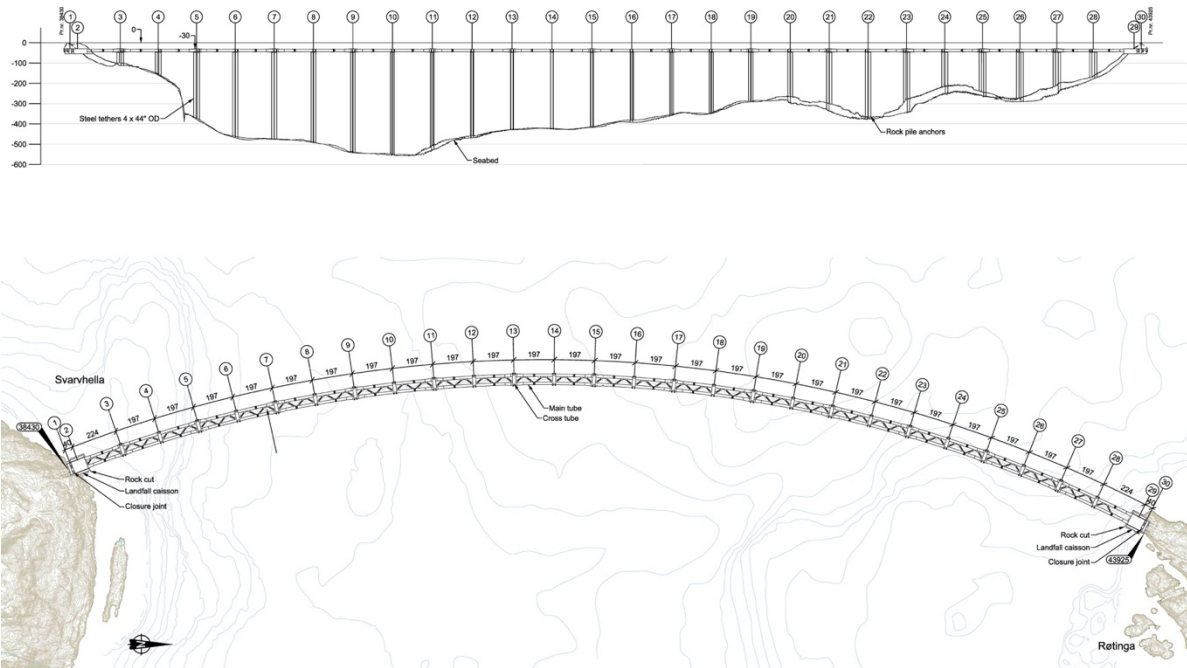


Figure 3.1-2: Projected seabed topology and plane view of the curved SFT bridge. The plane view is shown from south at the left end to north at the right end.

The ends of the SFT are anchored with large underwater landfall caissons, as the SFT continues into a rock tunnel. These end anchors are intended to work as fixed boundaries for the bridge. The SFT is made up of two pipes with 40 m center distance, and connected by four horizontal bracings per section length of 197 m in the free span. The span at the end anchors, measured to the center of the landfall caisson have a length of 224 m at end anchoring, measured to the center of the landfall caisson. The section at the south end including the landfall caisson is shown in Figure 3.1-3.

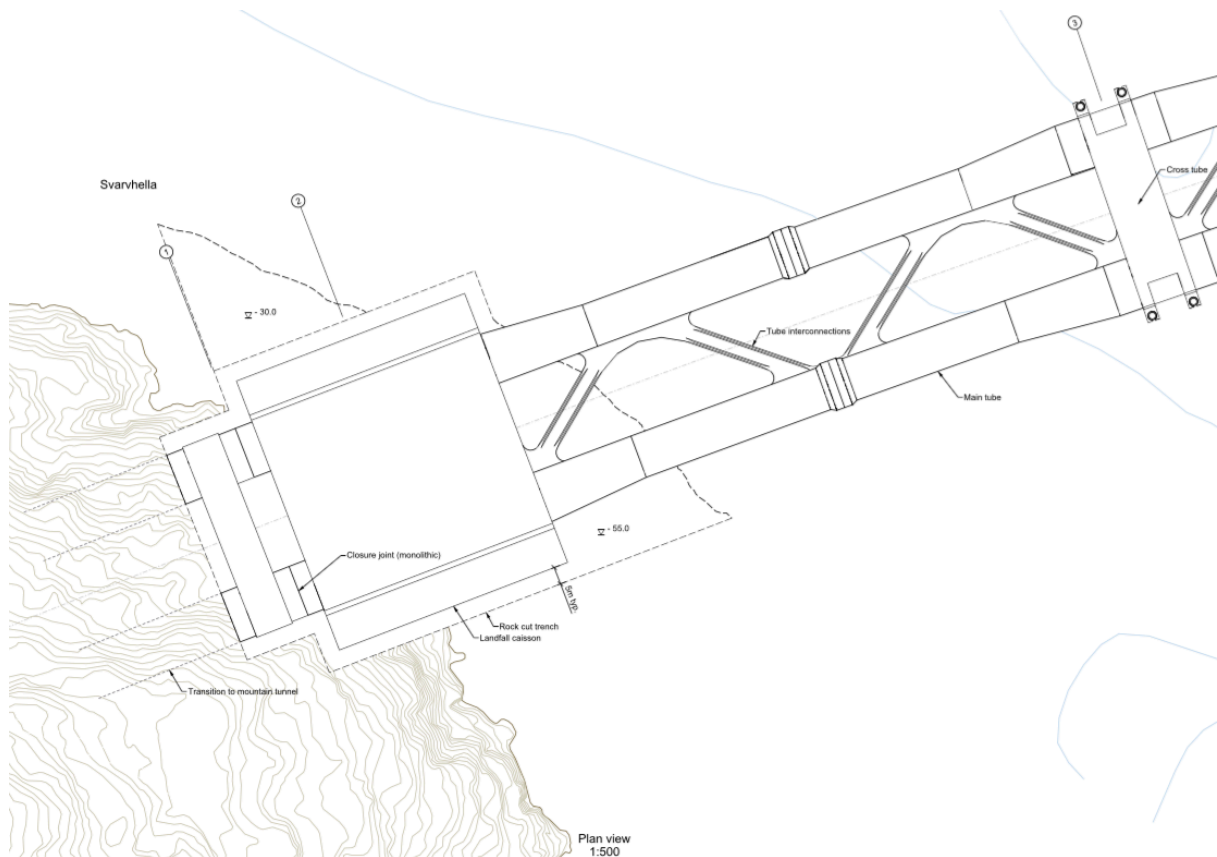


Figure 3.1-3 Plan view of the south end section including landfall caisson connecting the SFT to a conventional rock tunnel.

Each section is connected to the next with a cross tube, both providing stiffness and functioning as emergency exits between the pipes. The cross tubes alternate in size due to half of the cross tubes having lay-bys. The two alternating cross tube connections are shown in Figure 3.1-4. The cross section of the pipe also increases in the sections with lay-bys. These two cross sections are shown in Figure 3.1-5. At the bottom of each tube cross section there is a flat part with vertical walls used to anchor pre-tension cables lying in a circle through the pipe walls.

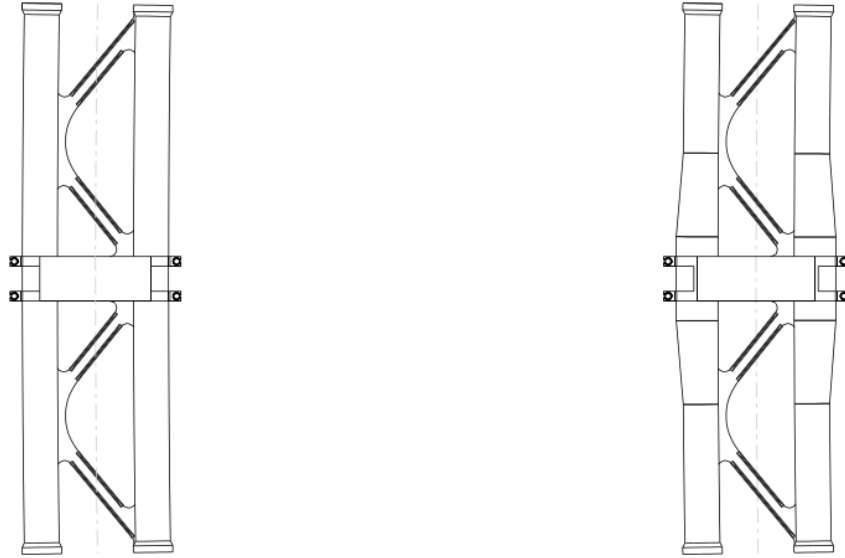


Figure 3.1-4: Alternating cross tube connections without lay-bys (left) and with lay-bys (right). The sections shown are 197m in length and include the horizontal bracing system.

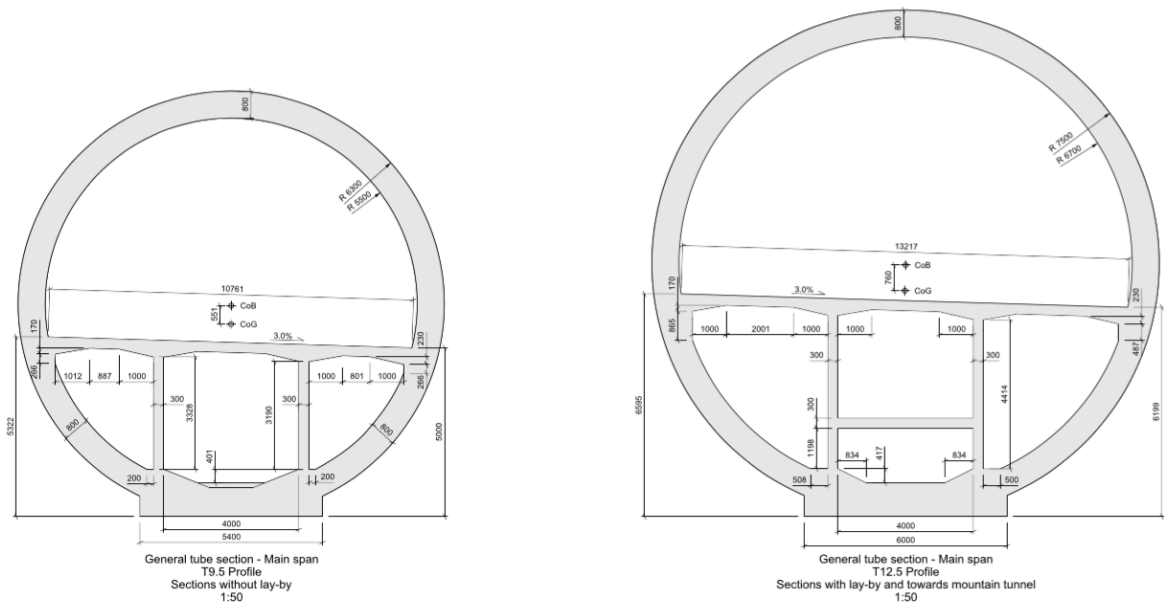


Figure 3.1-5: The cross sections of the pipe without lay-bys shown to the left, and with lay-bys to the right.

At each cross tube, there are four vertical steel tethers, a group of two tethers on each side of the cross tube. Due to the alternating width of the cross tubes, the internal center distance between the tether groups alternate between 63.3 m and 58.4 m, where the latter is shown in Figure 3.1-6. By locating the tethers this far apart in the width direction, they will contribute to torsional stiffness by opposing torsional rotation with a force-pair. The tethers are assumed to be of a hollow circular cross-section, with a diameter-thickness ratio such that they are roughly neutrally buoyant in water. The number of tethers and their dimensions are set equal for all tether groups, as the tethers along with buoyancy are accountable for the main load bearing capacity. Since the tether stiffness is dependent of length, this results in stiffer tethers at the shallowest water. The tethers are assumed anchored to the seabed with rock pile anchors.

High stress oscillations in the tethers may result in several undesirable effects. If the tethers reach compression during a seismic event, they may temporarily gain slack with from their anchors with the SFT or seabed, which may cause local damage to the anchors from impact when the tethers become loaded. In addition, precautions need to be made to ensure the tethers do not pop out of their anchors if they reach zero stresses. High tension stresses may also be of concern with respect to low cycle fatigue if the tethers reach yield stresses.

The submerged depth of the SFT and tube diameters also vary along the length of the SFT due to the variation in cross sections, but for this case study simplifications are made. The submerged depth is set to 30 m all along the length and the smallest pipe cross section and cross tubes are chosen for the entire length of the bridge. The cross section of the smallest pipe chosen for modelling in this case study is shown in an enlarged version in Figure 3.1-7.

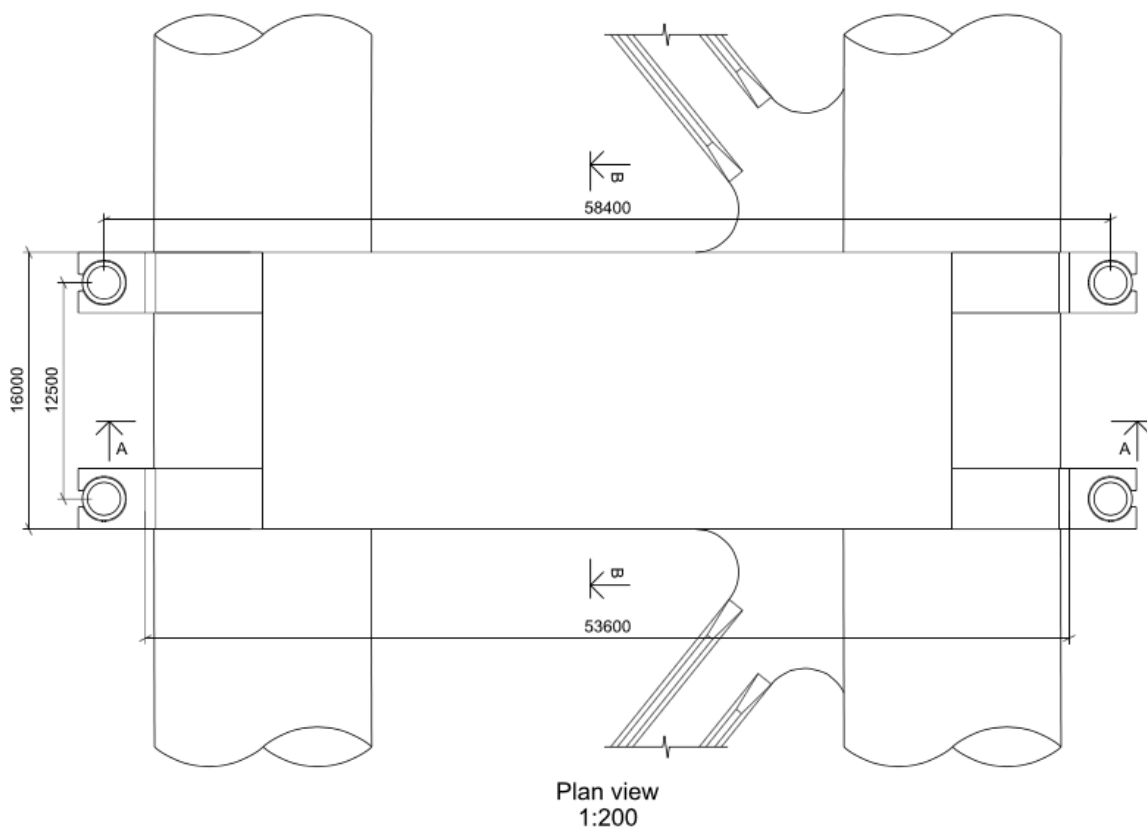


Figure 3.1-6: Plan view of the cross tube with tether placings shown for a section without lay-by.

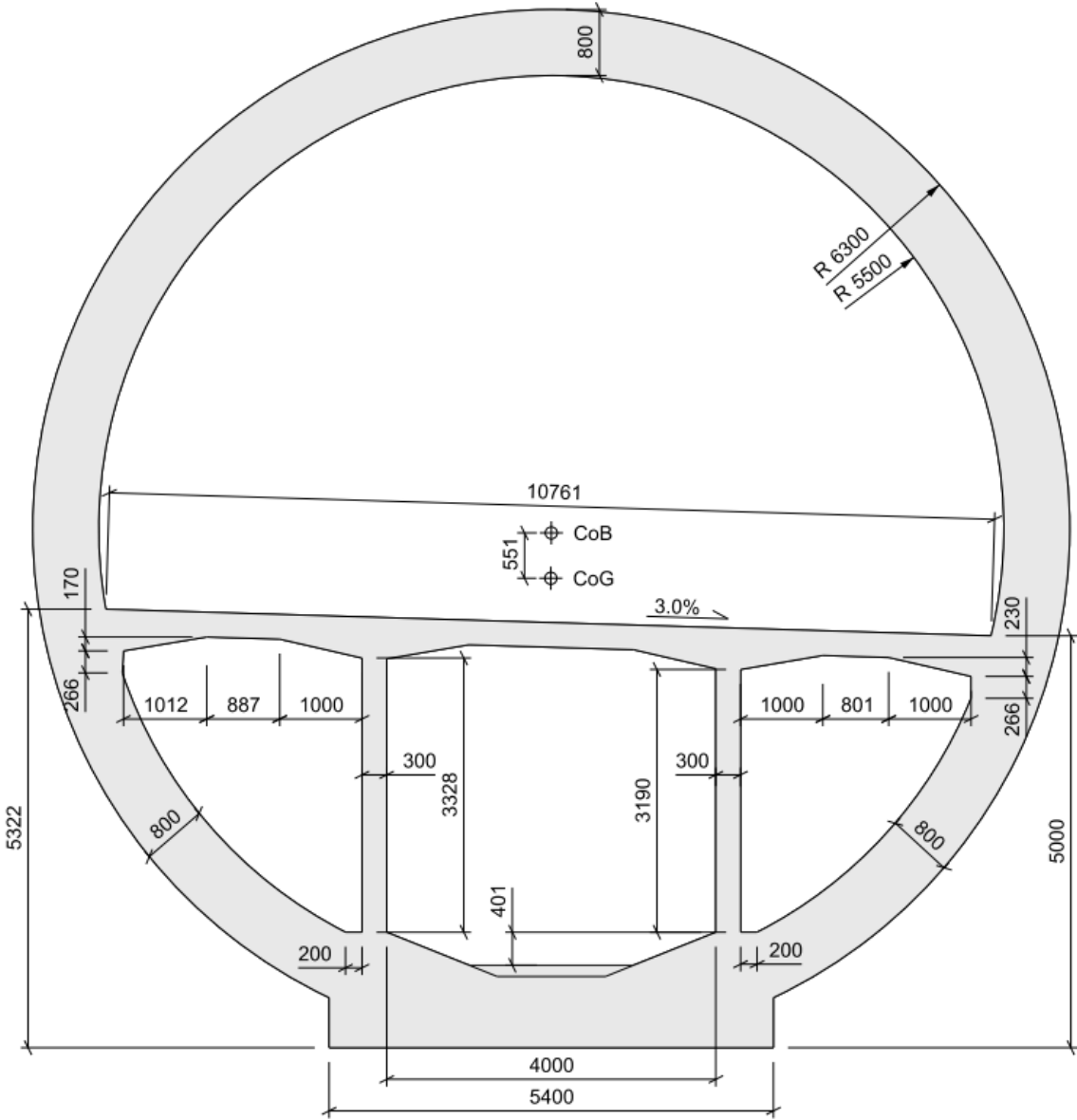


Figure 3.1-7: Enlarged cross section of the pipe without lay-by.

A summary of the parameters from the design basis for use in the modelling of the SFT in this thesis are shown in Table 3.1-1. Correspondingly, selected material properties from the design basis used in modelling are given in Table 3.1-2.

Table 3.1-1: Key parameters for the tether stabilized SFT from OO.

Curved length	5373 m
Number of spans	27
Number of tether groups	26
Pipe diameter	12.6 m
Pipe thickness	0.8 m
Free span section length	197 m
End section length	224 m
Minimum submerged depth to tunnel top	30 m
Tether distance c/c	Alternating 63.3m and 58.4m
Tether diameter	1.1 m
Tether thickness	0.038 m
Curvature radius	6000 m

Table 3.1-2: Material parameters used for modelling of the SFT, taken from the design basis from OO.

Concrete: B55 M40	
E-modulus	38000 MPa
G-modulus	15800 MPa
Poisson ratio	0.2
Design compressive stress	31 MPa
Steel S355	
E-modulus	210 000 MPa
G-modulus	80 000 MPa
Density ρ_{steel}	7850 kg/m ³
Poisson ratio	0.3

3.2 Earthquake time series

For the case study, it is chosen to analyze response to three vertical earthquake acceleration time series. The time series originate from recordings at Nahanni in Canada 1985 at Site 3, Friuli in Italy 1976 at Tarcento and Imperial Valley in USA 1940 at Superstition Mountain. The time series have been modified to match the EC8 design spectrum.

The time series are normalized by scaling the accelerations according to the seismic hazard for Bjørnafjorden. Both a scaling for an earthquake with return period of 10 000 years and an earthquake with recurrence of 475 years is used in the response study. The 475-year earthquake is scaled to the design value for PGA for Bjørnafjorden according to EC8. This calculation is shown in (2.53), where a_{gr}/a_{g40Hz} is the correlation factor between accelerations at 40 Hz and reference acceleration for EC8, a_{gv}/a_g is correlation between vertical and horizontal ground motion, and γ_I is the structural importance class, all given in EC8. The peak horizontal value for a_{g40Hz} at Bjørnafjorden is given as 0.9 m/s^2 (Standard Norge). According to OO an acoustic survey has shown there is little sediments close to the shore, while the seabed outside the slopes are in general soft deposits. As mentioned in the literature survey in chapter 1.4, SFTs usually attract the largest dynamic response close to the shore where the tethers are short. The soil factor for time series normalization is therefore set to be bedrock, even though there are some soft sediments in the deepest parts of the fjord. This will nevertheless be a reasonable approximation since the tethers are assumed anchored to the seabed with rockpiles. For design purposes the effects from sediments may be worthy of further investigations.

$$SA_{gv} = \left(\frac{a_{gr}}{a_{g40Hz}} \right) a_{g40Hz} \left(\frac{a_{gv}}{a_g} \right) \gamma_I \quad (2.53)$$

For the earthquake with 10 000 year return period, the seismic hazard map gives a peak value for horizontal acceleration of about 3.3 m/s^2 at Bjørnafjorden as given in Figure 3.1-1. For this case, the PGA is scaled to account for the seismic hazard map giving horizontal earthquakes by adopting the EC8 correlation factor between horizontal and vertical peak acceleration, as well as accounting for the map accelerations being given at 40 Hz. For the scaling of PGA, the importance factor from EC8 are ignored for this earthquake, as structural importance is already accounted for by applying an earthquake with higher return period. The resulting normalizing peak accelerations for both EC8 design and 10 000 year earthquake are given in Table 3.2-1.

Vertical acceleration time series for the Nahanni, Friuli and Imperial valley after normalization for EC8 design with 475 year return period is shown in Figure 3.2-1. The acceleration series for the 10 000 year earthquakes are identical except for a different scaling of the acceleration amplitudes according to Table 3.2-1. The earthquakes with 475 year return period will primarily be used for seismic response analysis in this case study, and these are the time series used unless else is specifically described.

Table 3.2-1: PGA for 10 000 year return period and 475 year return period used for normalization of time series.

Return period	Resulting normalized PGA
10 000 years	1.584 m/s^2
475 years	0.864 m/s^2

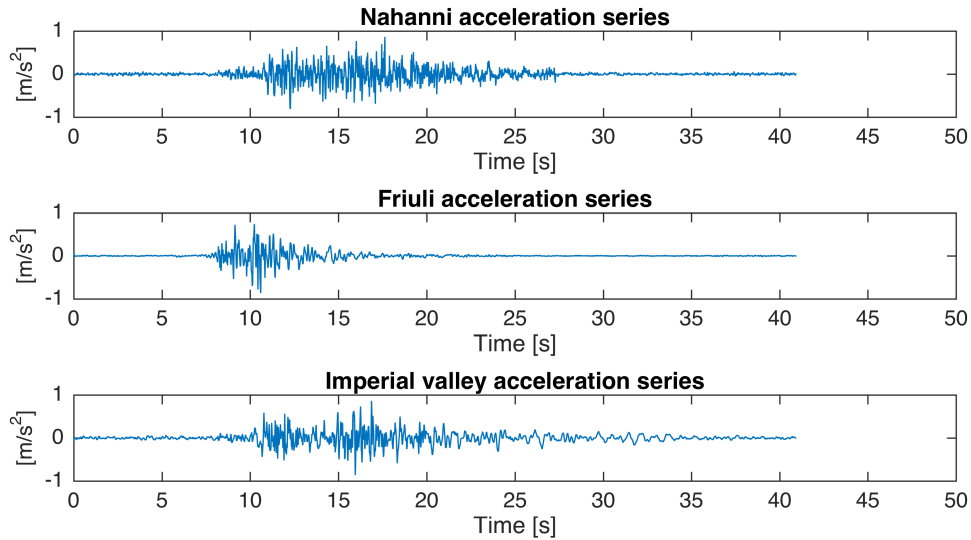


Figure 3.2-1: The acceleration time histories scaled for PGA equal 0.864 m/s^2 according to EC8 with return period of 475 years. Nahanni series on top, Friuli in the middle and Imperial valley at the bottom.

To find the dominating frequencies of the three earthquake time series used in this thesis, a FFT algorithm is applied to transform the acceleration series into the frequency domain. The resulting one sided spectrums of the accelerations in frequency domain are shown in Figure 3.2-3. Also included in the figure is a line indicating the frequency of the highest frequency vertical eigenmode with significant effective mass of the SFT as calculated later in chapter 6.2.1.

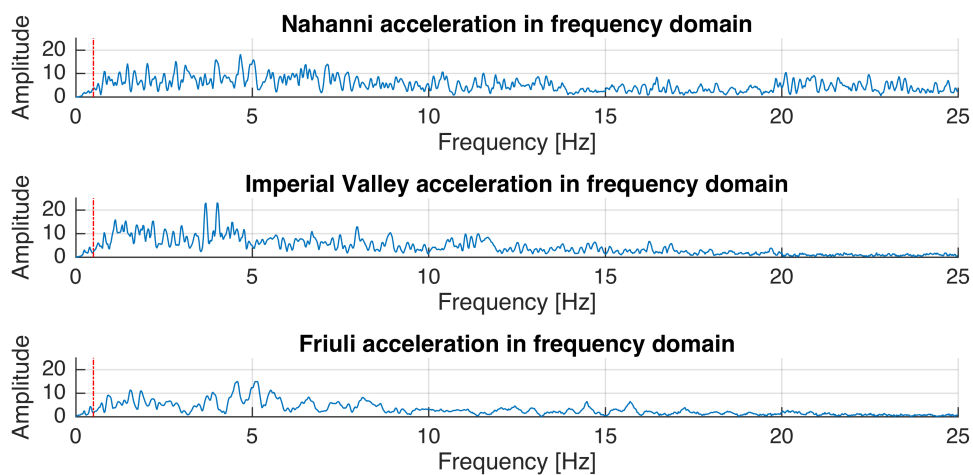


Figure 3.2-2: The acceleration series in the frequency domain calculated with FFT. The red dotted line represent 0.5 Hz which is slightly above the resulting highest vertical eigenfrequency with significant effective mass.

The acceleration amplitudes in the frequency domain show that for all the acceleration time series the dominating frequencies are roughly in the range of 1-10 Hz.

As mentioned, the acceleration time series have been normalized to match the elastic design response spectrum in EC8. To illustrate this, a linear acceleration Newmark time iteration scheme is applied on the acceleration time series to generate a pseudo acceleration response spectrum with damping set to 5 % critical damping. The response spectrums for the earthquake with 475 year return period are then plotted together with EC8 vertical response spectrum for 5 % critical damping, as shown in Figure 3.2-3. The response spectrums illustrate that the acceleration series are well fitted to the eurocode elastic design spectrum.

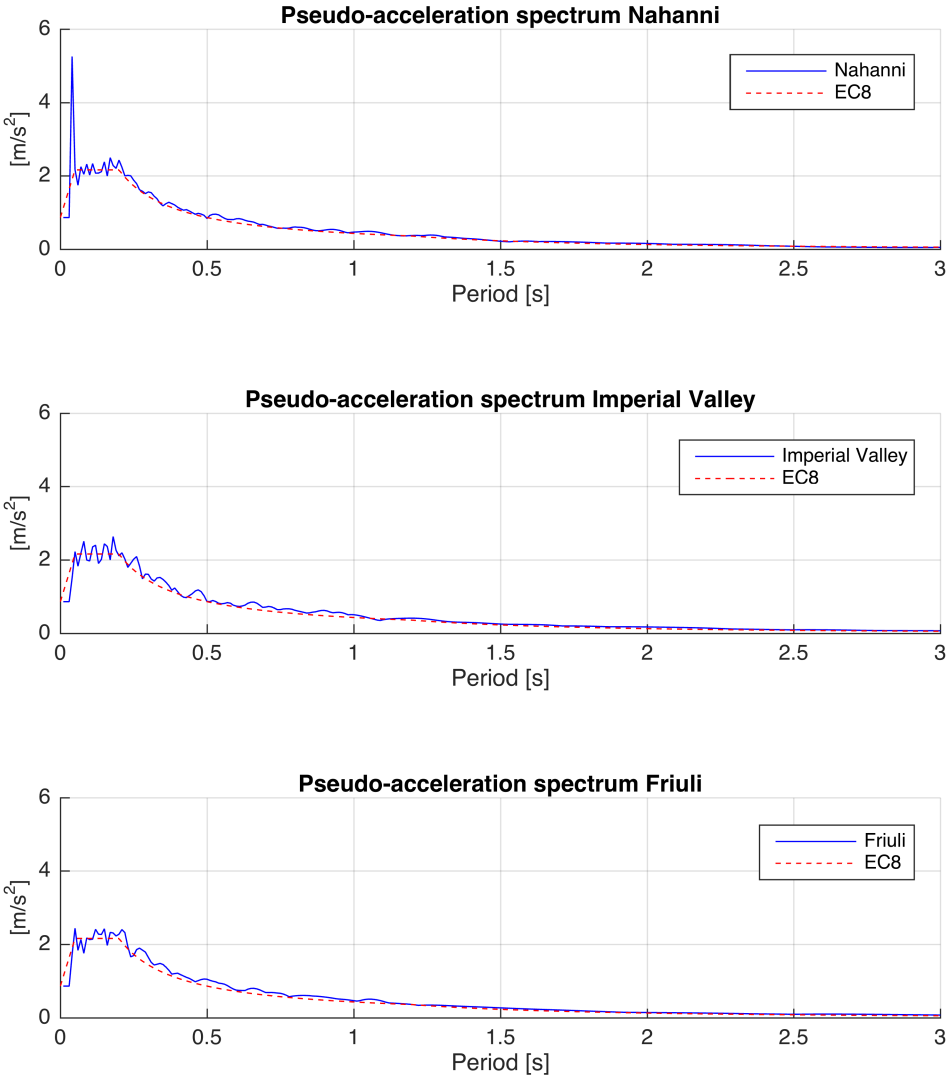


Figure 3.2-3: Pseudo acceleration spectrums plotted together with design vertical acceleration spectrum from EC8. Spectrums are from Nahanni at the top, Imperial Valley in the middle and Friuli at the bottom.

3.2.1 Strong motion Friuli

The computational power for some analyses in this case study is limited. For the time series analysis with FE models requiring high amounts of computational power it is desirable to reduce the length of the time domain analysis, and thus the acceleration time series. This is specifically for the ABAQUS acoustic time domain seaquake analysis according to chapter 6.5.2. For this case only the strong-motion part of the earthquake series is considered. There are several different definitions of what constitutes the strong motion region of an earthquake. The Friuli accelerogram has a short duration of the strong motion part, and will therefore be used as basis for these analyses. A commonly used way of defining the strong-motion part is the region between the first and last crossing of a threshold acceleration value, often chosen as 0.5 m/s^2 (Kramer, 1996). For the design earthquakes for Bjørnafjorden, the peak acceleration is only 0.864 m/s^2 which may make this threshold value too high, therefore a threshold for Bjørnafjorden is chosen at 0.1 m/s^2 . To avoid numerical difficulties in the FE modelling, the strong-motion region is extended at each side, so that the shortened acceleration time series starts and ends with zero acceleration. The resulting shortened strong-motion time series for Friuli is shown in Figure 3.2-4. Through this procedure, it is possible to use an accelerogram of only 9.1 seconds, compared to 40.94 seconds if using the entire time series.

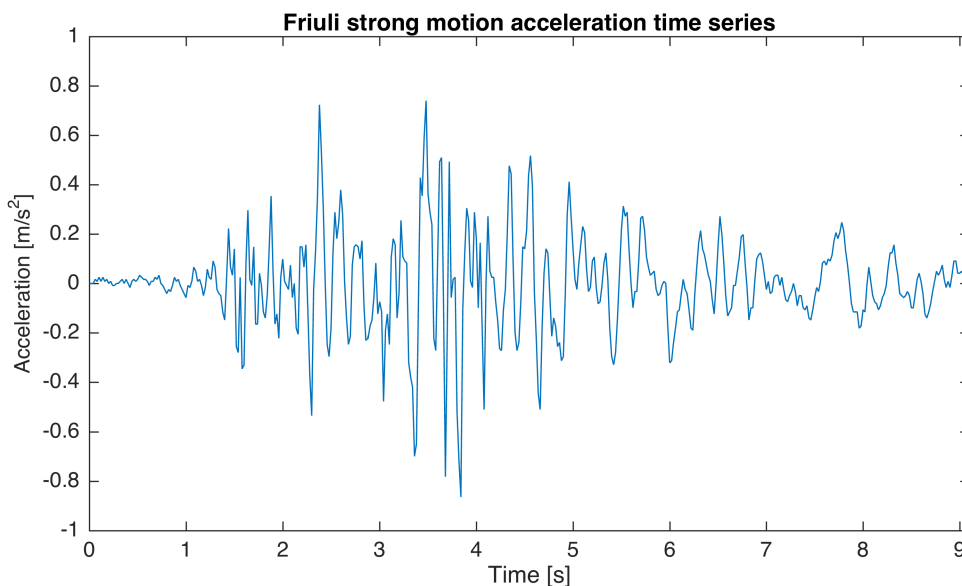


Figure 3.2-4: Shortened strong motion accelerogram for Friuli for use in CPU costly analysis.

3.3 Modelling strategy

The structure is long and relatively slender, with a global height-length ratio of about 0.2 % and height-length ratio between the tethers at about 6 %. By establishing a model of about 10 % of the entire length with 3D-shell elements, including both pipes and the horizontal bracing system, equivalent beam stiffness in lateral directions as well as torsion will be evaluated. These values are then applied to a simplified global 2D and 3D beam model of the SFT.

As the SFT is completely submerged in water, hydrodynamic effects will play a great role in the dynamic response. This is going to be accounted for in the response analysis through added mass and hydrodynamic damping calculated numerically through the software WADAM. Both added mass and hydrodynamic damping will in general be frequency dependent. The drag damping part will be quadratically dependent on relative velocity between the SFT and the fluid. Added mass will change the oscillating mass of the fluid-structure system, and therefore able to change the eigenfrequencies and structural response of the system. Performing an eigenmode analysis on the SFT beam model will give a frequency range for the significant eigenmodes, and thus giving a possibility of choosing frequency dependent added mass, and potentially also frequency dependent hydrodynamic damping.

To refine the beam model to represent the dynamic properties of the SFT adequately with added mass and hydrodynamic damping, a short iterative process is applied. The process can be summarized as follows:

1. Initial eigenmode analysis on the equivalent beam models with a guess on added mass coefficient from theoretical values for a circular cross section.
2. Extract WADAM analysis result on 3D SFT geometry to choose frequency dependent added mass in the frequency range for the vertical eigenmodes with sufficient participating mass of the SFT.
3. Refined eigenmode analysis with updated added mass coefficient
4. Repeat iteration on added mass if necessary
5. Choose a structural model with appropriate hydrodynamic properties for response analysis from seismic motion

4 WADAM modelling

To evaluate the hydrodynamic properties of the SFT an analysis is performed in the DNV Sesame package, using Genie for CAD-purposes, HydroD to set up analysis parameters and finally processing the model through the hydrodynamic solver WADAM. The analysis is focused on gaining accurate information about the hydrodynamic properties of the SFT, through added mass and hydrodynamic damping, by analyzing with both potential flow theory and Morison's equation.

4.1 CAD and meshing

The package Genie is used for creating the model. Two separate models are generated, one Morison model, with simple beam elements used to calculate Morison drag damping, and one meshed panel model to solve for potential flow. A section of length 394 meters is modelled, from center to center between cross tubes. In total, two half cross tubes and one whole is thus included.

4.1.1 Morison beam model

For the Morison beam model, the horizontal bracing system between the pipes is included. All parts, the pipe, cross tubes and bracings are modeled as beams with drag coefficients and area for the different beams applied according to DNV suggestions for different cross sections in offshore structures (DNV, 2010b). DNV gives tabulated values for different cross section parameters, as well as Reynolds number. Using the DNV values for kinematic viscosity of water, characteristic size of the SFT of 13 m height, and a guesstimate of oscillating velocity of the SFT of 0.1 m/s, the Reynolds number according to 2.3.3 is very roughly estimated to approximately 960 000. The applied drag coefficients as well as their corresponding Reynolds numbers as given by DNV are shown in Table 4.1-1.

The beams modeled in Genie for use in WADAM are in principle rigid lines, however, they are assigned cross sections for the analysis, which are rendered for illustration as shown in Figure 4.1-1.

Table 4.1-1: Applied Drag Coefficients for Morison Beam Model.

Parts	C_D	Valid for Reynolds number, Re
Bridge pipes (circular)	1	Re – 100 000
Cross stiffeners (plate)	1.9	Re > 10 000
Cross tubes (rectangular)	2.26	Re – 100 000

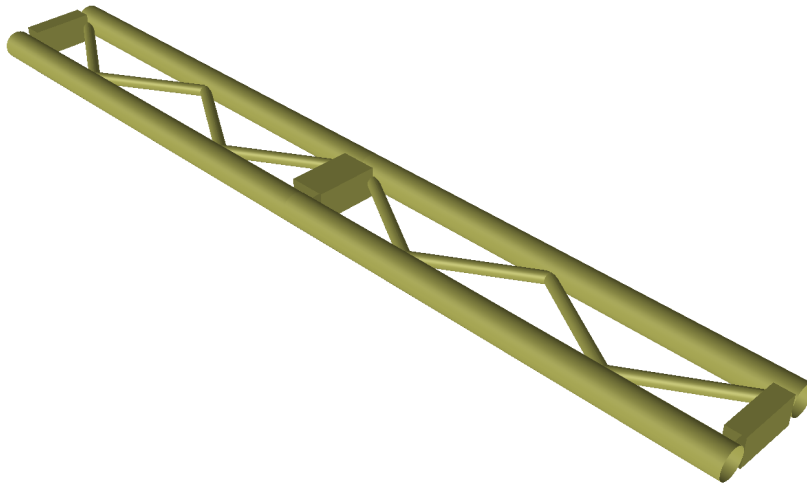


Figure 4.1-1: Morison beam model showed with rendered cross sections.

4.1.2 Panel Model

The panel model is generated to calculate frequency dependent added mass and radiation damping. Since the volume of the horizontal bracing system is small compared to the volume of the pipes and cross-tubes, these are neglected in the panel model, as they will give small impact on the total added mass and radiation damping. The tether corbels on the cross tubes are included, although with simplified geometry as a horizontal plate with straight faces as shown in Figure 4.1-2. The concrete underneath the pipes used to anchor the pre-tension cables is also included, as a simple rectangular box. The panel model is meshed with a mesh size of 2 m. According to WADAM user manual (DNV, 2010c), 8 panel elements should be used per wavelength of the incident wave to be able to sample the wave sufficiently. For panels of 2 m size this therefore corresponds to the panel model giving adequate results for wavelengths of 16m and larger, corresponding to frequencies lower than 0.32 Hz. For results adequate for higher frequencies, smaller panels need to be used, however, the WADAM version available limits the number of panels so performing an analysis with smaller panel mesh is not currently possible.

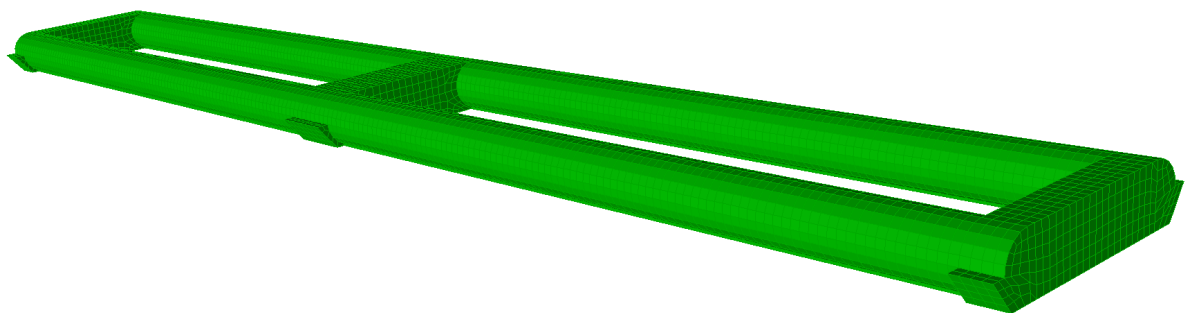


Figure 4.1-2: Meshed panel model from WADAM.

4.2 WADAM results

After setting up input and desired output parameters in HydroD, a WADAM analysis is conducted. An excerpt of input parameters is shown in Table 4.2-1. Both the panel model and the Morison beam model is analyzed. The panel model is solved for potential flow, giving added mass and radiation damping, and the Morison beam model gives drag damping linearized around a chosen velocity.

Table 4.2-1: Input parameters in WADAM model.

Length of modeled section	394 m
Number of panel elements	10404
Average Panel square side size	2 m
Water density	1023 kg/m ³
Sea depth	200 m
Submerged depth to centerline SFT	36 m

WADAM gives added mass in the form of total added mass in kg, and hydrodynamic radiation and drag damping as a force per velocity for the modelled section. By simple geometric considerations, these are converted to more presentable forms, such as added mass coefficient by dividing the added mass value to the displaced water mass of the modeled section. From the panel model, WADAM gives results for added mass and radiation damping for frequencies outside the valid range given in 4.1.2, however, the results are presented only in the valid frequency range. The calculated vertical added mass coefficients are shown in Figure 4.2-1, together with a constant line representing added mass coefficient of 1.1. The calculated horizontal added mass is shown in Figure 4.2-2.

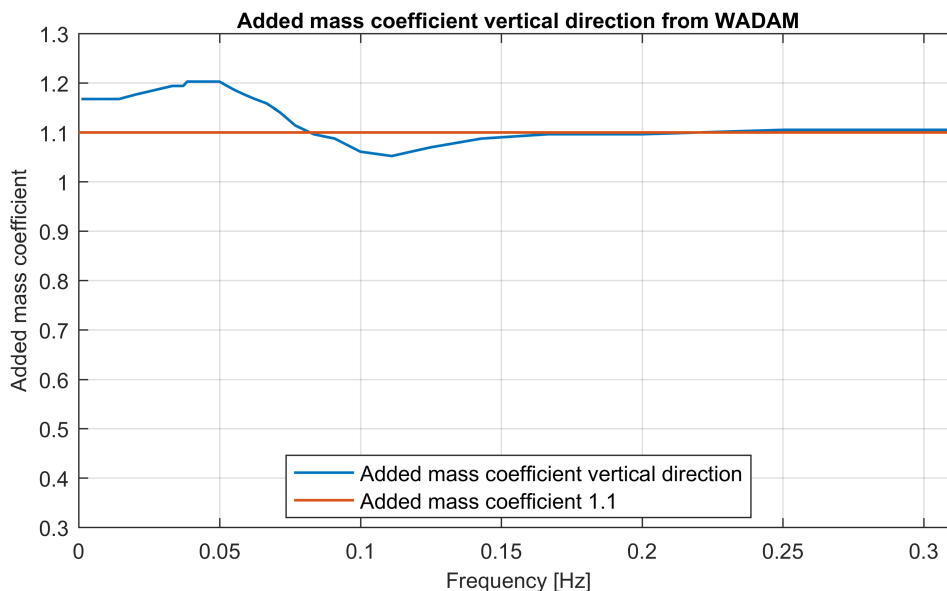


Figure 4.2-1: Calculated frequency dependent added mass coefficient in the vertical direction.

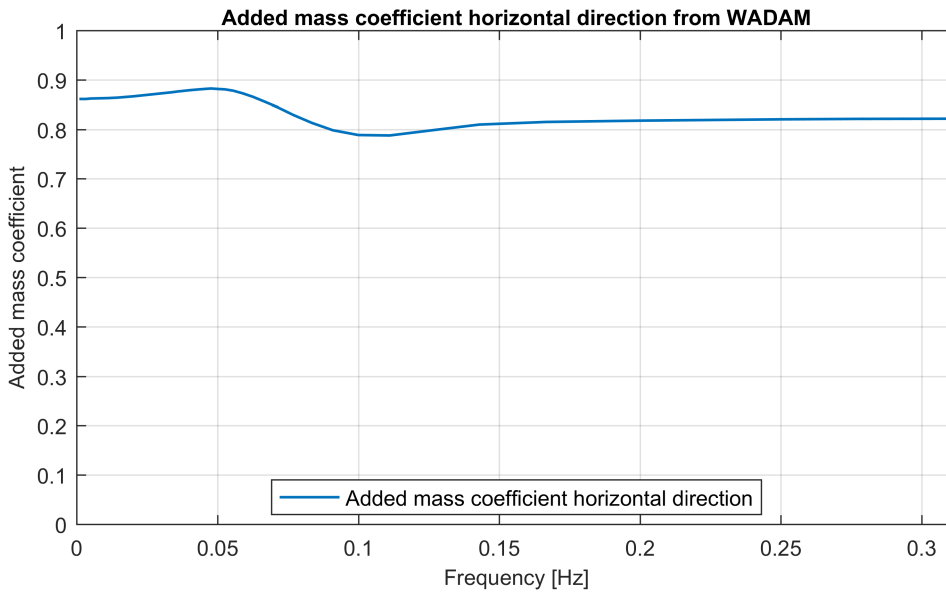


Figure 4.2-2: Calculated frequency dependent added mass coefficient in the horizontal direction.

It can be seen from Figure 4.2-1 and Figure 4.2-2 that for frequencies higher than 0.2Hz, the added mass coefficient is roughly a constant value, both for the horizontal and vertical direction.

Radiation damping is given in a force per velocity, and is adjusted by dividing on section length to give force per velocity and length. As mentioned earlier, the drag damping is calculated from chosen drag coefficients and linearized around a chosen velocity. As a result, when giving the calculated drag damping as a force per relative velocity of the structure, the damping becomes linear with respect to the linearized velocity. The calculated drag damping force linearized around different velocities, is shown together with the calculated radiation damping force with respect frequency in Figure 4.2-3. For both figures, the forces are given per length SFT and per relative velocity. Remark that Morison Damping force is proportional to the linearized velocity, meaning the Morison damping of linearized velocity 1 m/s is 10 times larger than 0.1 m/s.

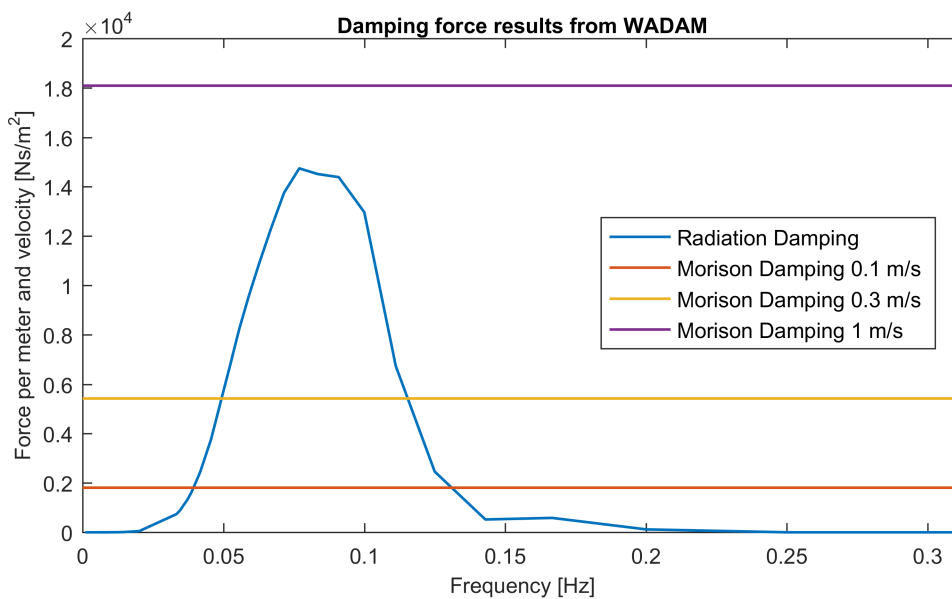


Figure 4.2-3: Radiation damping as a function of frequency. Morison drag damping is shown for different linearized velocities. Note that the force values are given per velocity and meter SFT length.

5 ABAQUS Acoustic Modelling

5.1 Developing acoustic model

A column of acoustic elements assigned with the acoustic properties of seawater in ABAQUS is constructed to verify the behavior of boundary conditions, element types, explicit and implicit methods, and finally to estimate seaquake pressures. An illustration of the column model is given in Figure 5.1-1. Material properties of the water and seabed is given in Table 5.1-1 and finite element acoustic model is given in Table 5.1-2. The properties of the seabed are set to a typical density and p-wave velocity of granite and gneiss, which is reasonable for the west coast of Norway. The sides of the acoustic column model have not been given any boundary condition meaning the sides will not adsorb energy and the wave amplitude should not decrease during propagation through the column for a vertical planar pressure wave. The load is set as a planar incident wave with a prescribed pressure amplitude.

Table 5.1-1: Material properties of acoustic mediums.

Density water	1023 kg/m ³
Speed of sound water	1449.7 m/s
Bulk modulus water	2.15 GPa
Density solid	2500 kg/m ³
Speed of sound solid	5000 m/s
Reflection ratio water and solid as given in chapter 2.2.6	0.788

Table 5.1-2: ABAQUS Acoustic model properties.

Model heights	100-550 m
Base area	5x5 m ²
Element size	1x1x1 m ³
Acoustic element type	AC3D8
Acoustic infinite element type	ACIN3D4
Internodal intervals per acoustic wavelength	28
Critical timestep to avoid aliasing of seismic input	0.01 s
Critical timestep to avoid surpassing an element in water	0.00069 s
Critical timestep to avoid surpassing an element in soil	0.0002 s
Chosen time step	0.0002 s
L _{max} : Maximum length of an element in water with 10 internodal intervals per acoustic wavelength	2.89 m

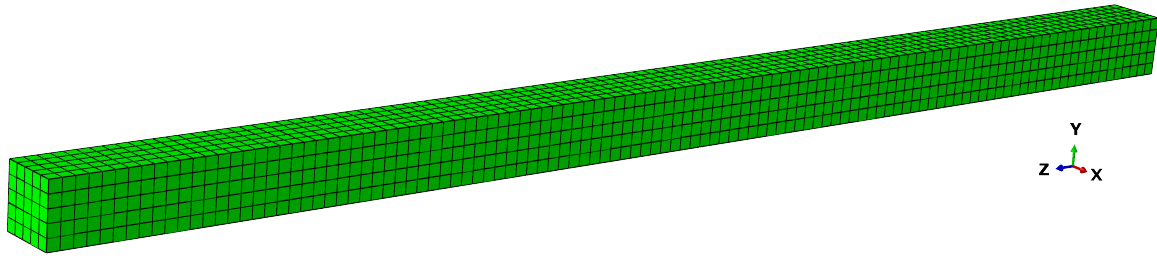


Figure 5.1-1: Illustration of 100 m high acoustic column model in ABAQUS with base area 5x5 m. Cubic mesh size of 1x1x1 m.

A pulse is created with the purpose of illustrating and confirming acoustic properties, boundary conditions and wave propagation in the modelled acoustic medium. The pulse consists of two identical cosine waves of one wavelength and opposite signs. The pulse starts after some time delay to ensure that the acoustic medium behaves well in the simulation before the pulse is applied. The pulse time series is shown in Figure 5.1-2.

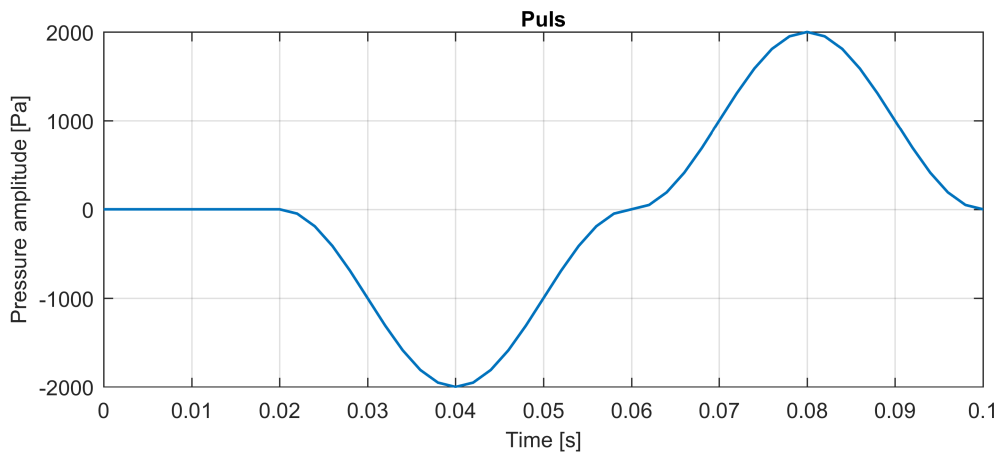


Figure 5.1-2: Two-sided cosine pulse set as load for validation of the acoustic model.

Initially, an implicit analysis of a 100 m high acoustic column with seawater properties is loaded with the incident pulse load without any boundary conditions applied. No boundary conditions in ABAQUS is equivalent to full reflection with equal sign. This model should trap the energy within the column. The pressure is extracted from the simulation at a middle node in the column at each height in the mesh. The pressure at each middle node through the column height is given in Figure 5.1-3, however, due to the sheer number of nodes, resulting in 100 lines, the legend for these are not shown in the figure. The wave is confirmed to propagate at the speed of sound in the medium by consideration of the pulse travelling time between two nodes with a given distance in the model.

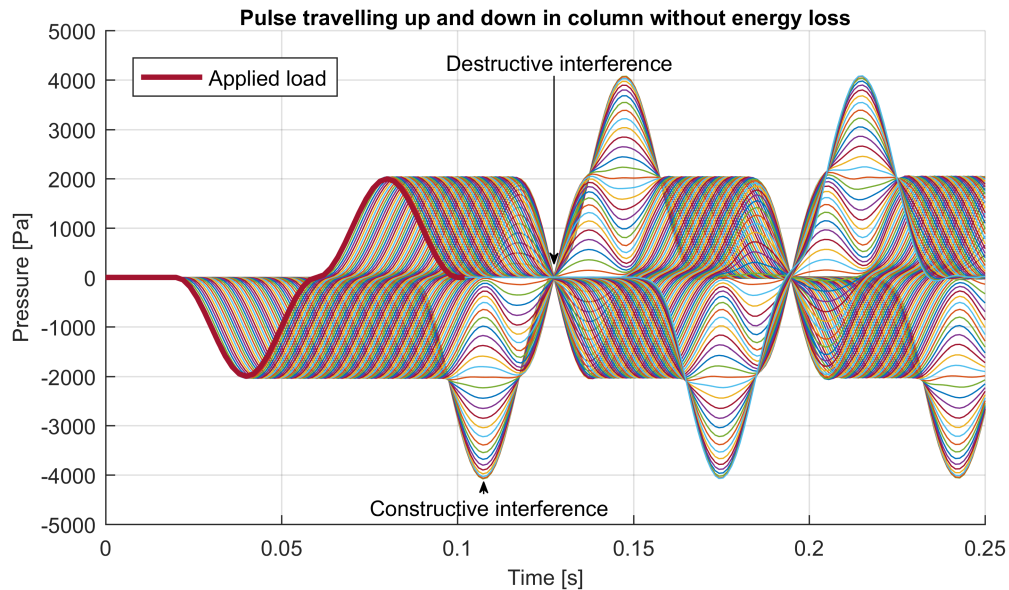


Figure 5.1-3: The applied pulse travelling in the water column without any energy loss. The applied load is shown in the legend, while each of the other lines represents the pressure at a single node at a specific height in the middle of the column. Two time incidents with complete overlap and maximum constructive and destructive interference is indicated with arrows.

It is evident that the positive and negative part of the pulse is reflected at the top and bottom resulting in constructive and destructive interference. When half the first cosine of the pulse is reflected, it overlaps its other half of the cosine still traveling upwards, thus nodes in the overlapping region will experience constructive interference. The same effect happens with the second cosine pulse. At the time incident when the complete first cosine of the pulse is reflected it will overlap with the next cosine of the pulse travelling upwards with different sign, and thus result in complete destructive interference. At this point all nodes in the column should experience zero acoustic pressure.

To model the free surface in the column model, a boundary condition is applied by enforcing zero pressure at the top of the column. This is a common way to model a free surface, equivalent to a boundary where the air is modelled with zero specific impedance, which should result in all energy being reflected, however with opposite sign, and should provide no energy loss upon reflection. Zero pressure is also given as an example of a free surface condition in the ABAQUS manual (Dassault Systèmes Simulia Corp, 2017). In addition, the behavior of infinite element is also investigated by applying infinite elements at the bottom of the column. These elements should in an ideal case transmit all the energy applied to the elements out of the system without any reflections. The energy transmission of the infinite elements finds place when the reflected wave at the top of the column hits the bottom of the column. The pressure at each middle node through the column height for an implicit and an explicit model with infinite elements at the seabed applied the pulse loading is shown in Figure 5.1-4.

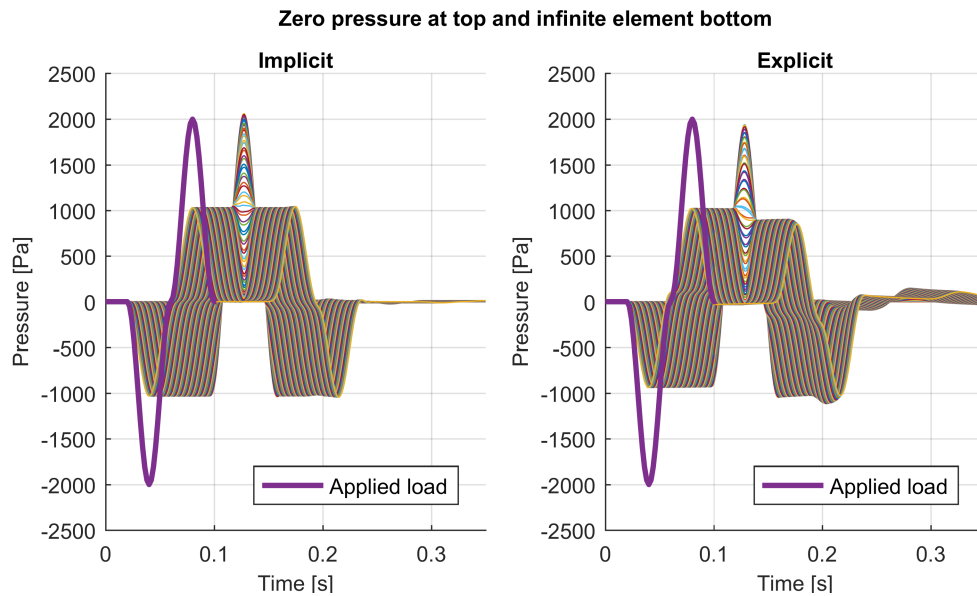


Figure 5.1-4: Comparison of implicit and explicit analysis with boundary of zero pressure at the top and infinite element at the bottom. Note the unsymmetrical pressure shape and reflected energy from infinite elements in the explicit analysis results.

Figure 5.1-4 shows that the infinite bottom boundary in an implicit analysis only transmit roughly 50 % of the energy during loading, however maintaining the shape of the loading for both positive and negative amplitude. This suggests that only a given fraction of the incident wave loading is transmitted into the acoustic fluid elements in the model. This is most likely a numerical phenomenon of the applied boundary condition with infinite elements as the entire incident wave was transmitted when no boundary conditions was introduced in Figure 5.1-3. The implicit method shows symmetric transmissions for positive and negative loading sign, approximately perfect reflection of all energy at the free surface and minor reflections from the infinite elements. The explicit method also gives approximately perfect symmetrical reflections at the free surface, however, the applied loading receives an unsymmetrical pressure wave shape. In addition, considerably more energy is reflected from the infinite elements. The time benefit of using explicit analysis for this model with the same mesh density and linear elements as in an implicit analysis does not seem to be large enough to make up for these undesired effects. This may of course be a different case for larger and more complex models with even higher computational cost, however, implicit analysis is thus chosen as the basis for further analysis with the water column in this thesis.

To account for a more realistic boundary condition at the bottom of the column, the model is refined into two acoustic mediums, one assigned the properties of seawater, and one assigned typical bedrock acoustic properties. The modelling of the bedrock at the seabed is intended to imitate the reflections of the primary waves by the seabed as well as accommodate for the energy transmitted into the bedrock. The boundary condition at the top of the column is still defined with enforcing zero pressure. The resulting pressures in the nodes when subjected to the pulse loading in this refined model is shown in Figure 5.1-5.

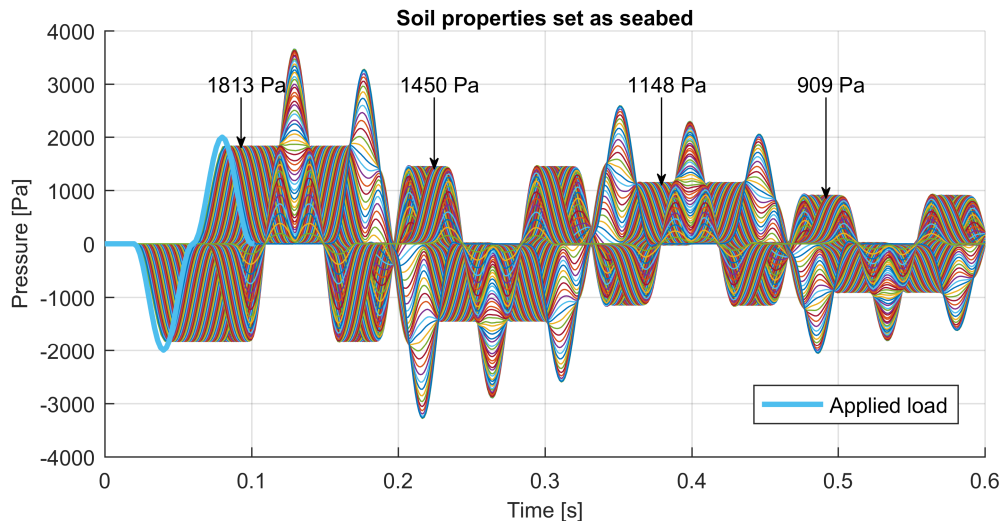


Figure 5.1-5: Pulse load with solid material as seabed and zero pore pressure at free surface. The soil reflects the wave amplitude with 79.2 %, which is the ratio of the pressure each pressure loss of the annotated pressures in the figure. This model is set as basis for the time domain acoustic analysis seaquake.

From the results in Figure 5.1-5, it can be seen that the acoustic seabed reflects 79.2 % of the wave back into the water column, which is the ratio between the pressures at each reflection annotated in Figure 5.1-5. This is close to the reflection ratio given in Table 5.1-1 and the model behavior therefore seems reasonable. Consequently, this model is set as basis for the time domain acoustic analysis of seaquake loading as conducted in chapter 6.5.2. Similar to the previous results in Figure 5.1-4, the bottom boundary only transmits a fraction of the pressure from the incident wave into the water domain, however as soil elements are introduced along with infinite elements, the fraction is changed. This reduction in the loading experienced is accommodated for in the seaquake model simply by scaling with a factor accordingly so the pressure magnitude experienced at the bottom elements of the acoustic water mesh is equivalent to the pressure magnitude of the incident wave.

6 ABAQUS Modelling

6.1 Modelling equivalent stiffness.

The SFT structure is very slender, with a length to width ratio of 15 in the vertical direction in-between the tethers, thus making the simplification of using a beam model to analyze seismic response reasonable. For a satisfactory response analysis, it is necessary that the beam model adequately represent the structural properties of the SFT, including the horizontal brazing system. A 3D section model is generated to find equivalent stiffness for use in the beam model. A shell model was used for computational efficiency compared to solid elements. This is due to the belief that uncertainties in seismic loading and using a beam model with smeared stiffness properties for response analysis negates any potential accuracy gain from applying solid elements for the section model.

6.1.1 The 3D shell element model

A straight section of the bridge with length of 607 meters was modelled with two pipes, interconnected with cross-tube sections according to drawings in chapter 3.1 as well as a truss system between the pipes. The smallest pipe-section was chosen for the entire section model. Emergency-exits are modeled with height equal to the pipe heights. The corbel for the tethers on the emergency exits are not modelled.

The structure is meshed in ABAQUS with S4R type shell elements of average size $1 \times 1 \text{ m}^2$. The elements use reduced integration with hourglass control to avoid shear locking. A simplification is made by not considering the curvature of the bridge elements in this model, as the truss system and emergency exits are thought to have larger impact on the stiffness than the curvature of bridge, especially in the vertical direction where response is of interest in this thesis. The ABAQUS shell model is shown in Figure 6.1-1 and Figure 6.1-2. The geometry of the truss system is simplified to a plate with a thickness corresponding to equivalent axial stiffness of the profiled trusses. The simplified geometry is illustrated in Figure 6.1-3. The shell members of the pipes, cross-tube sections and truss system are given their respective thickness according to the drawings. Material data used for input is previously given in Table 6.1-1.

Table 6.1-1: Equivalent model data.

Model length	607 m
C/C pipes	40 m
Element type	S4R
Integration rule over shell thickness	Simpson
Number of integrations point over shell thickness	5
Number of nodes	60029
Number of Elements	60016
Element size	$\sim 1 \times 1 \text{ m}^2$
Cross-tube section thickness	0.7 m
Pipe thickness	0.8 m
Stiffener thickness	0.836 m

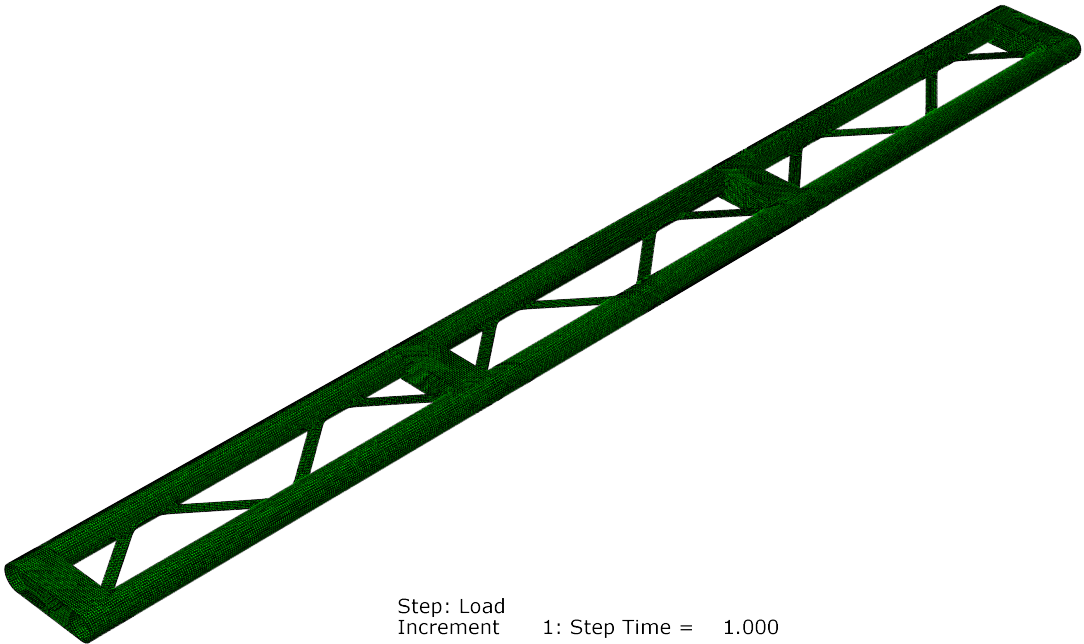


Figure 6.1-1: Equivalent model overview image.

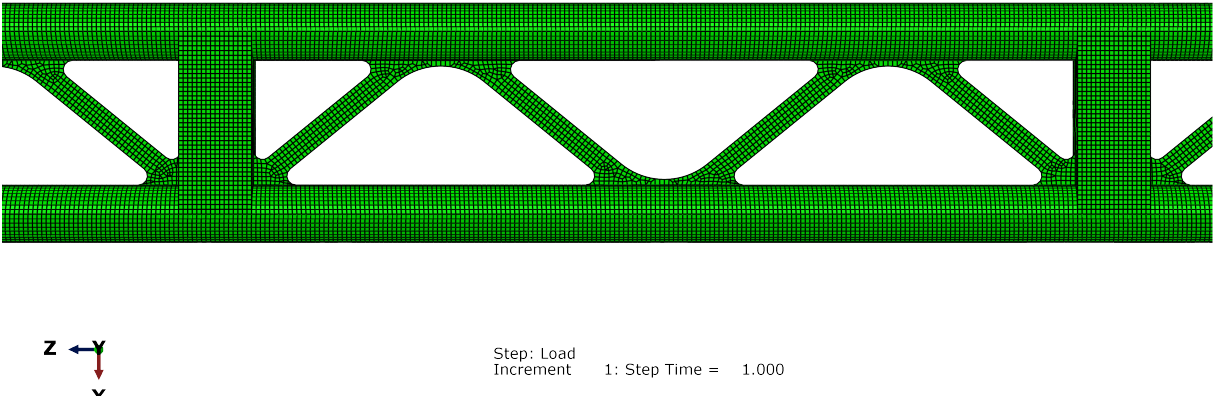


Figure 6.1-2: Equivalent model detailed image.

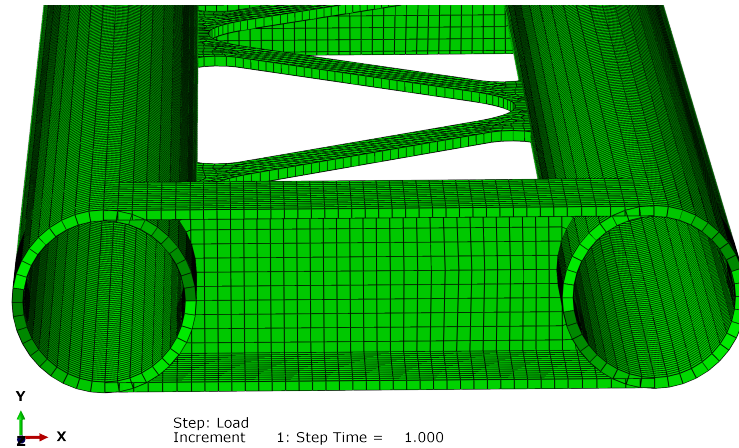


Figure 6.1-3: Illustrations of simplifications made of cross-tube sections and stiffeners in the equivalent model. The shell elements are rendered for illustration. Remark that the rendering of the shell elements creates a graphical, but false overlap between the elements of the pipes and the cross-tube sections.

6.1.2 Equivalent Lateral stiffness

To calculate lateral stiffness, boundary conditions at the ends of bridge section model is applied corresponding to a simply supported beam in horizontal and vertical directions respectively. Force-displacement relationship in the vertical and horizontal direction is prescribed, and solved in two separate linear static analyses. The resulting deformation shapes are shown in Figure 6.1-4 and Figure 6.1-5. The force-displacement results are then correlated with the bending stiffness from elastic analytical solution of the bending of a simply supported beam with distributed load. Inserting for the Young's Modulus of the concrete, the equivalent second moment of inertia for the bridge section is calculated from equation (2.54), originating from Navier-Bernoulli beam theory. In equation (2.54) the symbols are the distributed load q , length L , Young's modulus E , second moment of inertia I and deformation w . Calculated equivalent moment of inertia in both directions are given in Table 6.1-2.

$$w_{y,z} = \frac{5}{384} \frac{q_{y,z} L^4}{EI_{y,z}} \rightarrow I_{y,z} = \frac{5}{384} \frac{q_{y,z} L^4}{E w_{y,z}} \quad (2.54)$$

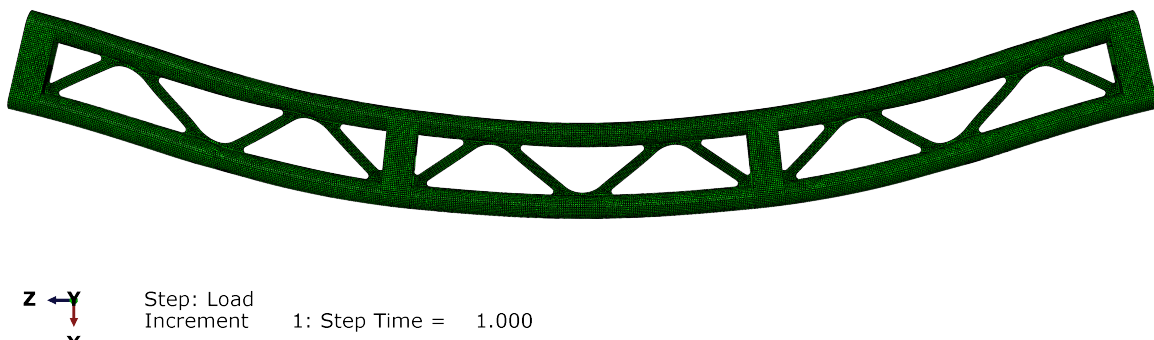


Figure 6.1-4: Resulting deformation shape for equivalent model in horizontal plane.

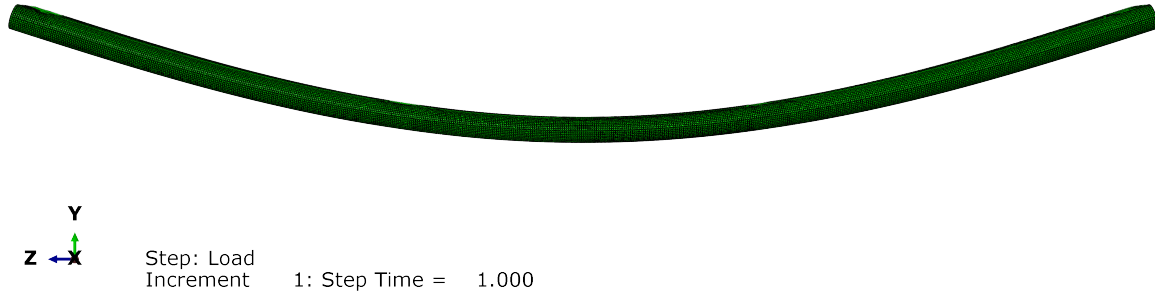


Figure 6.1-5: Resulting deformation shape for equivalent model in vertical plane.

6.1.3 Equivalent torsional stiffness

To calculate the equivalent torsional stiffness of the model, one of the end edges is fixed so that the model can be considered as a cantilever. A torsional moment is then applied to the opposite edge. Rotation at the cross-tube sections are recorded, corresponding to the center of the tether-groups. The resulting deformation shape is shown in Figure 6.1-6. It is central in calculation of the equivalent torsional stiffness of the bridge to include the torsional stiffness of the tethers in a reasonable way. The tether forces are considered as a moment at the center of the bridge girder cross section by the moment equivalency with a pair of forces. The distance between the tethers alternates between 58.4m and 63.3 m. The size of the equivalent moment from the tethers are calculated from the logged rotations at the respective tether location. The moment required to rotate the bridge girder and the tethers are added up, and used in equation (2.55) to calculate the equivalent torsional constant of the model. In equation (2.55) the symbols are angle ϕ , torsional constant I_T , moment M , length L and shear modulus G . The calculations are given in Figure 6.1-7. Remark that the moment required to rotate the tethers are over 15 times larger than the moment needed to rotate the bridge girder the same angle.

$$\phi = \frac{ML}{GI_T} \rightarrow I_T = \frac{ML}{G\phi} \quad (2.55)$$

Several simplifications of the torsional stiffness contributions from the tethers are made. The length of the tethers directly impacts the tether stiffness, and thus also their contribution to the torsional stiffness of the bridge. The length of the tethers is set to 200 m. The torsional stiffness of the bridge will therefore be highly varying along the length of the bridge, as the tethers vary significantly in length. In addition, the tethers will apply concentrated forces, enabling local torsional response in-between the tethers.

These simplifications of the model should be considered when applying it to the equivalent model. The SFT dynamic motions from vertical earthquake and possible seaquake excitation is not expected to excite torsional modes significantly. For simplicity, the equivalent stiffness is therefore chosen to be smeared over the length of the SFT in the simplified 3D beam model. For different dynamic loading scenarios, torsional resistance may be necessary to study in a greater extent, for instance with a full 3D model with solid or shell-elements.

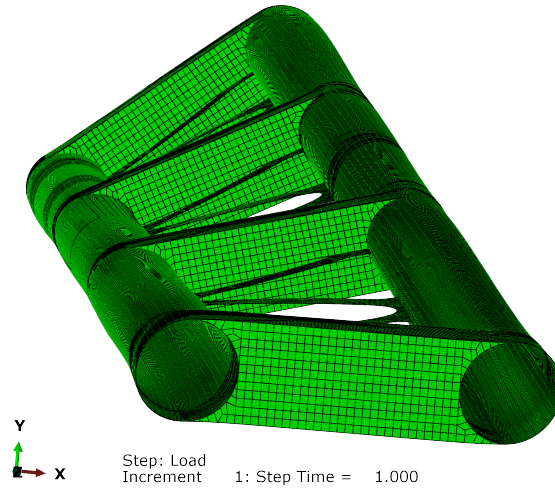


Figure 6.1-6 Resulting deformation shape for the equivalent model with applied torsion.

Torsional equivalent stiffness

$$\begin{aligned}
 E_{tether} &:= 210 \text{ GPa} & L_{beam} &:= 607 \text{ m} \\
 A_{tether} &:= 2 \cdot 0.129 \text{ m}^2 & G_{beam} &:= 15.83 \text{ GPa} \\
 L_{tether} &:= 200 \text{ m} \\
 \\
 a_1 &:= 63.3 \text{ m} & \theta_1 &:= 5.342 \cdot 10^{-6} \\
 a_2 &:= 58.4 \text{ m} & \theta_2 &:= 1.001 \cdot 10^{-5} \\
 a_3 &:= 63.3 \text{ m} & \theta_3 &:= 1.510 \cdot 10^{-5}
 \end{aligned}$$

$$M_1 := \frac{E_{tether} \cdot A_{tether} \cdot a_1^2}{2 L_{tether}} \cdot \theta_1 = (2.899 \cdot 10^6) \text{ N} \cdot \text{m}$$

$$M_2 := \frac{E_{tether} \cdot A_{tether} \cdot a_2^2}{2 L_{tether}} \cdot \theta_2 = (4.624 \cdot 10^6) \text{ N} \cdot \text{m}$$

$$M_3 := \frac{E_{tether} \cdot A_{tether} \cdot a_3^2}{2 L_{tether}} \cdot \theta_3 = (8.195 \cdot 10^6) \text{ N} \cdot \text{m}$$

$$M_{beam} := 10^6 \text{ N} \cdot \text{m}$$

$$M_{tot} := M_1 + M_2 + M_3 + M_{beam} = (1.672 \cdot 10^7) \text{ N} \cdot \text{m}$$

$$I_T := \frac{M_{tot} \cdot L_{beam}}{G_{beam} \cdot \theta_3} = (4.24556 \cdot 10^4) \text{ m}^4$$

Figure 6.1-7: Calculation of torsional constant

Table 6.1-2: Equivalent Model results.

Applied $q_{\text{horizontal}}$	12600 N/m
$w_{\text{horizontal}}$	0.0293 m
$I_{\text{horizontal}}$	19880 m^4
Applied q_{vertical}	12600 N/m
w_{vertical}	0.582 m
I_{vertical}	1268.9 m^4
Applied $M_{\text{torsional}}$	1.672E7 Nm
θ	1.510E-05 radians
I_T	42456 m^4

6.1.4 Validating equivalent stiffness

To evaluate the result from the equivalent model, comparison with simplified hand calculated results can be used. An upper bound for the horizontal stiffness can be calculated from linear Navier-Bernoulli beam theory for two pipes bending as if it was a single beam section. Similarly, a lower bound would be the stiffness of two pipes bending separately with no interaction. In the vertical direction, the stiffness should be somewhat higher than the stiffness for two pipes without interaction, due to stiffness contribution from the bracing system and cross beams. The results of the simplified Euler-Bernoulli calculations are shown in Figure 6.1-8.

Second Moment of Inertia of two adjacent pipes

$$R_o := 6.3 \cdot m \quad D_o := 12.6 \cdot m \quad R_i := 5.5 \cdot m \quad D_i := 11 \cdot m$$

$$A_{\text{pipe_net}} := \frac{\pi}{4} \cdot (D_o^2 - D_i^2) = 29.657 \text{ m}^2$$

$$I_{\text{pipe}} := \frac{\pi}{4} \cdot (R_o^4 - R_i^4) = 518.546 \text{ m}^4$$

$$\text{Distance}_{\text{pipes}} := 40 \cdot m$$

$$\text{SteinerTheorem}_{\text{horizontal_pipes}} := A_{\text{pipe_net}} \cdot \left(\frac{\text{Distance}_{\text{pipes}}}{2} \right)^2 = (1.186 \cdot 10^4) \text{ m}^4$$

$$I_{\text{Horizontal}} := 2 \cdot I_{\text{pipe}} + 2 \cdot \text{SteinerTheorem}_{\text{horizontal_pipes}} = (2.476 \cdot 10^4) \text{ m}^4$$

$$I_{\text{vertical}} := 2 \cdot I_{\text{pipe}} = (1.037 \cdot 10^3) \text{ m}^4$$

Figure 6.1-8: Calculations of second moment of inertia of two adjacent pipes for comparison with the equivalent model.

The results show a horizontal stiffness 20 % lower than the upper bound, and 20 times larger than the lower bound. This indicates that the bracing system is very effective in the horizontal direction, as the stiffness is very close to the upper bound for complete interaction between the pipes. In the vertical direction, the stiffness is roughly 23 % higher than the stiffness of two independent pipes.

The calculated equivalent stiffness are in accordance with the expected behavior of the bracing system and the cross tubes. Horizontal stiffness is greatly increased with the bracing system, while the vertical stiffness is only marginally larger than for two separate pipes. The resulting bending shapes look reasonable, with the vertical deformation shape in Figure 6.1-5 appears pretty much like a typical uniform beam in bending. For the horizontal deformation shape in Figure 6.1-4, the general deformation shape is also that of a uniform beam in bending, although with some influence from the stiff cross beams affecting the regions between the cross beams to also bend somewhat like a shear frame.

The torsional stiffness equivalent model, as previously mentioned, is strongly dependent of the tethers. In the assumptions of the calculations of the torsional stiffness in Figure 6.1-7, the bridge girder only contributes to about 6 % of the stiffness. Since the tethers contribute significantly, the equivalent torsional stiffness is harder to validate. However, since the 3D shell model behaves as expected in both horizontal and vertical directions, the 3D shell model should behave well enough to be sufficient for estimating the torsional constant as done in Figure 6.1-7, with the simplification of smearing the torsional constant over the beam length.

6.2 Beam models

An initial 2D beam model is created in the vertical-axial plane with the length of the bridge corresponding to the actual curved length of the bridge. The model is shown in Figure 6.2-1. Similarly, a model is also constructed in 3D beam elements accounting for the curvature of the bridge, shown in Figure 6.2-2. For both models, only one beam element is used in the width direction, with interaction between the pipes accounted for by the equivalent moment of inertia. For both models, the tether-groups at each section are modelled as a single tether with properties equivalent to the four tethers in the group. Second moments of inertia as well as torsional constant is chosen according to the results in chapter 6.1.

The end anchors are constrained as fixed, while the tethers are modeled as hinged both in the connections to the bridge and the connection to the seabed. Structural and hydrodynamic damping are disregarded in the initial model. The net buoyancy of 10 % is applied as concentrated forces in bridge nodes connected to the tethers. This is in equilibrium with the applied initial prestress of 108 MPa in the tethers. Added mass is applied by changing the density of the pipe, by adding the mass of the displaced water volume multiplied with a factor of 1.0, corresponding to theoretical added mass coefficient for a pipe in Figure 2.3-1. The results is set as basis for frequencies to evaluated in WADAM.

Refining the density of the SFT is based on the WADAM results given in chapter 4.2, which give an added mass coefficient of 1.1. A new linear perturbation eigenmode analysis is then conducted on the 3D beam model with the updated added mass coefficient.

For the eigenmode analysis, the tethers are modelled as single elements in their length direction, since vibration modes in the tethers are of little interest. However, for use in the dynamic analysis with ground excitations, the tethers are made up of multiple elements to allow stress waves to propagate in a realistic manner. All presented results and figures of the SFT are given with the south end of the bridge to the left and the north end to the right.

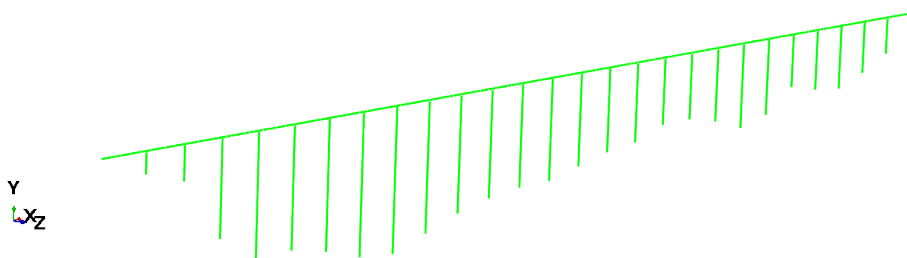


Figure 6.2-1: ABAQUS 2D beam model of the SFT.

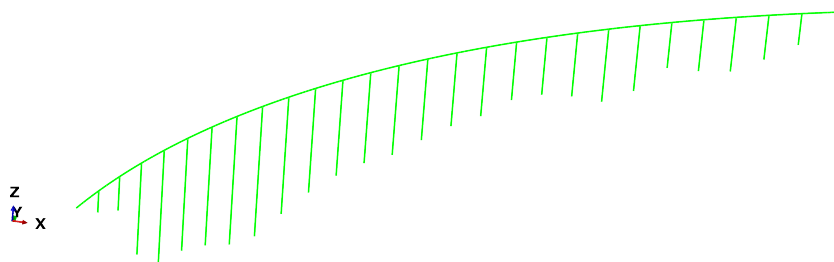


Figure 6.2-2: ABAQUS 3D beam model of the SFT.

6.2.1 Eigenmode analysis

Using the beam models, a linear frequency perturbation step in ABAQUS is used to extract the eigenmodes and eigenfrequencies. After the initial eigenmode analysis, refined added mass coefficient was estimated for relevant frequencies according to chapter 4.2. Eigenmodes are calculated both for the 2D initial, 3D initial, 3D with refined added mass and 3D dry beam model for comparison of eigenmodes and eigenfrequencies. The key input parameters for the eigenmode analysis are shown in Table 6.2-1. There are some axial modes occurring in the 2D model, and several horizontal and axial modes as well as some torsional modes in the 3D analysis results. The effective masses in the vertical direction are extracted of all beam models for comparison.

The 3D model with refined added mass is chosen for further investigation of earthquake response, due to accounting for the effect of curvature and torsion. In addition, the 3D model has adaptability of studying ground acceleration in all three directions.

Table 6.2-1: Key input parameters for eigenmode analysis.

	2D modell	3D modell
Element type girder	B21	B31
Element type tethers	T2D2	T3D2
Total number of beam elements B31	218	218
Tether elements T2D2	27	27
Avg. size of B21 elements	25m	25m
Density in pipe including added mass coefficient of 1.0	9238	9238
Density in pipe including added mass coefficient of 1.1	-	9724
Density in pipe including added mass coefficient of 0.0	-	4376
Number of eigenmodes extracted	200	200

The effective masses are divided by the total mass of the structure, and a plot of the accumulated effective mass ratio in the vertical direction as a function of frequency is shown in Figure 6.2-3. Accumulated effective mass ratio for all the analyzed models are given in the figure. The dominating frequency area of the wet SFT eigenmodes are in the area between 0.2 Hz and 0.5 Hz. The vertical effective masses are distributed over a few vertical modes, the accumulated effective masses surpass 80 % after just 15 vertical eigenmodes and 97 % after 28 vertical modes. The 2D and 3D model with added mass coefficient 1.0 are almost identical as shown in Figure 6.2-3, which implies that the horizontal curvature does not affect the vertical excitation to a great extent. The dry analysis has considerable higher eigenfrequencies because of the lower mass. The 90 % line of accumulated effective mass ratio is given in the graph. This is to illustrate the requirement given for modal analysis in EC8, where all modes used in a modal analysis need to have an accumulated effective mass of at least 90 % of the total mass of the structure. In addition, all modes with more than 5 % effective mass ratio need to be included. For this thesis only time domain response analyses of the full system are conducted.

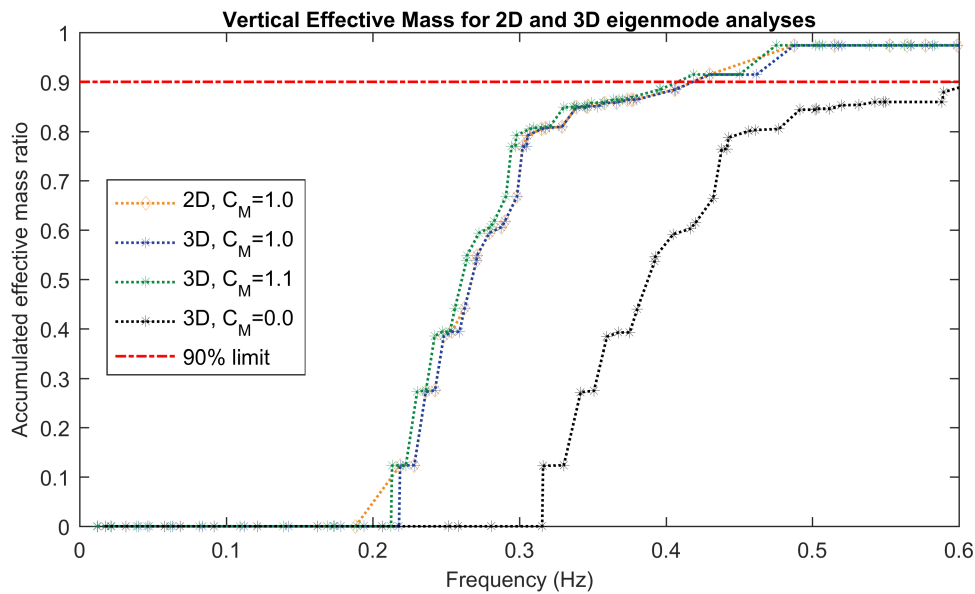


Figure 6.2-3: Accumulated effective mass ratio in vertical direction.

Table 6.2-2 gives the 28 first vertical eigenmodes with corresponding eigenfrequency and effective mass relative to total mass for the 3D analysis with refined added mass. It is worth noting that the highest single effective mass for the remaining higher modes is 0.25 % of the total mass.

Table 6.2-2: Vertical eigenmodes with corresponding eigenfrequency and effective mass.

Vertical mode	Eigenfrequency [Hz]	Effective mass ratio
1	0.213	12.30 %
2	0.223	0.11 %
3	0.230	14.87 %
4	0.236	0.32 %
5	0.242	10.95 %
6	0.247	0.85 %
7	0.256	4.77 %
8	0.264	9.63 %
9	0.264	1.06 %
10	0.272	4.57 %
11	0.280	1.18 %
12	0.283	1.19 %
13	0.291	5.00 %
14	0.295	10.14 %
15	0.298	2.235 %
16	0.307	1.342 %
17	0.310	0.219 %
18	0.321	0.220 %
19	0.330	3.930 %
20	0.337	0.000 %
21	0.338	0.166 %
22	0.349	0.67 %
23	0.357	0.10 %
24	0.364	0.57 %
25	0.368	0.02 %
26	0.396	2.03 %
27	0.419	3.05 %
28	0.475	5.92 %
Sum EM first 28 modes		97.41 %
Sum EM 200 extracted modes		98.62 %

The eigenmode analysis show highly local eigenmodes. The first vertical eigenmodes appear in the area with the deepest water thus softest tethers, as shown for the three first modes in Figure 6.2-4. These local modes have similarities to those of a simply supported beam with the first mode being similar to a sinusoidal half-wave, the second a full wave, the third one and a half wave, etc. At both ends of the bridge, a couple of local vertical eigenmodes with high eigenfrequency and significant masses are found. All these eigenmodes are shown in Figure 6.2-5. The first 28 vertical eigenmodes are given in the appendix.

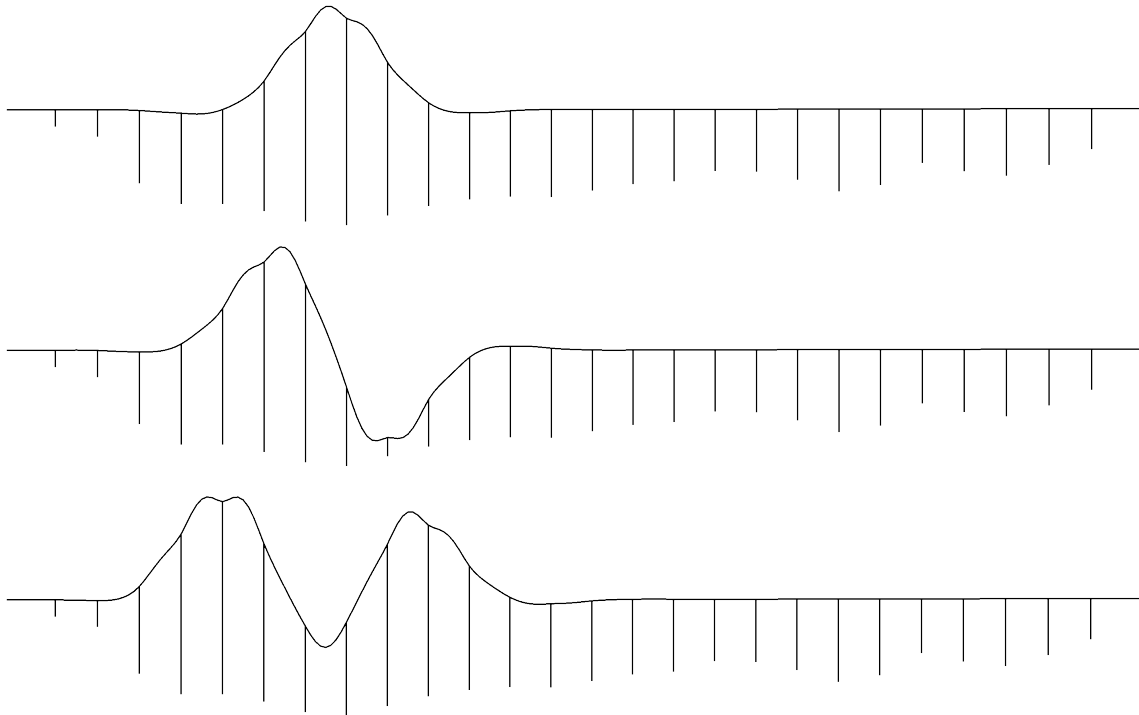


Figure 6.2-4: Illustration of the three first eigenmodes. Corresponding eigenfrequency and effective mass are given in Table 6.2-2.

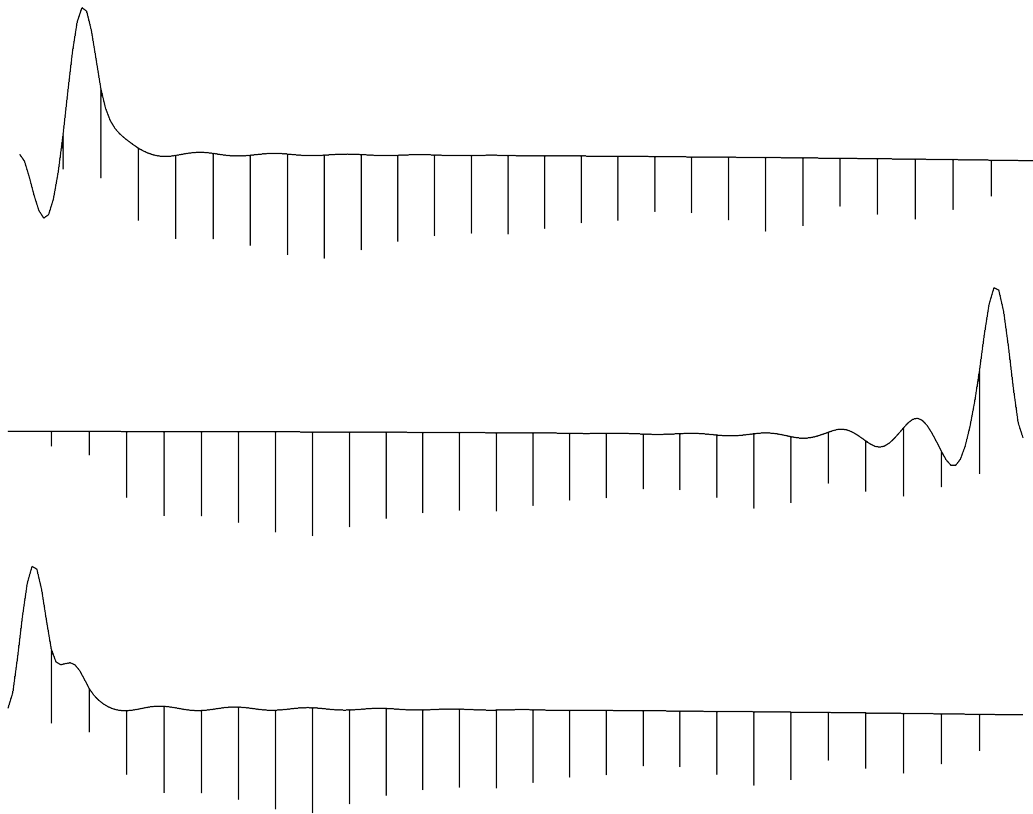


Figure 6.2-5: Illustration of local vertical eigenmodes near shore, number 26 (upper), 27 (middle) and 28 (lower). Corresponding eigenfrequency and effective mass are given in Table 6.2-2.

6.2.2 Applying structural damping

According to the bridge guidelines from NPRA (NPRA, 2015) a critical damping ratio of uncracked concrete bridges can be set to 0.8 %. Due to water tightness assuming uncracked concrete is reasonable, however this value inherently possesses some uncertainty and the actual value may be lower. It is worth noting that cracked concrete will give higher damping ratios, and some cracking may be accepted in the case of a significant earthquake. Nevertheless, the critical damping ratio is set to 0.8% for the beam model of the SFT. Zero damping in the vertical direction is assumed in the tethers. The structural damping is applied as Rayleigh damping, enforced at frequencies of 0.2 Hz and 0.5 Hz, assuring artificially high damping ratios are not occurring in the frequency range of the eigenmodes with high effective masses. The applied Rayleigh damping is shown in Figure 6.2-6.

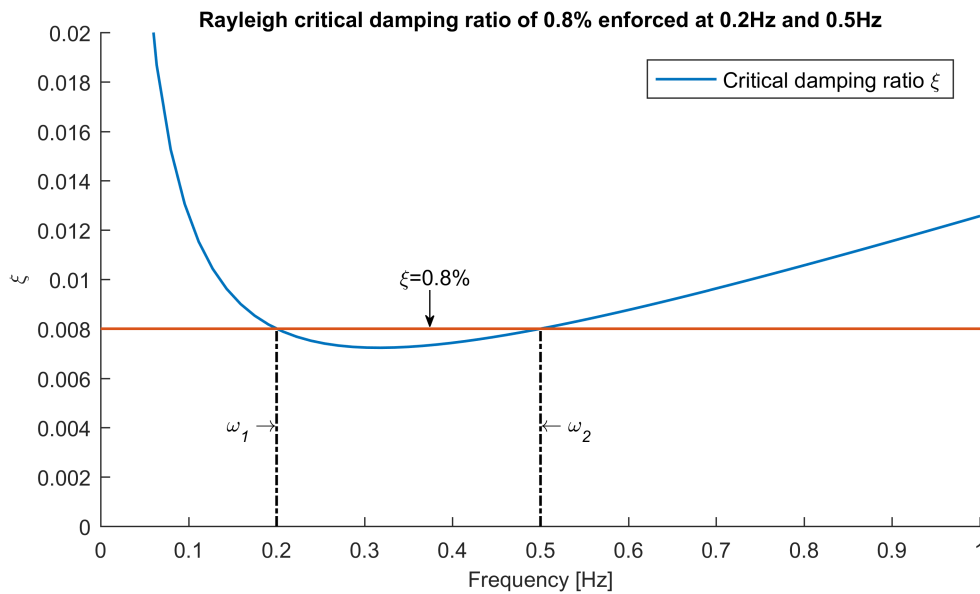


Figure 6.2-6: Applied structural critical damping ratio of 0.8 % enforced at 0.2 Hz and 0.5 Hz.

6.3 Time series response analyses

The response of the beam model to seismic motion is investigated through dynamic explicit analyses. The initial model is used with 0.8 % damping and 1.1 in added mass coefficient, given in Table 6.3-1, ignoring any hydrodynamic damping. An element-by-element automatic stability time integration scheme is used, with the maximum time increment limited to 0.6 ms. The tethers are modelled with element length so that waves of 25 Hz are represented over approximately 12 tethers, which should be sufficient to avoid aliasing and to represent the propagating wave adequately. The duration of the earthquake time series is 40.94 s, and highest frequency content is 25 Hz. The analysis is extended 100 seconds to capture structural response occurring after the earthquake. To reduce the impact of numerical round off error for such a long explicit analysis, ABAQUS double precision is used. The field variables are recorded at all girder nodes and girder elements, as well as the upper and lower elements of the tethers.

Table 6.3-1: Beam model properties

Max time increment	0.6 ms
Wave propagation in tethers per 0.6ms	3.1 m
Shortest tether element	5 m
Wavelength in tethers, 25 Hz	58 m
Prestress tethers	108 MPa
Added mass coefficient	1.1
Structural Rayleigh damping set at 0.2 Hz and 0.5 Hz	0.8 %
Estimated critical time increment of ABAQUS	0.9 ms

6.3.1 Spatial response of the initial model

The results from the response of the three time series analyses in ABAQUS are processed in Matlab, and peak values in each direction of the extracted field variables for each node or element at coordinates along the curved bridge length are extracted. The upwards direction is defined as positive. The resulting peak displacement, velocity and acceleration of the bridge nodes are shown in Figure 6.3-1, Figure 6.3-2 and Figure 6.3-3, respectively.

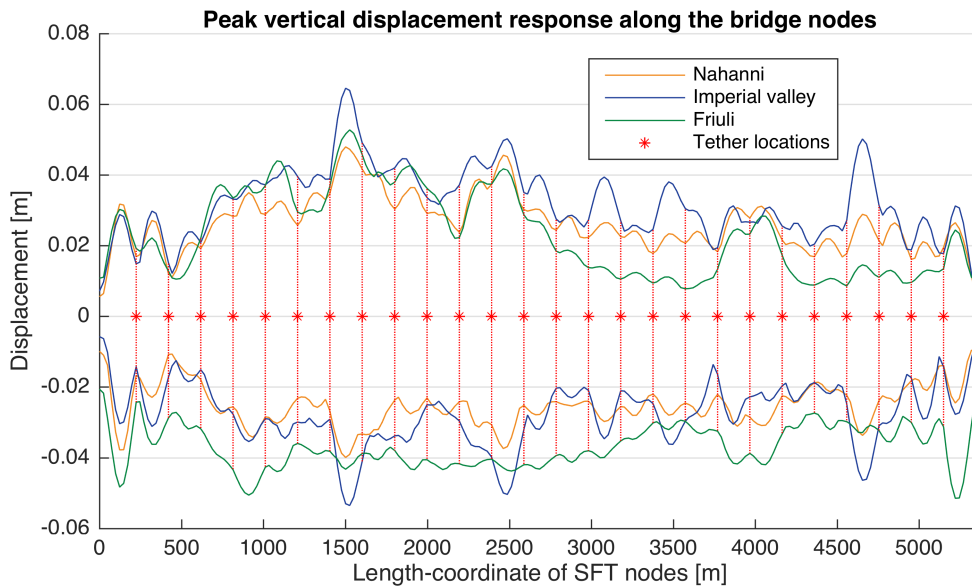


Figure 6.3-1: Peak vertical displacements along the SFT bridge nodes for the three different earthquake series. Note that the maximum displacements for the earthquakes are equal to those at the ends of the bridge as these are applied the ground motion.

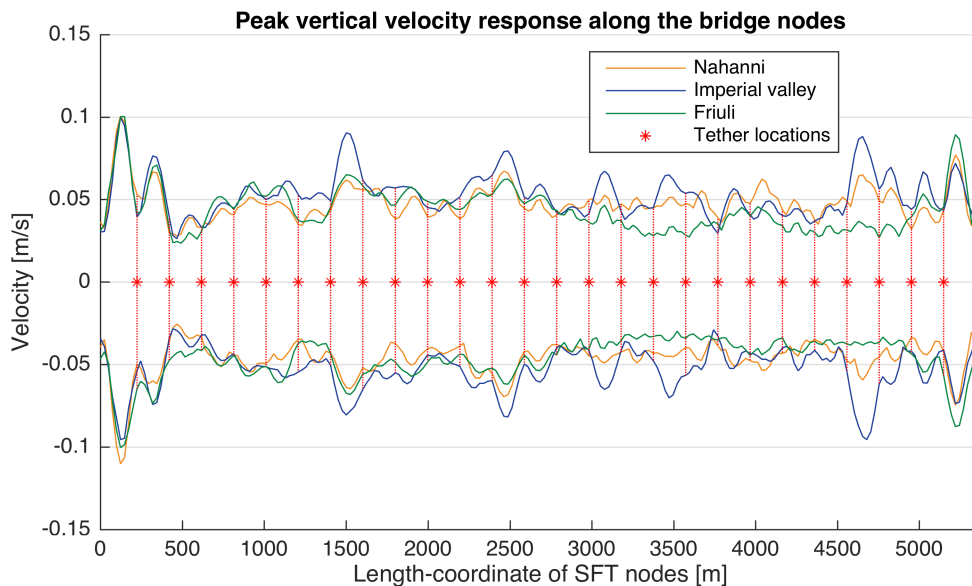


Figure 6.3-2: Peak vertical velocity along the SFT bridge nodes for the three different earthquake series. Note that the maximum velocities for the earthquakes are equal to those at the ends of the bridge as these are applied the ground motion.

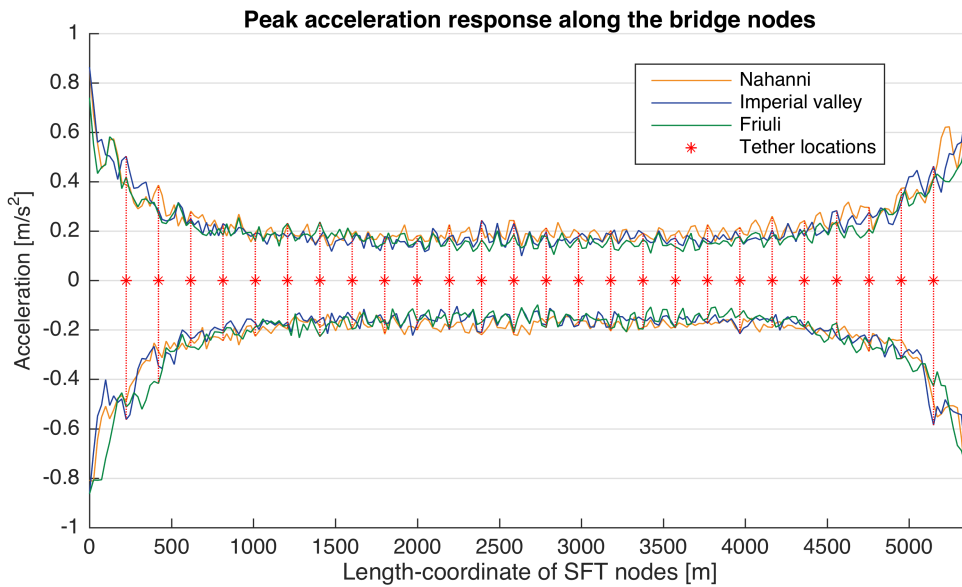


Figure 6.3-3: Peak vertical acceleration along the SFT bridge nodes for the three different earthquake series. Note that the maximum acceleration for the earthquakes are equal to those at the ends of the bridge as these are applied the ground motion.

The results show that the peak displacements of the SFT are amplified compared to the ground motion. The tethers oppose relative displacements with the seabed, and therefore restrain the displacements. As expected this effect can be seen since the peak displacements often show local minimums at or close to the tether locations, and local maximums between the tethers. Note that it is about 200 m between the consecutive tethers, and thus the vertical curvature of the SFT between the tethers is small, even though the scale of the x and y-axis in the figure may give another impression. The peak velocities show some local peaks at the ends of the SFT, particularly at the left end, where the tethers are the shortest. The peak accelerations for the initial model are de-amplified all along the bridge, as can be seen from the results in Figure 6.3-3. The peak accelerations occur at the ends of the SFT, where they are fixed to the base.

6.3.2 Section response of the initial model

From the initial response analysis, sectional forces and stresses are extracted in a similar fashion to the spatial response properties. The peak stresses in the top elements of the tethers is plotted along the SFT length and is shown in Figure 6.3-4. Since tether stiffness affects the stress in the tethers, and is inversely proportional to length, the respective tether lengths are shown in Figure 6.3-5 for illustration.

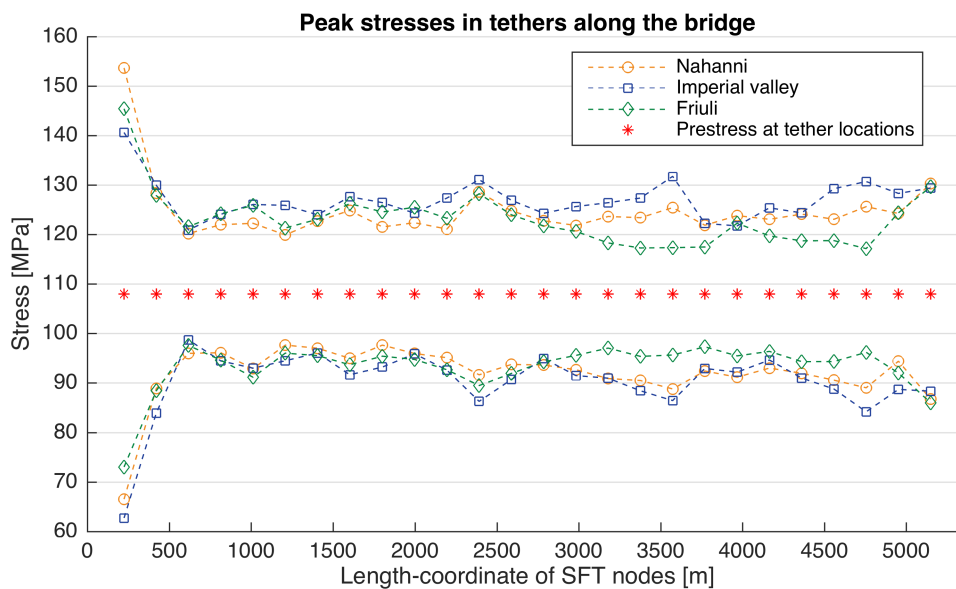


Figure 6.3-4: Peak stresses in the top tether elements along the SFT length nodes for the three different earthquake series, together with the prestressing tension in the tethers. Tension is defined as positive stresses.

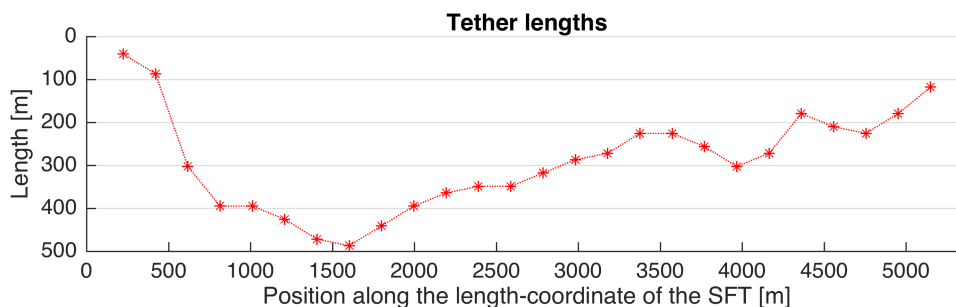


Figure 6.3-5: Tether length along their position on the SFT length.

From the results in Figure 6.3-4, it is shown that stress in the tethers varies a lot along the beam, with the first tether to the left showing high deviations from the applied pretension. The peak values of the stresses are largest in the first tether from the left, which is also the shortest tether, as shown in Figure 6.3-5. The peak stresses in this tether deviate roughly 46 MPa from the applied pretension of about 108 MPa. It can be seen from the results that for the first tether, Nahanni gives large deviations from the initial prestress in both directions.

The shear force response in the bridge elements is extracted from the bridge beam elements. The shear stresses in the centerline of the cross section are estimated from linear bending theory in order to be able to relate the shear forces to shear stresses. The resulting peak shear stresses are shown in Figure 6.3-6.

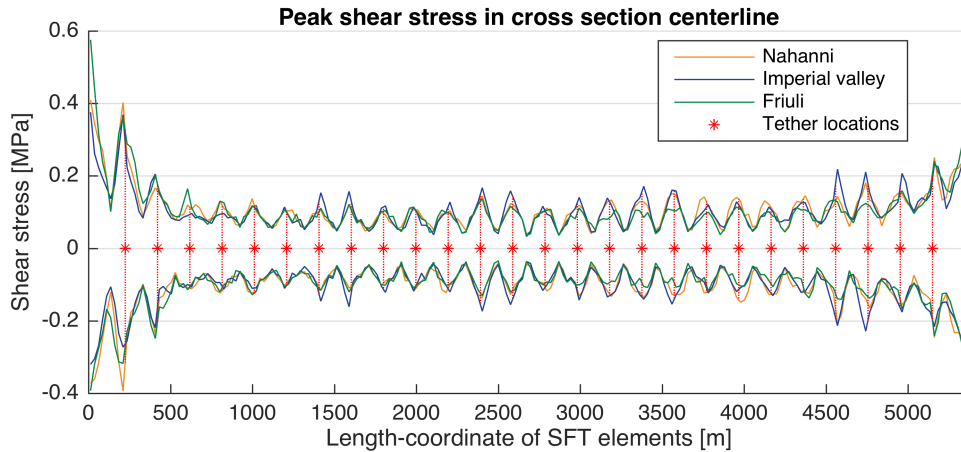


Figure 6.3-6: Peak shear stress in the cross-section centerline along the SFT bridge elements for the three different earthquake series.

The resulting shear stresses in the beam are shown to be quite small, with a maximum value at the left end of 0.6 MPa. For design to peak shear stresses only the maximal values are of interest regardless of sign, as this is a result of the sign convention used in the modelling. The shear stresses behave as expected with peak values towards the ends and the supports at the tethers. It can be seen that global shear stresses in the cross section from the seismic motion applied in this analysis are low and therefore not critical for the cross section of the structure.

Similar to shear stresses, the extracted stress from bending in the vertical plane is converted to bending stresses at the top and bottom of the SFT through linear Euler-Bernoulli bending theory, using the equivalent second moment of inertia according to the results in chapter 6.1. The resulting peak bending stresses for bending in the vertical plane along the length of the bridge is shown in Figure 6.3-7. Positive bending stresses indicate tension in the top of the cross-section and compression in the bottom, while the negative bending stresses indicate the opposite.

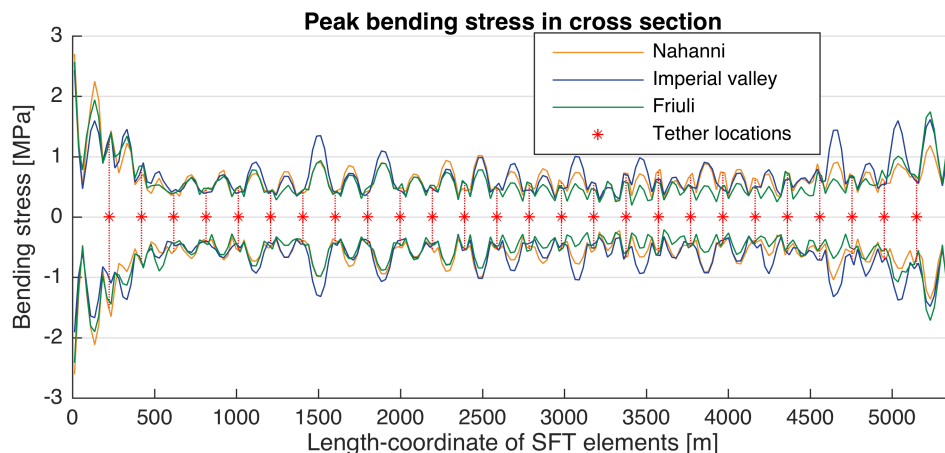


Figure 6.3-7: Peak bending stress in the cross-section along the SFT bridge elements for the three different earthquake series. Positive values indicate tension in top of the cross section, while negative values indicate tension in the bottom.

The resulting bending stresses are in general low, with maximum values of 3 MPa at the left end. With respect to cracking and reinforcement in the concrete, it is not necessarily equivalent which side positive and negative bending stresses occur on. However, the bending stresses from the vertical seismic excitation seem to be quite symmetric, giving approximately the same bending stresses in tension both in the bottom and top of the cross section.

A similar approach to moment and shear is applied to the torsional response of the SFT beam. The torsional shear stresses of the initial beam model are calculated from the torsional moments by assuming the two pipes act as closed sections and are solely responsible for the entire torsional moment of the beam. The resulting torsional stresses are shown in Figure 6.3-8.

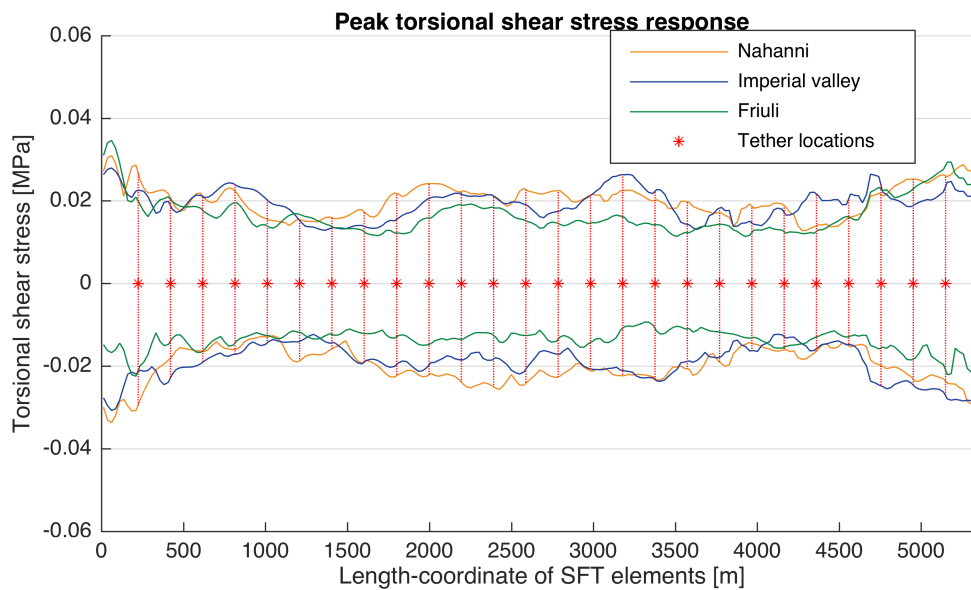


Figure 6.3-8: Peak torsional shear stresses assuming the internal torsional moment is due to shear stresses according to two closed pipe cross sections.

The resulting torsional shear stresses in Figure 6.3-8 are vanishingly low, with maximum values below 0.04 MPa at the fixed ends. Torsional shear stresses will therefore most likely be of little to no importance to the SFT when only subjected to vertical seismic excitation. The representation of the torsional resistance of the SFT has however been applied as a smeared torsional resistance along the beam, and the effects of this will be studied further in a sensitivity study in subchapter 6.4.2.

6.3.3 Behavior in the stiffest tether

From the results of the initial response analyses on the SFT beam model, it is evident that most section stresses are low, except for the oscillations in the tether stresses. The largest oscillations in tether stresses occur at the two tethers closest to the south end of the bridge. To better evaluate the dynamic behavior in this region of the SFT, the response-history of the stress in the shortest tether is shown in Figure 6.3-9.

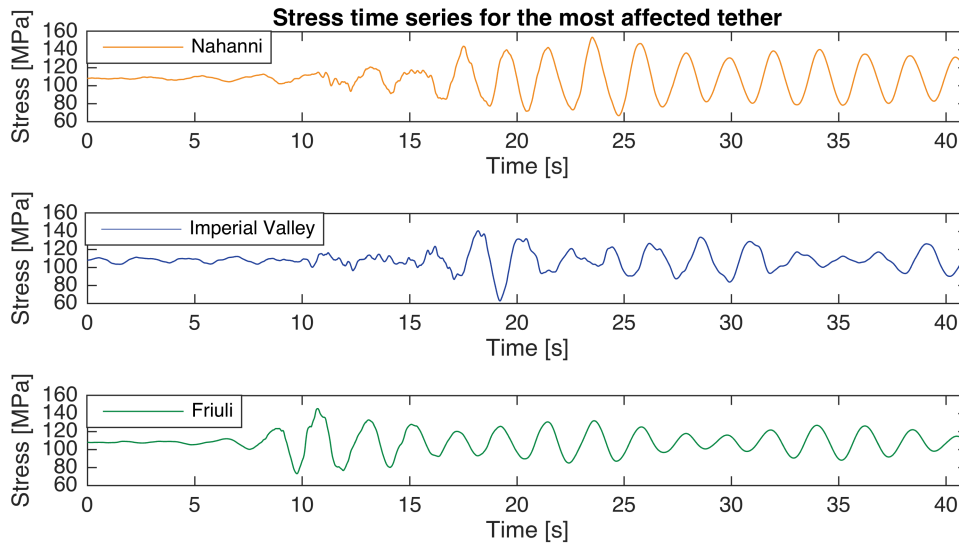


Figure 6.3-9: Response time series for the stresses in the shortest tether during the three different accelerograms used.

From the resulting time-series of the stresses in the shortest tether, it can be seen that Nahanni excites this tether with large amplitude for several oscillations, while Imperial Valley show a single low peak value with following amplitudes being quite low in comparison to Nahanni.

At the time instant when the dynamic stresses in the shortest tether are at a maximum for the three earthquake acceleration time series, their respective instantaneous displacement patterns along the bridge are shown in Figure 6.3-10.

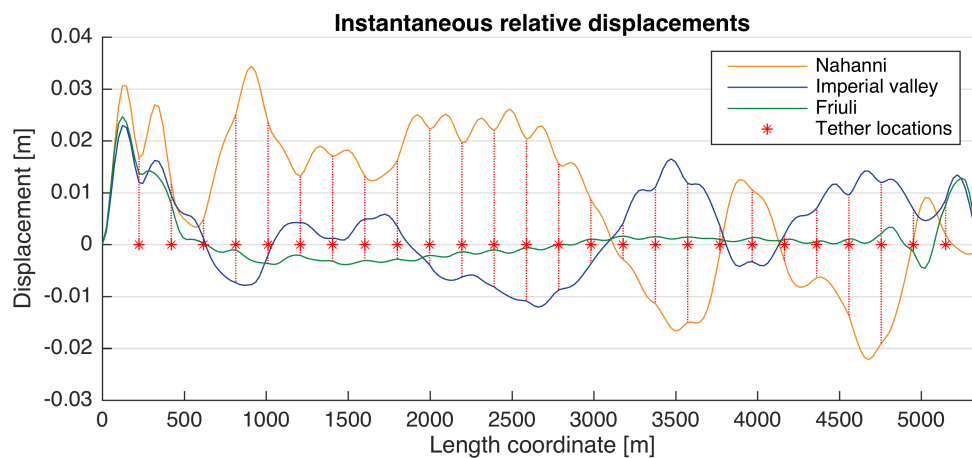


Figure 6.3-10: The instantaneous displacement pattern along the bridge at the time of maximal stress in the shortest tether for the three different earthquake accelerograms. Note that the time when this occurs is different for the three earthquake time series.

To find the frequency content of the oscillations in the shortest tether, a FFT is applied in Matlab on the stress deviation from the pretension after excitation from the Nahanni acceleration time series. The resulting one-sided frequency amplitude plot is shown in Figure 6.3-11.

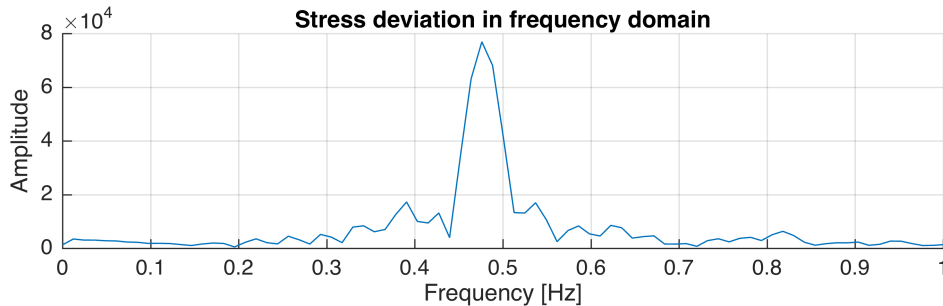


Figure 6.3-11: Stress deviation in the shortest tether shown in frequency domain for the oscillations in the SFT after the earthquake excitation. The SFT has been excited from the Nahanni accelerogram. Note that the peak at 0.47 Hz corresponds well with vertical mode 29, and the slight peak below 0.4 Hz correspond to mode 27.

The stress oscillations in the frequency domain show a significant peak at 0.47 Hz which corresponds well with vertical mode 28, and a peak slightly below 0.4 Hz that corresponds to the frequency of mode 26, both shown in Figure 6.2-5. Not that since this is the frequency content both during the earthquake and a short time interval afterwards, it includes response to forced vibrations, which explain why the peaks of the eigenmodes are not very sharp, however they clearly stand out. The instantaneous displacement pattern at the left end for all excitations shown in Figure 6.3-10 also correspond well with a combination of these two modes, which indicates that excitation of these modes are to a large extent responsible for the peak stress deviations in the shortest tether.

6.4 Sensitivity study

To limit the extent of the following sensitivity evaluations, only the Nahanni acceleration time series is applied to the beam model. This earthquake has been shown in Figure 6.3-4 to give high peak responses in the shortest tether of the modelled SFT.

6.4.1 Effect of Damping

Hydrodynamic damping

As the drag force is quadratic dependent on velocity, the damping matrix is linearly dependent on velocity. A summary of the drag damping properties originating from chapter 4.2 are given in Table 6.4-1, while a plot of the force-velocity relation per meter SFT length is given in Figure 6.4-1. Correlating these numbers with the velocities from the spatial seismic response analysis results in Figure 6.3-2 with a maximum velocity of about 0.1 m/s, resulting in a peak drag force of about 180 N/m length of the SFT. This load is negligible when compared to the uncertainties in the FE model the seismic excitation, and is therefore neglected for the study of the seismic response of the SFT. The frequency range of the response from the SFT from seismic ground motion is expected to be in frequency range of its eigenfrequencies. This corresponds to periods smaller than 5 s, or frequencies larger than 0.2 Hz. The radiation damping calculated in chapter 4.2 is significantly lower than the drag damping in this frequency range. The radiation damping is therefore also neglected in studying vertical seismic excitations.

Table 6.4-1: Drag damping properties.

Drag force per meter SFT and squared velocity	18090 Ns ² /m ³
Beam element length	24.625 m

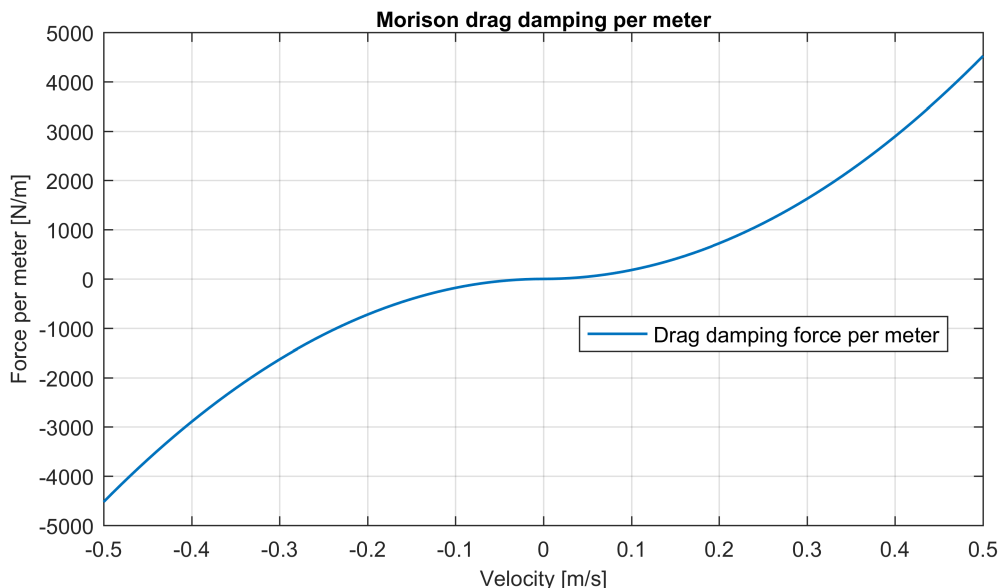


Figure 6.4-1: Plot of Morison drag damping force per meter SFT length and relative velocity.

Structural damping

For the initial response modelling, structural Rayleigh damping was applied at 0.8 % according to the description in Figure 6.2-6. A structural damping coefficient of 0.8 % may be somewhat high for uncracked concrete and a value of 0.5 % is also often used. To investigate the sensitivity of the seismic response with respect to the applied damping ratio, the beam model is excited from seismic ground motion with different values for structural damping. The resulting plot of peak stresses in the tethers for the different values of applied structural damping is shown in Figure 6.4-2.

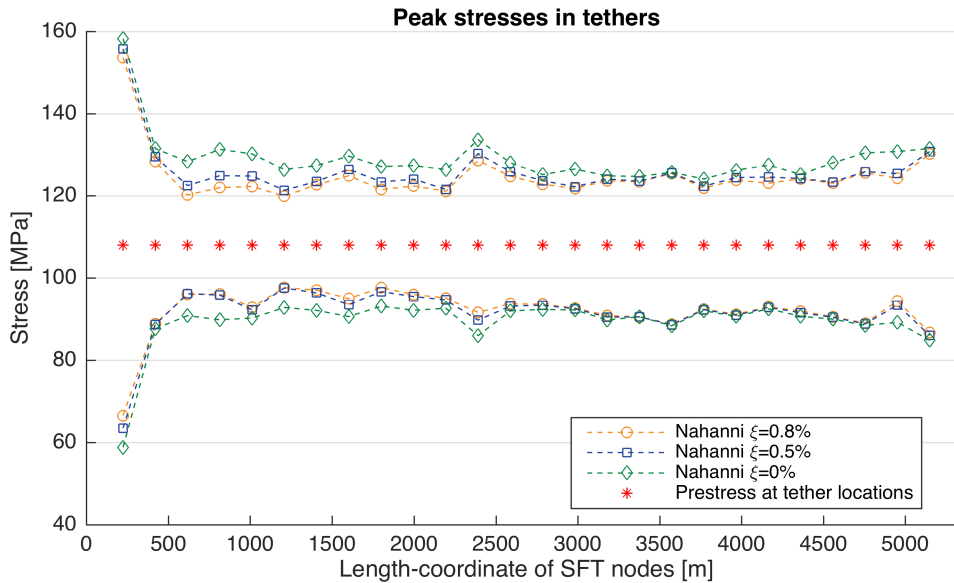


Figure 6.4-2: Peak stresses in the tethers along the bridge for different values of critical damping ratios.

The results show that for the lowest stress value in the shortest tether, changing the structural damping ratio alters the tether response. Applying zero critical damping led to roughly 20 % higher deviation from the applied prestress for the most affected tether compared to the initial model, while 0.5 % critical damping led to a deviation increase of about 7 %. The effect of structural damping on the calculated seismic response in general seems to be modest.

6.4.2 Torsional effects

For the initial model the torsion resistance from both the beam and the tether force pairs was smeared over the SFT length. The contribution of the tether force pairs was estimated using the stiffness of an average tether length. To investigate the torsional effects, a more realistic representation of the torsional resistance is developed. This model includes applying pointwise torsional springs equivalent to the torsional resistance of the force pairs at the tethers. The beam elements are applied the equivalent torsional resistance excluding contribution from the tether force pairs according to chapter 6.1.3. The peak torsional stresses over the bridge length are shown in Figure 6.4-3 for both the initial model and for the more realistic torsional representation including torsional springs.

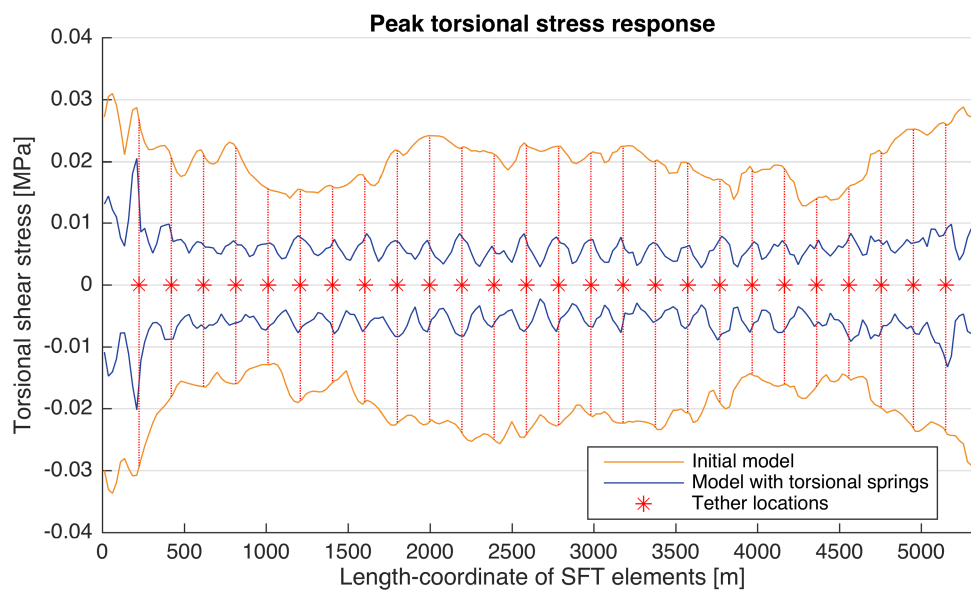


Figure 6.4-3: Peak torsional shear stress response in the bridge girder for the initial model, and for the model with refined torsional representation with torsional springs.

The peak torsional stresses calculated for the beam seems reasonable, with maximums at the rotational springs at the tethers and at the fixed ends. The torsional stresses are even lower for a more correct representation of the torsional resistance, which substantiate that these stresses may be disregarded for vertical earthquake response.

The maximum rotation spring moment throughout the analysis is only 2.3 MNm, corresponding to a tether stress of 0.15 MPa when the tethers act as force pairs. This is equivalent to 0.3 % of the peak stress oscillations in most affected the tethers from seismic excitation of the initial model, shown in Figure 6.3-4, and can therefore safely be neglected.

The peak stress response in the shortest tether is virtually identical for the initial model and the model with pointwise rotational springs. The first difference occurring after 4th significant digit in the tether stress, a deviation of 0.002 MPa. It indicates that any coupling between torsion representation and tether stresses are negligible.

6.4.3 Earthquake wave passage effect

A brief analysis of the SFT response to simplified asynchronous excitation is conducted on the initial beam model without seaquake loading. Only the wave passage effect is considered. Two analyses are performed with excitation from the Nahanni acceleration time series, one with a south-north (SN) propagating wave and one with a north-south (NS) propagating wave. The seismic wave speed is set to 1500 m/s. The resulting peak stresses are shown in Figure 6.4-4.

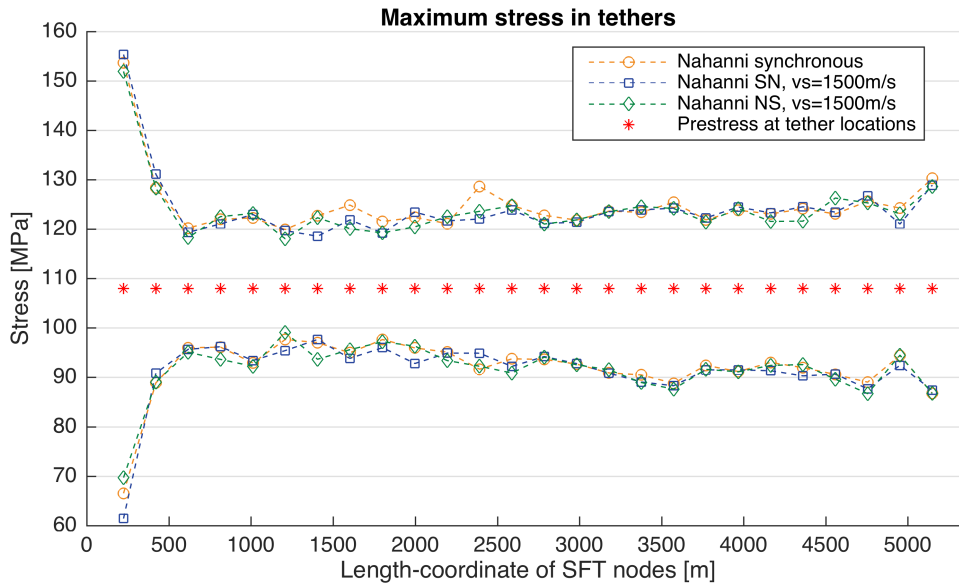


Figure 6.4-4: Peak stress response of the SFT excited from the Nahanni excitation considering wave passage effect in two directions.

The effect on tether stresses in general seem to be modest to small. However, note that the lowest stress value observed for a SN propagating wave corresponds to 5 % higher deviation from the prestress than the results for synchronous ground motion.

6.4.4 Effect of softer tethers.

It is evident from the initial results that the stiffest tethers close to the south shore attract the largest stress oscillations from seismic excitation. To investigate the effects of changing the effective elastic stiffness of the tethers, the beam model is modified by changing the stiffness of the two tethers closest to the south shore. In the numerical modelling this is accomplished by changing the modulus of elasticity of these tethers to 70 GPa, as opposed to the initial 210 GPa. This significantly reduced the axial stiffness of these two tethers. The tether stiffness for both the original model and the model with refined stiffness is shown in Figure 6.4-5.

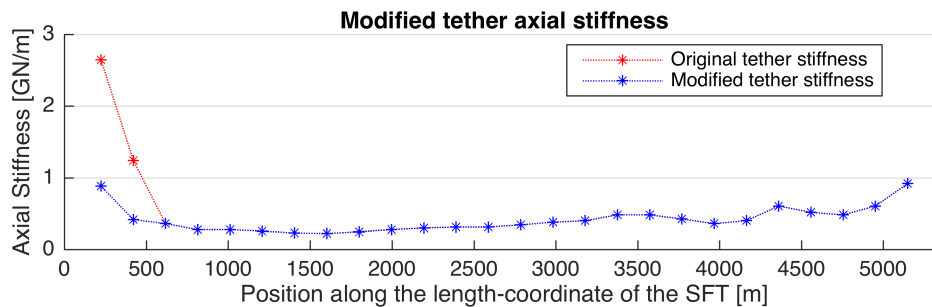


Figure 6.4-5: Tether stiffness for the initial beam model along with the modified stiffness for the tethers after softening the two tethers at the left shore.

The model with modified tether stiffness is then excited with the Nahanni accelerogram. The resulting peak stresses in the tethers are shown in Figure 6.4-6 together with response from the initial beam model.

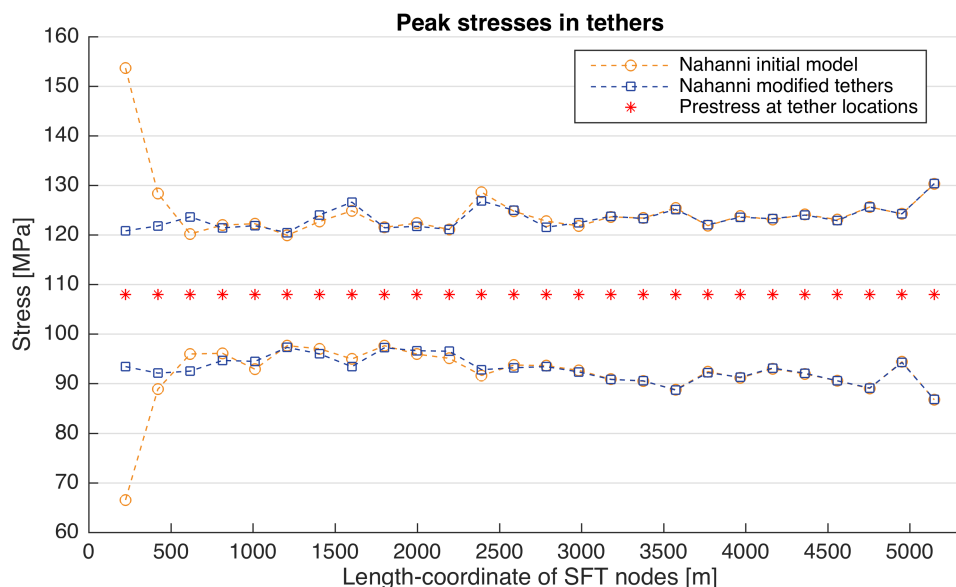


Figure 6.4-6: Peak stresses in the tethers along the SFT length. The results from the initial model is shown in yellow, while the results from the modified model with soft tethers at the left is shown in blue.

The results in Figure 6.4-6 show that lowering the stiffness in the two shortest tethers on the left shore drastically decrease the deviation from the prestress in these tethers. The effect seems to be highly local, as the stress values for the tethers at the right end of the bridge are practically unaffected.

6.5 Applying seaquake

The load a structure experiences from a seaquake is dependent on the structural properties, and should ideally be evaluated in a coupled analysis.

There are in principle two possibilities of using a coupled approach for the seaquake loading. The first is a full coupled analysis with both response and load modelling in a finite element model with acoustic mesh surrounding the SFT. This would automatically account for the hydrodynamic properties of the submerged structure through the acoustic-structural mesh coupling. The second method being somewhat simpler and would include a coupled analysis accounting for the interaction between the seaquake pressure waves and the SFT assumed as rigid for calculating seaquake loading. This load would then be applied to an uncoupled response analysis of the SFT in for instance a beam model. In this case the hydrodynamic properties of the SFT need to be included in the response modelling, for instance through added mass as done for the initial response modelling.

For this thesis however, a decoupled approach of estimating the seaquake effect on the SFT is evaluated. The seaquake loading is calculated from the pressure difference between the top and bottom of the SFT depths in an analytical and numerical model. Neither of these load models account for the presence of the SFT, thus being a simplification ignoring interaction between the pressure waves in the water and the SFT geometry. The hydrodynamic properties of the submerged structure is accounted for through the added mass representation in the simplified beam model used for response calculation. Although this represent a decoupled approach to the seaquake loading, it is expected to give a reasonable approximation of the magnitude of the seaquake effect.

The seaquake loading is dependent on water depth, and to reduce the amount of seaquake time-series needed, the seabed topography is idealized at depth intervals of 50 m. The depths are idealized as constant between the middle point between tethers, as shown in Figure 6.5-1. Seaquake loading is applied as distributed line loads on the beam elements according to their respective idealized seabed topography. The seaquake loading is thus applied to the 2D beam model by means of several 1D seaquake loads generating a quasi-2D load model.

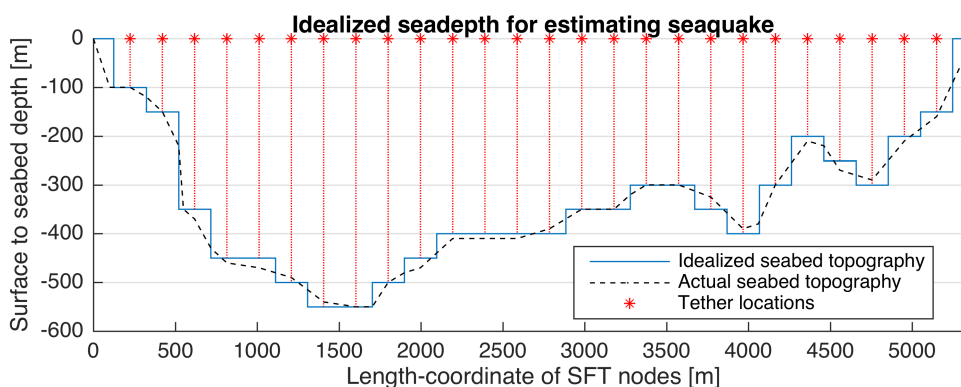


Figure 6.5-1: Idealized seabed topography shown with blue line, together with the actual seabed topography in a dashed black line. Note that the beam elements closest to the shore are not applied seaquake loading, and the idealized seabed topography is therefore represented with zero depth in these regions.

6.5.1 Analytical seaquake from frequency domain

Using Matlab, the displacements corresponding to the earthquake acceleration time series are derived through numerical trapezoidal double integration. A FFT algorithm with zeropadding in Matlab is used to transform the displacement time-series to the frequency domain. Using the amplification functions in the frequency domain for the different depths as derived in Figure 6.5-1, the relative fluid particle displacement of the depths corresponding to the submerged depth of the top and bottom of the SFT, at approximately 30 m and 42 m, are attained in frequency domain. The relative fluid displacements between these points are then calculated through an IFFT algorithm. This procedure is done for the 10 different depth intervals of the idealized seabed topography. By numerical differentiation, the relative fluid particle velocities between top and bottom of the SFT originating from the pressure waves are attained.

The net line loads on the SFT are finally calculated by converting velocity to pressure through the impedance properties of water, and multiplying with the projected width of the two pipes of the SFT. In principle, this is equivalent to a simplification of the pressures of the top and bottom of the SFT both acting on a horizontally plane surface, equivalent to the SFT cross section being a rectangular box, disregarding any interaction effects between the SFT and the pressure waves. For illustration, the attained pressure-time series for a seabed depth of 100 m using the Friuli time-series is shown in Figure 6.5-2. All the pressure time series calculated are given in the appendix.

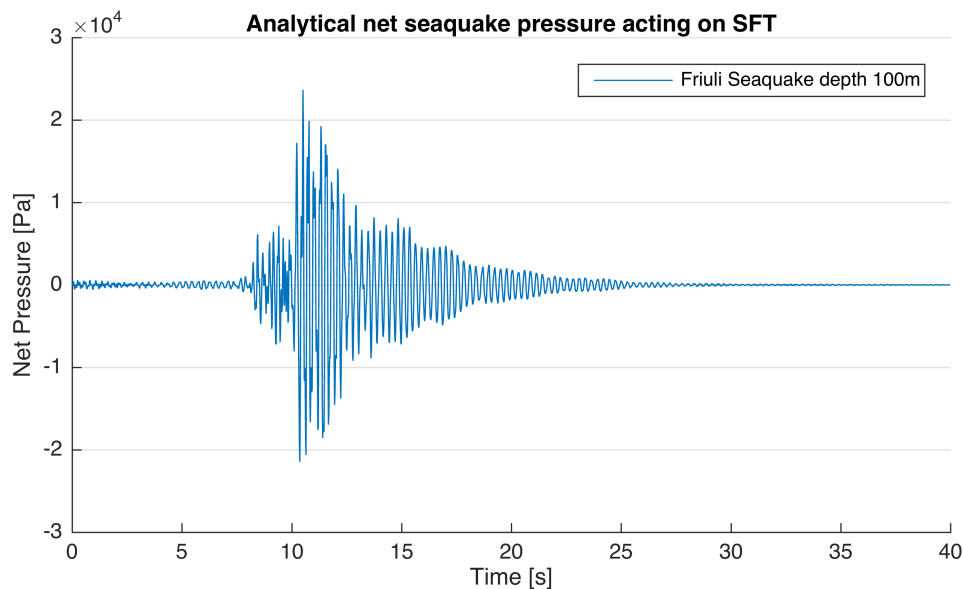


Figure 6.5-2: Calculated net pressure time series for seaquake loading with 100m seadepth. The pressure is derived from the relative velocity between depths corresponding to the top and bottom of the SFT.

The results show that the calculated seaquake show similarities to the Friuli acceleration series applied, with relatively short duration, and onset of the highest pressures starts at the same time incident. The pressure oscillates with more harmonic tendencies than the acceleration series, which is due to the pressure waves in the water being reflected up and down the water column at a frequency corresponding to the water depth due to constant wave speed. The calculated seaquake maximum net pressure value from the 100 m depth and Friuli acceleration series is roughly 25 kPa, which corresponds to a line-load on the SFT of roughly 600 kN/m.

To compare the results of seaquake pressures calculated with different depths, both the 100 m and 550 m seabed depth pressure time-series for Friuli are shown at a short time interval early in the time series in Figure 6.5-3.

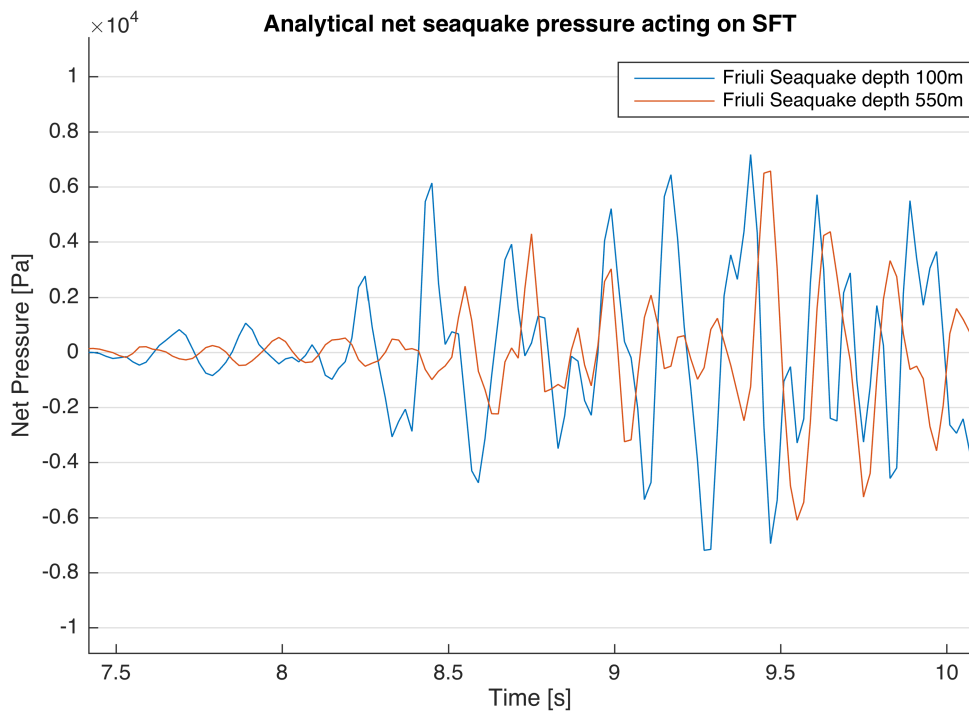


Figure 6.5-3 Calculated net seaquake pressure on the SFT from 100 m and 550 m seabed depth. Pressure series only shown excerpt of the time series.

The results in Figure 6.5-3 show that the time-lag between the two first peaks over 2000 Pa for the two pressure time series is approximately 0.3 s, corresponding to a wave propagation of roughly 450 m in water. This suggests that the analytical frequency domain solution behaves reasonable accounting for the correct phase-lag due to the propagation of the pressures waves in water. The calculated seaquake pressures deviate more in shape at later time incidents in the time series due to the different eigenfrequencies at the two depths affecting the response.

6.5.2 Abaqus Acoustic time-domain pressure loading

By using the same idealizations of seabed topography as for the analytical frequency domain solution, an acoustic time domain analysis is performed using the model derived in chapter 5, with loading based on the shortened Friuli time series in chapter 3.2.1. The net seaquake loading is calculated analogly to the solution from frequency domain, through extracting the difference between the pressure time-series at depths corresponding to SFT top and bottom, and multiplying with the projected cross section of the two pipes. In total 10 different acoustic models are run with water depths corresponding to the idealized seabed topography in Figure 6.5-1. For illustration, the net pressure derived from the ABAQUS results in time domain with a column model height of 100 m, 250 m and 550 m is shown along with their corresponding frequency domain solutions in Figure 6.5-4. All the calculated ABAQUS acoustic seaquake pressures time series are given in the appendix.

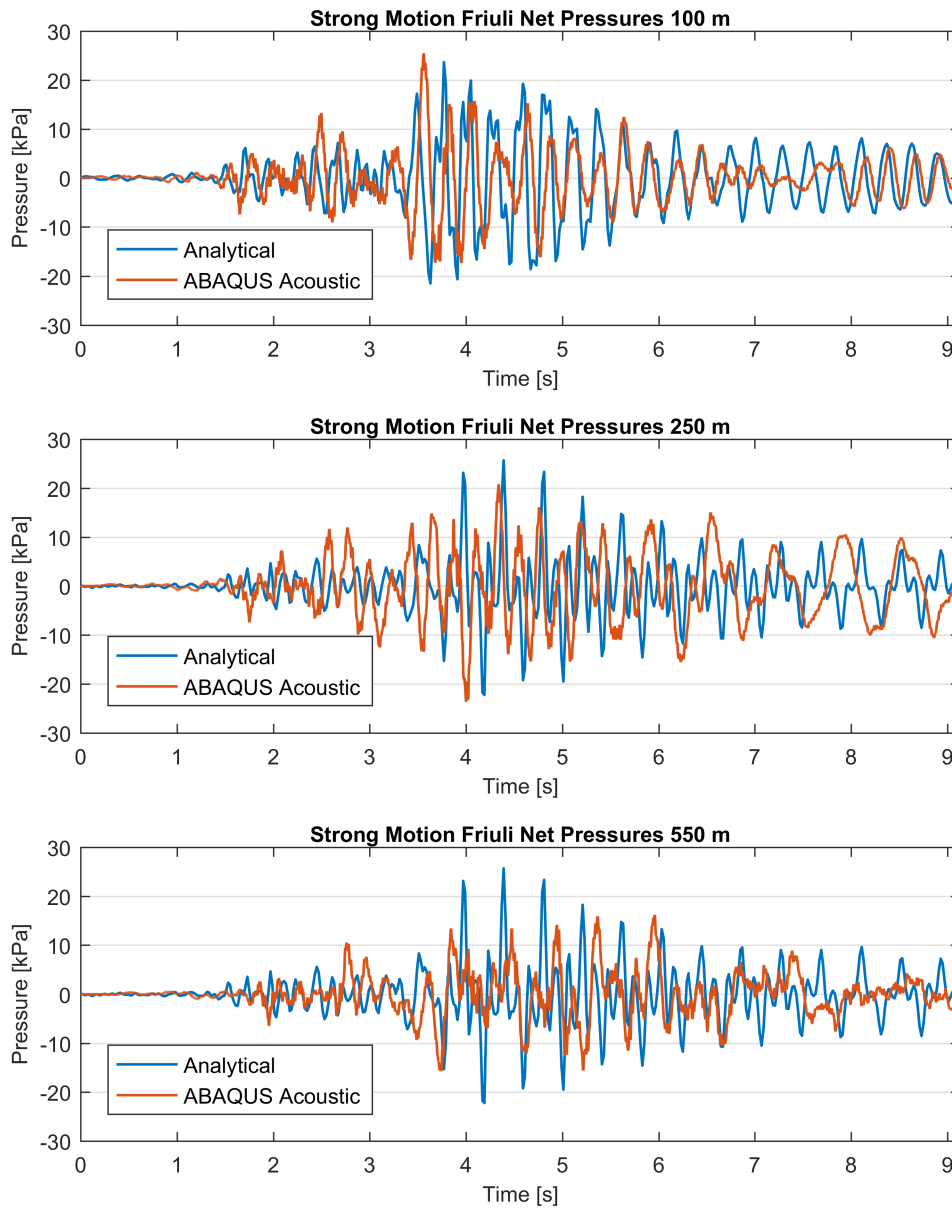


Figure 6.5-4: Net pressure time series calculated from the shortened Friuli time series in chapter 3.2.1. The results from the Abaqus acoustic time domain analysis is denoted ABAQUS Acoustic in the legend, and the analytical frequency domain solution is denoted Analytical.

The figures indicate comparable results even though they are based on different solutions. The maximum peak values and frequency content of the solution are fairly similar, which supports use of the ABAQUS acoustic column modelling for use in more refined models of structure-acoustic interaction for the SFT.

6.5.3 Global response of seaquake strong motion Friuli time series

An analysis on the beam model of the SFT is run for the strong motion part of the Friuli acceleration time series, to compare the effect of the seaquake calculated analytically in frequency domain with the seaquake calculated from ABAQUS in time domain. Note that the seaquake loading has only been calculated for the shortened acceleration time series for Friuli in chapter 3.2.1, due to large computational time required for the ABAQUS acoustic model. The peak tether stress of the SFT to the different seaquake loading for the shortened of Friuli time-series on the SFT beam model is shown in Figure 6.5-5.

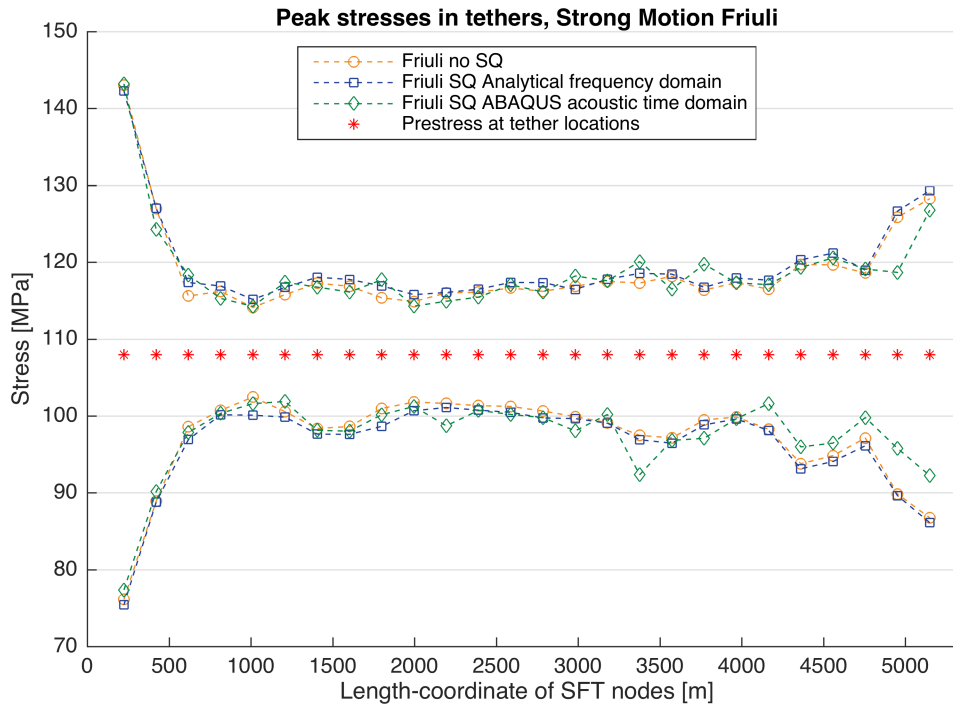


Figure 6.5-5: Peak stress in tether for Friuli strong motion time series without seaquake and including seaquake from analytical and numerical models.

The figure shows that the peak tether stresses of the SFT to the strong motion part of the Friuli time series is very similar for the seaquake representation from analytical frequency domain seaquake and the acoustic finite element results. The peak stresses also seem not to be affected by the seaquake to a great extent. Note that the duration of the analyses are only 9.1 s.

The peak stresses in the tethers are only slightly affected by the seaquake loading, however this may not be the case for accelerations. The peak value for the pressures is in the magnitude of 25 kPa, corresponding to a line-load of roughly 600 kN/m, compared to the oscillating mass of the structure including added mass of roughly 600 000 kg/m. According to Newtons second law of motion, this would result in a peak acceleration from the seaquake loading alone of about 1 m/s^2 . The peak accelerations along the SFT are extracted from the response analysis and are shown in Figure 6.5-6 for the different representations of seaquake during Friuli strong motion excitation.

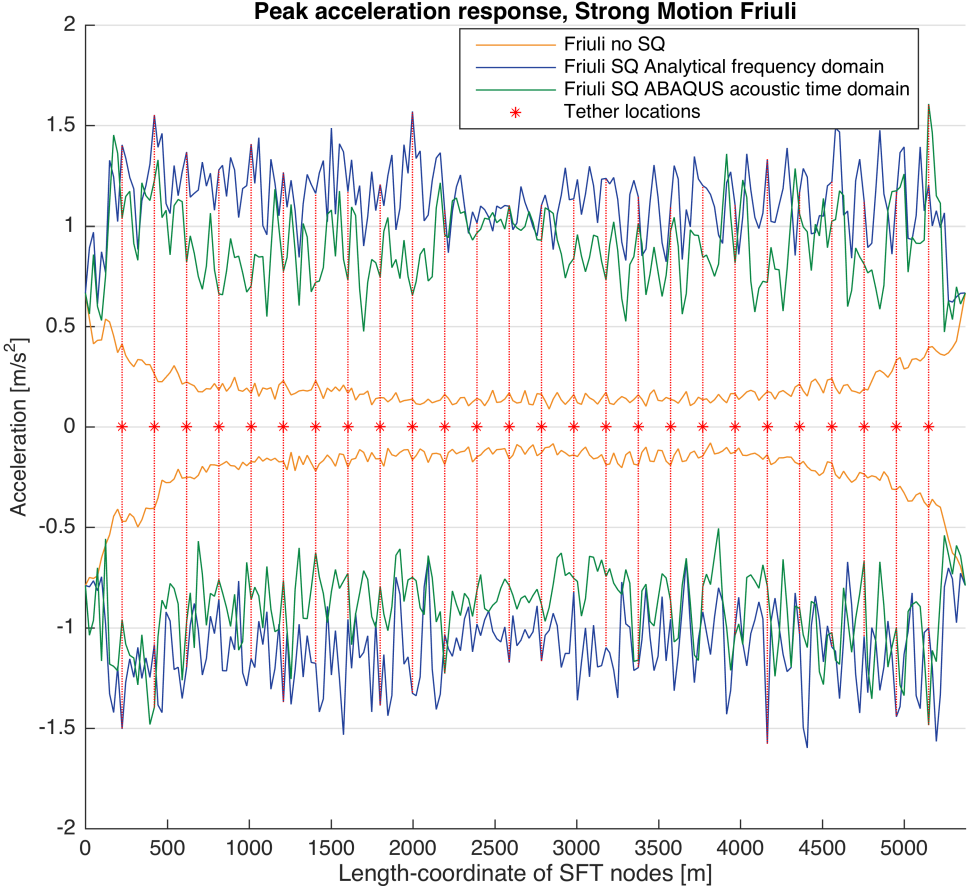


Figure 6.5-6: Acceleration of strong motion Friuli time series along the SFT bridge elements without seaquake and including seaquake from analytical and numerical models.

The results for peak accelerations in Figure 6.5-6 show that when including seaquake loading either from frequency domain or ABAQUS acoustic, the accelerations are amplified compared to the ground motion almost over the entire SFT length. This is in large contrast with the de-amplification of the accelerations along the bridge when no seaquake is applied.

6.5.4 Global response of full length seaquake loading

The effect of seaquake loading on for the full length of the three acceleration time series are studied. Due to computational time for the ABAQUS acoustic seaquake model this is only done for the seaquake load calculated from the frequency domain. The peak stress response in the tethers when applied seaquake loading for all three earthquake acceleration time series together with response from excitation without seaquake loading is shown in Figure 6.5-7. The computed peak acceleration for the same analysis is shown in Figure 6.5-8.

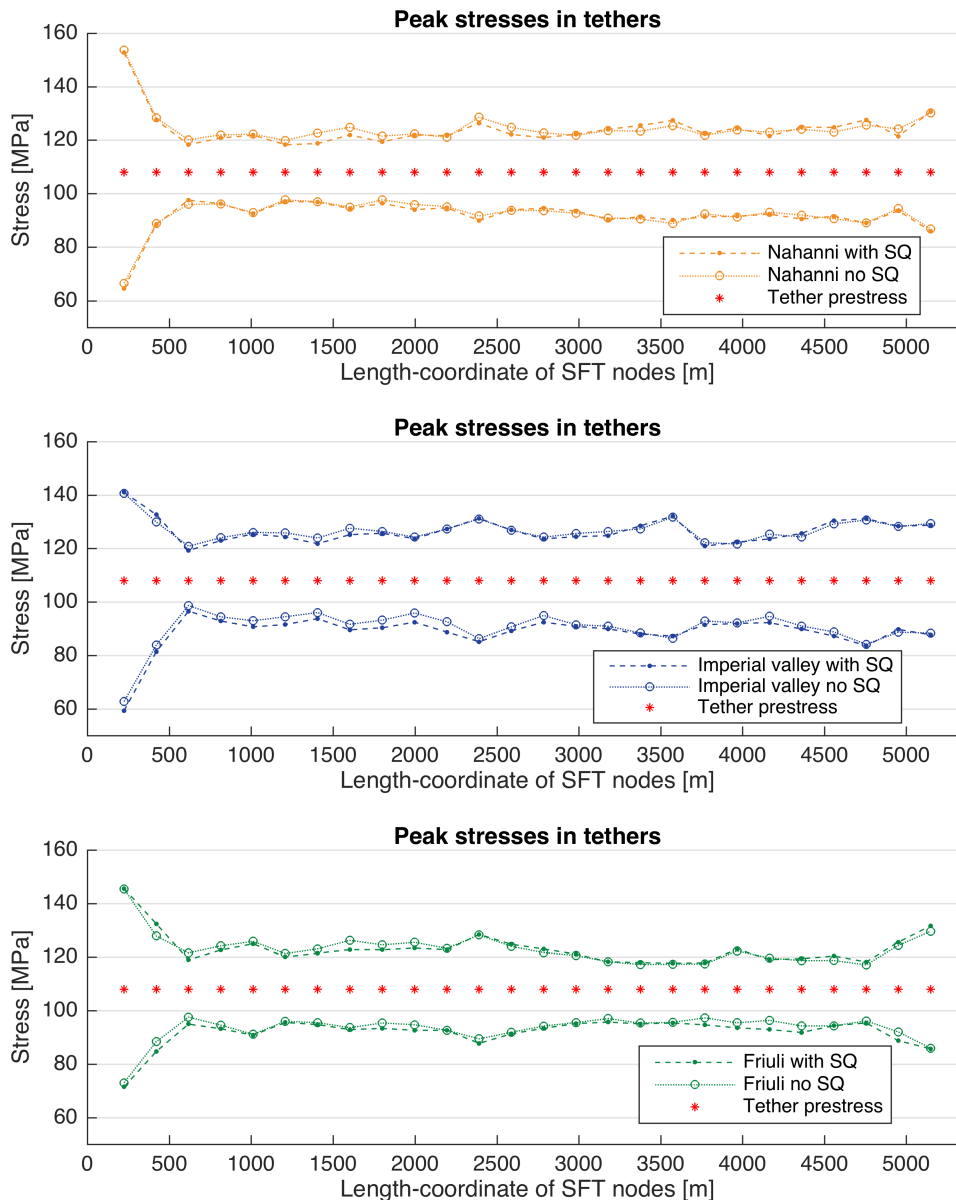


Figure 6.5-7: Peak stresses in the top tether elements along the SFT length nodes for the three different earthquake series with analytical solution of seaquake compared to the initial results.

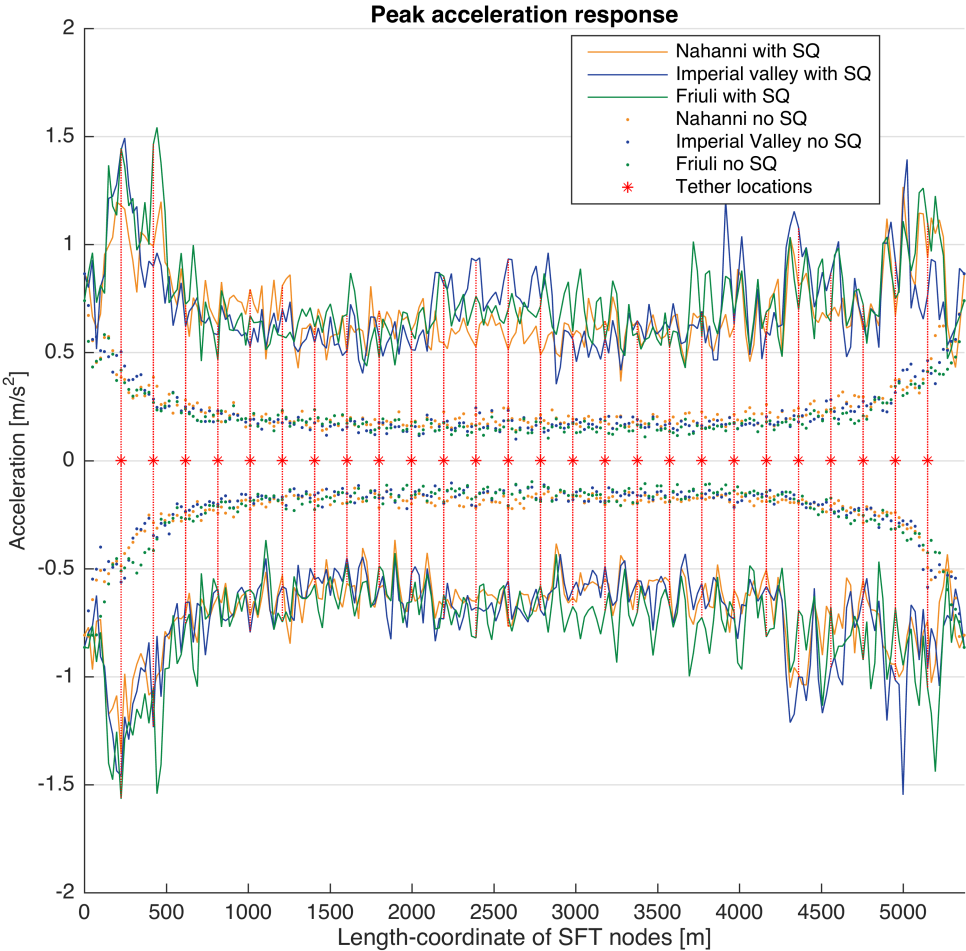


Figure 6.5-8: Peak node acceleration along the SFT bridge nodes for the three different earthquake series with and without analytical seaquake loading.

The results in Figure 6.5-7 show that including the seaquake loading has modest to small effect on the computed stresses in the tethers. However, Figure 6.5-8 show that the accelerations are significantly increased along the SFT length when including seaquake loading.

6.5.5 Earthquake with higher return period

An attempt is made to evaluate the effect of a larger earthquake excitation, using the earthquake time series normalized to the PGA of an earthquake with 10 000-year return period at Bjørnafjorden. The critical damping ratio is reduced to 0.5 % for structural damping in the concrete. The seaquake loading derived from the frequency domain is applied. The resulting tension in the tethers are shown in Figure 6.5-9. For the purpose of comparison, possible effects from the wave passage effect are not included in this analysis.

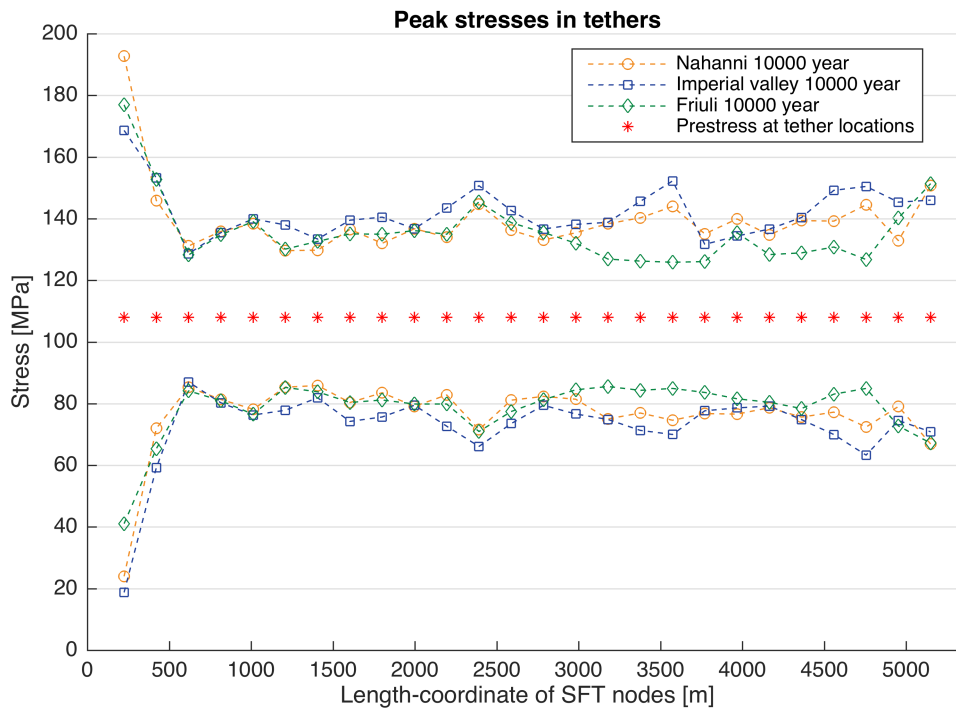


Figure 6.5-9: Peak stresses in the top tether elements along the SFT length nodes for all three time series, normalized to the PGA values of the earthquakes with return period of and 10 000 years and critical damping ratio of 0.5 %. Analysis includes seaquake loading derived from frequency domain.

The analysis show that no tethers have negative peak stresses, and they are thus constantly in tension, which is required for the system to remain in the linear regime. The lowest tension value in the most affected tether is slightly below 20 MPa, and the highest slightly below 200 MPa. The computed peak acceleration for the same analysis is shown in Figure 6.5-10.

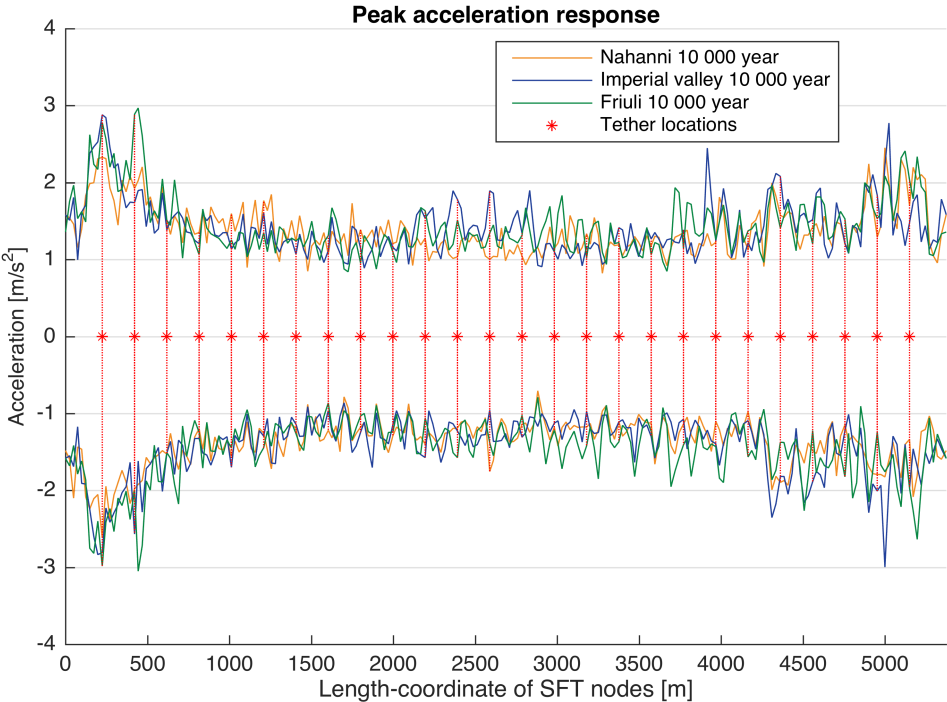


Figure 6.5-10: Peak node acceleration along the SFT bridge nodes for the three different earthquake series with and without analytical seaquake loading of 10 000-year return period.

The accelerations are significantly increased along the SFT length when including seaquake loading, having peak values up to 3 m/s². These values are close to being double compared to the values from the response with 475-year return period including seaquake given in Figure 6.5-8, which is in accordance with the relation between the PGA of the earthquakes.

7 Discussion

7.1 Hydrodynamic properties of SFT

7.1.1 Added mass

Through running a panel model in WADAM, frequency dependent added mass and hydrodynamic radiation damping were calculated for a frequency range below 0.32 Hz, as given in chapter 4.2. The frequency range for the calculated eigenmodes in chapter 6.2.1 exceed this limiting frequency. Ideally, the WADAM model should be analyzed with smaller panel size to give accurate values for higher frequencies, however, due to limitations in the software available, this was not possible. Nevertheless, comparing the numerical results with literature, some assumptions of the results for higher frequencies can be made. By comparing the shape of the attained frequency dependent added mass shown in Figure 4.2-2 with results in literature shown in Figure 1.4-2, it is evident the calculated values for added mass of the SFT share a similar shape. It is thus reasonable to extrapolate the attained added mass coefficient for higher frequencies. This is due to the nature of the added mass coefficient to go towards a constant value for high frequencies, and the shape of the calculated added mass coefficient already seems to be fairly constant between 0.2 Hz and 0.32 Hz. A vertical added mass coefficient of 1.1 for the entire range of wet eigenfrequencies for the SFT is therefore a reasonable approximation.

For a circular cross section in infinite water domain, the added mass coefficient is expected to be 1; that is, the added mass is equal to the displaced water mass. However, the modelled SFT structure has a more complicated nature; firstly, it is not a perfect circle, secondly it is not in infinite fluid, and thirdly, it consists of cross-beams and two pipes which may cause interaction effects. These factors complicate the system, making the performed numerical calculation desirable to ensure use of an adequately accurate added mass coefficient in the structural analysis. Furthermore, the proximity to the free surface may explain a great deal of the deviation in added mass between the ideal circular cross section solution in infinite fluid domain, and the numerical analysis results for the SFT. The structure is roughly 6 radii below the fluid surface, and for an ideal circular cross section, this will give a theoretical added mass value close to 1.1, in accordance with Figure 2.3-2. This indicates that the distance from the fluid surface may be of more importance to the added mass in vertical direction than the geometry interaction effects of the SFT.

In the horizontal direction, however, the limit towards high frequencies for the calculated added mass coefficient is at roughly 0.82 as shown in Figure 4.2-2. As the two pipes align in the oscillatory direction, it is reasonable that the interaction effects of the two pipes and cross beam should be larger than for the vertical case. The cross-beam connectors increase the volume of the structure without significantly increasing the added mass in horizontal direction, which is a contributing factor for the reduction in the added mass coefficient. However, this is a complicated matter, as several parameters influence the added mass, such as depth below surface level which should give a slight increase in added mass as previously mentioned.

7.1.2 Hydrodynamic damping

Hydrodynamic radiation damping and drag damping were estimated using WADAM. According to the results in chapter 4.2, the drag damping at velocities of 0.1 m/s corresponds to a distributed load of only 180 N/m along the SFT length. This is the peak value drag force for maximum velocities from earthquake excitations of the initial beam model. The drag damping model is based on Morison equation, which is an empirical approximation. Neglecting drag damping is expected to give conservative results for the response studied in this thesis. The radiation damping calculated is very similar in shape to the results in literature in Figure 1.4-1. It is also expected that radiation damping should go from zero at low frequencies and back to zero at high frequencies, as mentioned in chapter 2.3.2. Extrapolating the values for radiation damping in the range of eigenfrequencies of the SFT is thus reasonable. The corresponding distributed load for radiation damping is even lower than the drag damping. It is also worth noting that it is desirable for the vertical eigenfrequencies of the SFT to not lie in the frequency region of peak values of radiation damping. This is to avoid resonant behavior with surface wave loads, since incident surface waves will generate vertical loading on the SFT at the frequencies for peak radiation damping.

The relative velocity for the SFT from seismic excitation has such a low value that any drag and radiation damping should be neglected due to much higher uncertainties in the finite element response modelling, especially in the load representation of a seismic event. The drag and radiation damping force may of course be worth considering for other load cases with higher relative velocities between the fluid and the SFT.

7.2 Eigenmodes

The eigenmode analysis show highly local vertical eigenmodes. The tethers are in principle elastic supports, and their axial stiffness steer the behavior of the bridge.

The first vertical eigenmodes appear in the area with the deepest water thus softest tethers, as shown for the three first modes in Figure 6.2-4. These local modes have similarities to those of a simply supported beam with the first mode being similar to a sinusoidal half-wave, the second a full wave, the third one and a half wave, etc. Correspondingly, the second and fourth vertical mode has very low effective mass in the vertical direction, while the first and third modes have significant effective masses. Note that eigenmodes with low or zero effective mass may be excited by asynchronous ground motion.

At the south (left) end of the bridge, some local vertical eigenmodes with high eigenfrequency and significant masses are found. In these mode shapes the two tethers closest to the south end of the bridge oscillate vertically, while the other tethers are almost unaffected from these modes, as can be seen in the mode shape for these modes as shown in Figure 6.2-5. As these tethers are short and therefore have large axial stiffness, excitation of these eigenmodes are expected to induce large stress oscillations in these tethers.

The significant vertical effective masses are distributed over a few vertical modes, with 97 % located between 0.2-0.5 Hz in the first 28 vertical modes, indicating that vertical structural response from excitation will to a large extend occur in this frequency range.

When updating the added mass coefficient from 1.0 to 1.1, all vertical eigenfrequencies are reduced by a factor of roughly 2.5%. This is reasonable since the mass of the system is dominated by the mass of the beam relative to the mass of the tethers. As a result, the ratio of change in the eigenfrequencies due to the changed the added mass are expected to be similar between the eigenmodes. This is due to the added mass is applied by scaling the inertia of the beam with a constant value.

The vertical eigenmodes of the 2D model are almost identical to those of the 3D model. However, the 3D model also gives horizontal modes as well as torsional modes, which a 2D model is unable to represent. If only vertical excitation alone is of interest, and the curvature effects such as torsion are disregarded, this indicate that a 2D analysis may be sufficient for simplified vertical seismic response analysis of a SFT with vertically straight tethers.

7.3 Seismic response of global beam model

In general, the SFT amplifies the peak displacements compared to the ground motion, as shown in Figure 6.3-1. The tethers oppose relative displacements with the seabed, and therefore restrain the displacements. As expected, this effect can be seen in the figure since the peak displacements often show local minimums at or close to the tether locations, and local maximums between the tethers. The largest displacements occur at the deepest tethers, however the peak velocities along the bridge given in Figure 6.3-2 are of similar magnitude, indicating that the modes responsible for these displacements are of lower frequencies than those at the position of shorter tethers, as they have similar peak velocities but larger displacement amplitude to travel per oscillation. This is in accordance with the frequencies and shapes of the eigenmodes of the SFT calculated in chapter 6.2.1. The velocities and displacements per se does not cause problems for the SFT, however large relative displacements between the SFT and the seabed will give rise to tether stresses that may be critical.

The peak accelerations for the initial model without seaquake are de-amplified all along the bridge, as can be seen from the results in Figure 6.3-3. The peak accelerations occur at the ends of the SFT, where they are fixed to the base. Due to the fixed boundary condition at the shore the SFT is accelerated more from the ground motions than in the middle span. The reason for the de-amplification of the acceleration of the SFT, is because of the high inertia of the bridge, and the tethers acting as soft elastic supports. This is due to the eigenfrequencies of the SFT between 0.2-0.5 Hz are not in the range of the dominant frequencies of the acceleration time series, as shown in Figure 3.2-2.

Stresses in the tethers varies a lot along the beam, with the two first tethers oscillating between high peak values. The peak values of the stresses in the shortest tether are roughly 46 MPa apart from the applied pretension of about 108 MPa. The Nahanni accelerogram gives the highest value of the peak tether stress, while imperial valley gives the lowest value. However, from the time series of the stresses shown in Figure 6.3-9, it is seen that Nahanni excites this tether significantly for several oscillations, while the imperial series gives a low peak value for the stresses for a single peak.

The response to shear forces for the SFT is closely related to the tension in the tethers. The transverse shear forces are converted to equivalent peak shear stresses in the centerline of the cross section through elastic beam theory, as shown in Figure 6.3-6. The resulting shear stresses are small with a maximum value of 0.6 MPa and will therefore be of minimal concern for this SFT from vertical seismic excitation. The corbels connecting the SFT to the tethers will of course need to be designed according to the expected forces to be transferred to the tethers.

Similarly, the bending moments were converted to peak bending stresses as shown in Figure 6.3-7. These behave as expected, with maximums at the fixed ends of the SFT, however the stresses are also in this case low when compared to the ultimate design stress for the chosen concrete at 31 MPa. The stresses may still be of some interest in order to limit cracking of the concrete to ensure the water tightness of the SFT in the aftermath of excitation from a seismic event. The maximum bending stresses from static buoyancy are roughly 4.5 MPa at the tethers, close to double the dynamic earthquake bending stress. In addition comes dynamic moment fluctuations from other loads not considered in this thesis.

The Fourier transform of the resulting tether stress in the shortest tether from the Nahanni earthquake as shown in Figure 6.3-9 show a distinct peak together with a less pronounced peak just below 0.4 Hz. The frequencies of these peaks correspond closely to the two eigenmodes on the left side of the SFT shown in Figure 6.3-11. Together with the instantaneous displacement pattern shown in Figure 6.3-10, which show similarities to a combination of these mode shapes for all three acceleration series, this indicates that these two modes are to a large extent responsible for the peak stresses in this tether.

7.4 Sensitivity study

7.4.1 Damping sensitivity

By exciting the SFT beam model with the Nahanni accelerogram it was found that the peak values of the stresses were to some extent affected by the applied damping. Any real concrete structure will have a finite value of damping, thus making an analysis with zero damping unrealistic. This study shows the limit to how much the damping may affect the peak response of the structure. The structural damping can be stated to affect the peak tether response moderately, with an increased deviation from prestress of 7 % when reducing structural damping from 0.8 % to 0.5 %. Correspondingly, the limit of the damping influence is shown to increase deviations from prestress with 20 % when structural damping is set to zero, when comparing to the results for structural damping of 0.8 %. This seems reasonable since transient analyses with irregular loads, such as earthquake loads, are generally much less affected by damping compared to periodic loading scenarios.

7.4.2 Torsional effects

The curvature of the SFT will result in torsional forces due to vertical motions. The results in Figure 6.3-8 show that shear stresses from torsional moment do not appear to be of importance for structural response from vertical earthquakes. This is due to the two pipes acting as closed sections that give rise to small torsional shear stresses, and that the torsional moment excitation from vertical earthquakes are small.

When representing the torsional resistance of the beam model through pointwise rotational stiffness over the tethers, the maximum torsional shear stresses in the beam are reduced as is shown in Figure 6.4-3. The torsional stresses have local maximums over the tethers as expected since the tethers give large resistance against torsional rotations. The shear stresses from torsion are vanishingly small for both models, and may safely be neglected in the case of vertical seismic excitation.

The force-pairs in the tethers opposing torsional moments will give rise to additional tether stresses. However, the results in chapter 6.4.2 show that the increase in tether stresses is only 0.15 MPa due to the rotational stiffness in the tethers, which is a 0.3 % increase in the deviation from prestress. The results also show that the response in tether stresses from a smeared torsional model and a model with pointwise rotational springs over the tether are virtually identical. Both these effects are reasonable to neglect. The torsional representation therefore seems to not be of importance when considering vertical seismic excitations, and an approximated smeared torsional resistance is adequate.

7.4.3 Earthquake wave passage effect

The results from the simplified representation of the wave passage effect on the Nahanni excitation gives alterations of the response in the shortest tether. The lowest peak stress value decreases roughly 5 % when excited with a wave propagating in SN direction, and increases roughly 5 % when excited with a wave propagating in NS direction when compared to the results from synchronous ground motion. This suggests that effects of asynchronous seismic excitation may affect the SFT response to some extent.

7.4.4 Effect of softer tethers

When reducing the stiffness of the two shortest tethers at the south end of the bridge, the stress oscillations in these tethers were reduced drastically when excited by the Nahanni acceleration time series, as shown in Figure 6.4-6. Softer tethers allow larger displacements between the top of the tethers and the seabed for the same stress levels in the tethers. By reducing the stiffness of the short tethers at the left end of the SFT, the frequency of the local eigenmodes around these tethers should decrease, which according to the frequency content of the acceleration time series used, as shown in Figure 3.2-2, should result in lower seismic excitation of these modes.

Although changing the material of the tethers may not be possible there are ways to accomplish a softer tether behavior. A soft bearing system may be installed at either end of the tethers, so that the bearing system and the tether acts as two springs in series, resulting in a softer total behavior of the tether system. This approach may however be quite costly. Another way to accomplish softer tether behavior is to use a better steel grade at these tethers, reducing the total area of the tethers and increasing the prestress for load bearing. Since the stiffness of tethers with same length and material are proportional to the cross-sectional area this would reduce the stiffness of the tether group. It is however worth noting that softer tethers may not be favorable for other loading scenarios not considered in this thesis, such as wave loading.

7.5 Seaquake

7.5.1 Numerical behavior

In order to model the seaquake phenomenon adequately, it is essential that the acoustic finite element model performs reasonably. The imposed boundary conditions as well as fluid and seabed properties are essential for the quality of the results.

The energy decay of pressure waves in water during a real seaquake scenario is highly uncertain. Each point at the seabed will act as a point source radiating a spherical pressure wave, resulting in a complex wave propagation in three dimensions. If the excited seabed is completely horizontal and of infinite extent being synchronously excited, this would result in a perfectly plane wave propagating in the vertical direction. For simplicity, it is chosen to approximate the incident wave as a planar wave, even though the behavior in three dimensions will be dependent on seabed topography.

To account for energy loss at the boundaries, infinite elements are applied, which at least in implicit time integration seem to dissipate virtually all energy from an incident wave at the bottom boundary in Figure 5.1-4. The infinite elements, as well as the behavior of the incident loading on the mesh, appears to be less accurate when using an explicit integration scheme.

In the final acoustic column model used to estimate seaquake loading the boundary at the seabed is approximated by modelling a segment of bedrock extended into the infinite domain with infinite elements. This is a physical representation in the sense that energy transmitted from pressure waves in the water into the bedrock will not return to the water column system. Due to the density and velocity of the bedrock being higher than those of the seawater, the seabed boundary should behave close to a hard-reflecting boundary, hence reflecting most of the wave back into the water domain with the equal sign according to chapter 2.2.6. The transmitted wave should lead to a loss of energy in the system. The results from the final model in chapter 5 captures the expected behavior of plane vertical wave propagation in a water column with the applied boundary conditions.

7.5.2 Seaquake uncertainties

As the acoustic finite element column model performs numerically well to the tested boundary conditions the numerical precision of the model is not the main contributing uncertainty in the modelling of the seaquake phenomenon. The governing uncertainties for the modelling of the seaquake phenomena comes down to three factors, namely the seabed boundary conditions, the applied loading, and possible structural interaction effects.

Seabed

In reality, there are sediments overlying the bedrock which will reflect some of the pressure waves, resulting in a more diffuse reflection than the one modelled in the analysis. There may also be stratification in the bedrock which can reflect a pressure wave propagating through the bedrock. The properties of the bedrock itself will also carry uncertainty, which will directly impact the amount of transmitted pressure wave from the water domain to the rock domain which disappears from the finite element system. For the properties of bedrock assumed in the acoustic modelling, roughly 80 % of the energy is reflected into the fluid domain, however for lower pressure wave velocities in bedrock this ratio could be significantly lower.

Seaquake loading

The loading applied in seaquake modelling, both in the acoustic modelling and in the analytical frequency, is derived from the earthquake time series velocities and the impedance relation given in chapter 2.2.6. This is equivalent to the earthquake seabed velocity being independent of the overlying water and eventual sediments at the seabed, which is not the case. The greatest uncertainty in the applied loading is the assumption of a vertical propagating wave disregarding seabed topography effects. An inclined seabed will give an inclined wave propagation, giving rise to the possibility of focusing effects where the pressures are amplified significantly, analogous to light through a magnifying glass. For example, a V-shaped seabed may result in amplified pressures when compared to an infinitely horizontal seabed. This effect is disregarded in the applied seaquake loading on the SFT by using a quasi-2D model which gives pressures along the SFT according to water depths.

Structural seaquake interaction

The pressures used to estimate seaquake loading are calculated both in frequency domain and acoustic time domain through wave propagation in fluid, disregarding the effects from interaction between the pressure waves and the SFT. In reality, the wave propagation will be coupled with the SFT and therefore the pressure acting on the SFT will be different. The net load on the SFT is calculated as the difference between the pressure at the top and bottom elevation of the SFT and multiplying with the cross-section width. This assumes that the pressures on top and bottom of the SFT is acting on the same area, equivalent to a quadratic cross section, while these points of a circular cross section are singular points with no area. The quadratic cross section approximation in this solution is expected to be conservative, as it will result in a higher approximated load on the SFT than accounting for a circular cross section. On the other hand, disregarding the structural interaction effect on the pressure wave may be non-conservative. When a pressure wave hits the structure, energy will be reflected and radiated, and thus the net pressure acting on the opposite side of the structure from the acoustic wave may be reduced compared to the pressures estimated from a model without a structure. This could potentially give higher net loads on the SFT.

7.5.3 Comparison between analytical and time domain seaquake

There are several similarities between the net pressures calculated from frequency domain and the numerical acoustic analysis shown in Figure 6.5-4. The peak values for the pressures are roughly the same and the periods between the peaks are comparable. Since the numerical acoustic model already has been validated to perform numerically well for given boundary conditions, this indicates that the acoustic finite element solution is trustworthy. The developed numerical acoustic model could therefore be suitable for expansion into a coupled acoustic-structural model.

The response comparison of the peak tether stresses of the SFT, shown in Figure 6.5-5, between the seaquake loading from both frequency and time domain are very limited as the duration of the analyses is below 10 seconds. Nevertheless, the peak responses from the two different seaquake approximations are quite similar. The peak acceleration response in Figure 6.5-6 for both seaquake representations are similar in magnitude, which both are significantly amplified from the initial response modelling results with no seaquake. This indicates that the response of the SFT should be of similar magnitude when applied loaded from the net seaquake pressures from the frequency domain solution and numerical acoustic time domain solution for the entire earthquake time series.

Due to the similarities in the responses, there is no reason to assume there is any accuracy gain from running the beam model response analysis with acoustic time domain seaquake loading over the analytical frequency domain solution, as long as no coupling between loading and structure, or a proper 2D pressure distribution along the SFT is introduced. Therefore, it is deemed reasonable to investigate the seaquake effects on the SFT though applying the full-length seaquake calculated from all acceleration time series through the analytical solution in frequency domain. This is nevertheless justifiable simply due to computational cost, since this is a relatively fast procedure, while the ABAQUS acoustic analysis is highly CPU costly, even for the short analysis of the strong motion part of the Friuli earthquake.

7.5.4 SFT response from seaquake loading

Previous reports suggest seaquake should be studied further, as it may give significant contribution on the SFT response in the vertical direction. The seaquake effect strongly depends on the accuracy of the seaquake modelling as discussed in the previous subchapters. It is worth noting that seaquake loading is a system dependent effect, and the response of a submerged structure may differ from that of a large floating structure or a ship.

The effect of the seaquake loading on the SFT response varies along the length of the bridge, which can be seen from the results in Figure 6.5-7. Some locations experience no amplification and even de-amplification in the peak stresses. This is most likely due to the seaquake loading being out of phase with the loading in the tethers from seabed ground motion.

For the response from Imperial Valley in Figure 6.5-7, the lowest value of the peak stresses in the shortest tether are moderately amplified when including seaquake loading, with an 8 % increase in the deviation from applied prestress for this tether. In general, the seaquake seems to give modest to little alteration in the values for the peak tether stresses. This contradicts some of the previous studies mentioned in the literature survey in chapter 1.4.3 that conclude that tether displacements, thus also stresses, of an SFT increase largely when subjected to seaquake. This may be due to differences in representation of the seaquake as the qualities of this loading remain quite uncertain. In addition, the design basis for the SFT including tether distribution, as well as modelling of seabed topography clearly impacts structural response.

The accelerations are considerably amplified by the seaquake loading to a larger extent than sectional forces in the structure. As seen in Figure 6.5-8, including seaquake results in a considerable increase in peak accelerations all along the bridge length. The accelerations along the beam are amplified compared to the PGA of the earthquakes when including seaquake, in contrast to the de-amplification observed when disregarding seaquake. The increased accelerations are due to the relatively high net pressures of the seaquake loading when compared to the oscillating mass of the structure. The peak seaquake loading is roughly 600 kN/m, which when compared to the distributed oscillating mass of the SFT including added mass of 600 000 kg/m should result in an acceleration of about 1 m/s^2 from seaquake alone. The peak acceleration of the SFT depends on to what extent the seaquake loading is in-phase with the accelerations induced by the excitation through the tethers. These results imply that increased accelerations of the structure due to seaquake may be an important aspect to consider when evaluating seismic response of a SFT.

7.6 Earthquake with high return period

The analyses of earthquakes with 10 000 year return period, with reduced structural damping ratio and including seaquake loading, led to considerably higher response than the initial model.

The acceleration response in Figure 6.5-10 show that since seaquake is included in this analysis, the peak acceleration response of the SFT is roughly 3 m/s^2 , which should be considered for traffic safety, but as this is a relatively low acceleration compared to gravity, the tether response may be of more significance.

The results for the peak tether stresses in Figure 6.5-9 show that no tethers have negative peak stresses, and they are thus constantly in tension, which is required for the system to remain in the linear regime. The lowest tension value in the most affected tether is slightly below 20 MPa, and the highest slightly below 200 MPa. For the purpose of comparison, possible effects from the wave passage effect or other dynamic loads were not included in this analysis. To avoid problems with low cycle fatigue and slack in the tethers, it should be avoided that the tethers reach yielding or compression respectively, as mentioned in chapter 3.1. The resulting stresses in the shortest tether for this analysis may provide a too small safety margin for the SFT, considering that no other dynamic loads are included in this analysis. If earthquakes with 10 000 year return period are set as design basis for this specific SFT, precautions may be necessary in order to avoid compression and perhaps also yielding in the stiffest tethers from seismic excitation.

8 Conclusions

In this MS thesis, an ABAQUS model was developed for investigation of effects from vertical earthquake ground motion on a submerged floating tunnel (SFT) proposal for the site of Bjørnafjorden. The SFT is modelled as a curved 3D beam model. The effects of seaquake loading, damping, torsion, earthquake wave passage and softer tethers are studied. The response from earthquakes with peak ground acceleration corresponding to return-period of 10 000 years for the site were also investigated. From the results, several conclusions can be made:

- Calculating added mass from a numerical potential theory panel model in WADAM resulted in an increase in added mass of roughly 10 % when compared to the analytical value for a circular cross section in infinite fluid. The added mass seems to be rather constant with respect to the frequencies of interest for vertical earthquakes on a SFT, and the assumption of constant added mass with respect of relevant frequencies for vertical excitation could then be evaluated as reasonable.
- Structural damping affects peak earthquake response of the SFT to a small extent which must be seen in context with the earthquake motion being both transient and irregular. Drag and radiation damping for the SFT's eigenperiods are small and safe to neglect for vertical seismic excitation of a SFT with vertical tethers.
- Curvature effects result in small torsional section forces for vertical earthquakes for low curvature, and may in such cases be disregarded. The 2D beam model show almost exactly the same eigenfrequencies as a 3D beam model. Tension in tethers due to torsional effects are negligible. Therefore, it would be sufficient to ignore torsional effects for studying vertical seismic excitation on a SFT when horizontal curvature is relatively low.
- Stress oscillations in the tethers appear to be critical for the SFT when subjected to vertical earthquake. The shortest, and thus stiffest, tethers close to the sides of the fjord attract the largest tether forces. Reducing the stiffness of these tethers significantly decreased the oscillations from the prestress value.
- Earthquake wave passage effect was considered in a simplified manner with only two propagation directions, but was shown to give moderate alterations of the SFT response in tether stresses, indicating that asynchronous ground motion may potentially have non-negligible effects on the stresses in the tethers.
- Seaquake loading was calculated both analytically in frequency domain and numerically in time domain without structural coupling. The acoustic behavior of water was captured in both models, but model refinement is needed to evaluate the effect of structural coupling on the seaquake loading.
- The SFT response to applied seaquake loading increases tether stresses only moderately, however accelerations on the SFT are significantly increased compared to neglecting seaquake loading.

- Tether stresses was shown to come close to compression when earthquakes with 10 000-year return period was used for excitation. If S235 steel or a lower steel grade is used for the tethers the stresses also come close to yielding. This may result in a low safety margin considering the uncertainty in the loading, that asynchronous effects are not extensively studied, and more significantly, no other dynamic loads are included in the response analysis. Precautions may need to be taken to avoid problems with low-cycle fatigue and/or local damage due to slack in tethers during earthquake excitations for the stiffest tethers.
- The overall response of the SFT to vertical earthquake excitation with return period of 475-years seem to have little effect on the structural response of the SFT, giving small sectional forces in the bridge girder and modest tether stresses. Such earthquakes will not be of critical importance in the design of the given SFT.
- Due to the stress oscillations, and thus forces in the tethers during seismic excitation, there may be capacity issues for tether anchors if suction anchors were to be used instead of rock piles as assumed in this thesis. This is especially worthy of considerations if earthquakes of 10 000 year return period are to be used as design basis.

8.1 Remarks and recommendations for further research

The seaquake phenomenon still seems somewhat uncertain. As it was pointed out in the literature survey, the effect has been shown to inflict severe damage to boats, and has been extensively researched for large floating structures. A submerged structure such as a SFT differs from a floating structure in the sense that the water above the structure will to some extent give an opposing pressure, reducing the net uplift force from the seaquake, while a boat will have no resistance in the vertical direction except its own weight. The seaquake loading effect is system dependent and will be affected by the presence of the structure in the fluid domain.

More research is needed to investigate seaquake on submerged structures; that is, through rigorous fluid-structure interaction analyses. A model similar to the ABAQUS acoustic model developed in this thesis should be extended to including the structure as rigid when calculating the seaquake loading. The ideal solution is expanding the model to a full coupled structural acoustic response analysis of an end section of the SFT or even the entire bridge if sufficient computational power is available. Another subject for further research is extension of the quasi-2D loading model to a proper 2D load model, accounting for the inclination of the seabed topography. This is possible to model in the ABAQUS numerical acoustic model in time domain. The 1D frequency domain acoustic model which was developed in this thesis in the frequency-domain can be extended to the 2D domain by accounting the variability of the base geometry. This should be analytically achievable for some idealized base geometries such as trapezoidal shapes of the seabed topography.

The effects of asynchronous ground motion was considered in a highly simplified manner, only accounting for the wave passage effect with two wave headings, which is a narrow and incomplete description of asynchronous seismic excitation. The results indicated that asynchronous ground motion could be of some significance to the response of the SFT, which should be investigated further.

References

- Ambraseys, N. (1985). A damaging seaquake. *Earthquake engineering & structural dynamics*, 13(3), 421-424
- Bungum, H. (2017). Jordskjelv – Store jordskjelv i Norge – Store norske leksikon. In S. N. Leksikon (Ed.), *STORE NORSKE LEKSIKON*. snl.no: STORE NORSKE LEKSIKON.
- Chandrasekaran, S. (2015). *Dynamic Analysis and Design of Offshore Structures* (Vol. v.5): Springer India : Imprint: Springer.
- Clay Mathematics Institute of Cambridge. (2017). The Millennium Prize Problems | Clay Mathematics Institute. Retrieved from <http://www.claymath.org/millennium-problems/millennium-prize-problems>
- Construction, & Design. (2017). *Earthquake: Body Waves & Surface Waves*. <http://www.constructionanddesign.com>. Retrieved from <http://www.constructionanddesign.com/2016/02/earthquake-body-waves-surface-waves.html>
- Crowe, C. T. (2009). *Engineering fluid mechanics* (9th ed., SI version. ed.). Hoboken, N.J: Wiley.
- Dassault Systmes Simulia Corp. (2017). Abaqus 6.13 Documentation. In D. S. S. Corp (Ed.), *Abaqus 6.13*.
- DNV. (2010a). ENVIRONMENTAL CONDITIONS AND ENVIRONMENTAL LOADS
- DNV. (2010b). Recommended practice, DNV-RP-C205.
- DNV. (2010c). *User Manual - Wadam*.
- Dunham, K. K. (2016). Coastal Highway Route E39–Extreme Crossings. *Transportation Research Procedia*, 14, 494-498 %@ 2352-1465.
- Faggiano, B., Panduro, J., Rosas, M. M., & Mazzolani, F. (2016). The Conceptual Design of a Roadway SFT in Baja California, Mexico. *Procedia Engineering*, 166, 3-12.
- Faltinsen, O. M. (1990). *Sea loads on ships and offshore structures*. Cambridge: Cambridge University Press.
- Hamamoto, T. (1995). Stochastic fluid—structure interaction of large circular floating islands during wind waves and seaquakes. *Probabilistic engineering mechanics*, 10(4), 209-224.
- Inoue, Y., Murai, M., Noma, Y., & Aoki, T. (2002). *A Frequency and Time domain study on Response Analyses of Large Floating Structures due to Seaquakes*.
- Kramer, S. L. (1996). *Geotechnical earthquake engineering*: Pearson Education India.
- Lee. (1995). Wamit Theory Manual.
- Long, M. (2014). Fundamentals of Acoustics (pp. [39]-79).
- Martinelli, L., Domaneschi, M., & Shi, C. (2016). Submerged Floating Tunnels under Seismic Motion: Vibration Mitigation and Seaquake effects. *Procedia Engineering*, 166, 229-246.
- Martire, G., Faggiano, B., Mazzolani, F., Zollo, A., & Stabile, T. (2010). Seismic analysis of a SFT solution for the Messina Strait crossing. *Procedia Engineering*, 4, 303-310.
- Mirzapour, J., Shahmardani, M., & Tariverdilo, S. (2016). Seismic response of submerged floating tunnel under support excitation. *Ships and Offshore Structures*, 1-8.
- NASA. (2017a). Euler Equations. Retrieved from <https://www.grc.nasa.gov/www/k-12/airplane/eulereqs.html>
- NASA. (2017b). Navier-Stokes Equations. Retrieved from <https://www.grc.nasa.gov/www/k-12/airplane/nseqs.html>
- Newman, J. N. (1977). *Marine hydrodynamics*: MIT press.
- Norsar. (2016, 2016-08-03). Jordskjelv i Norge. Retrieved from <https://www.jordskjelv.no/jordskjelv/om-jordskjelv/jordskjelv-i-norge/>

- Norsk Oljemuseum. (2017). Heidrun | Norsk Oljemuseum. Retrieved from <http://www.norskolje.museum.no/heidrun/>
- Norwegian Council for Building Standardization (NBS). (1998). Seismic Zonation for Norway: NORSAR and Norwegian Geotechnical Institute,.
- NPRA. (2012). Fergefri E39 - Delprosjekt Fjordkryssing. *Rapportar delprosjekt Fjordkryssing*.
- NPRA. (2015). *Bruprosjektering : [håndbok N400]* Håndbok (Statens vegvesen : online), Vol. N400(2015).
- NPRA. (2016). Høyringsframlegg: E39 Stor-Os, Ådland-Svegatjørn, Planomtale.
- Paik, I., Oh, C., Kwon, J., & Chang, S. (2004). Analysis of wave force induced dynamic response of submerged floating tunnel. *KSCE Journal of Civil Engineering*, 8(5), 543-550.
- Perotti, F., Shi, C., Domaneschi, M., & Martinelli, L. (2013). The non-linear dynamic response of submerged floating tunnels to earthquake and seaquake excitation.
- Romo, M. P., & Seed, H. B. (1986). Analytical modeling of dynamic soil response in Mexico earthquake of september 19th 1985. *Proceedings, International Conf. on the 1985 Mexico Earthquake, Mexico City*, pp. 148-162.
- Shengzhong et.al. (2016). Research on Type Selection of Submerged Floating Tunnel of Qiongzhou Strait. *Procedia Engineering*, 166, 307-316. doi:10.1016/j.proeng.2016.11.553
- Standard Norge. Design of structures for earthquake resistance. Part 1: General rules, seismic actions and rules for buildings.
- Uenishi, K., & Sakurai, S. (2013). On the dynamics of generation of seaquakes (pp. 341-346).
- USGS. (2017). Seismicity of the Earth Maps 1900-2013. Retrieved from <https://earthquake.usgs.gov/earthquakes/byregion/>

Appendix

Appendix

A. Eigenmodes initial model

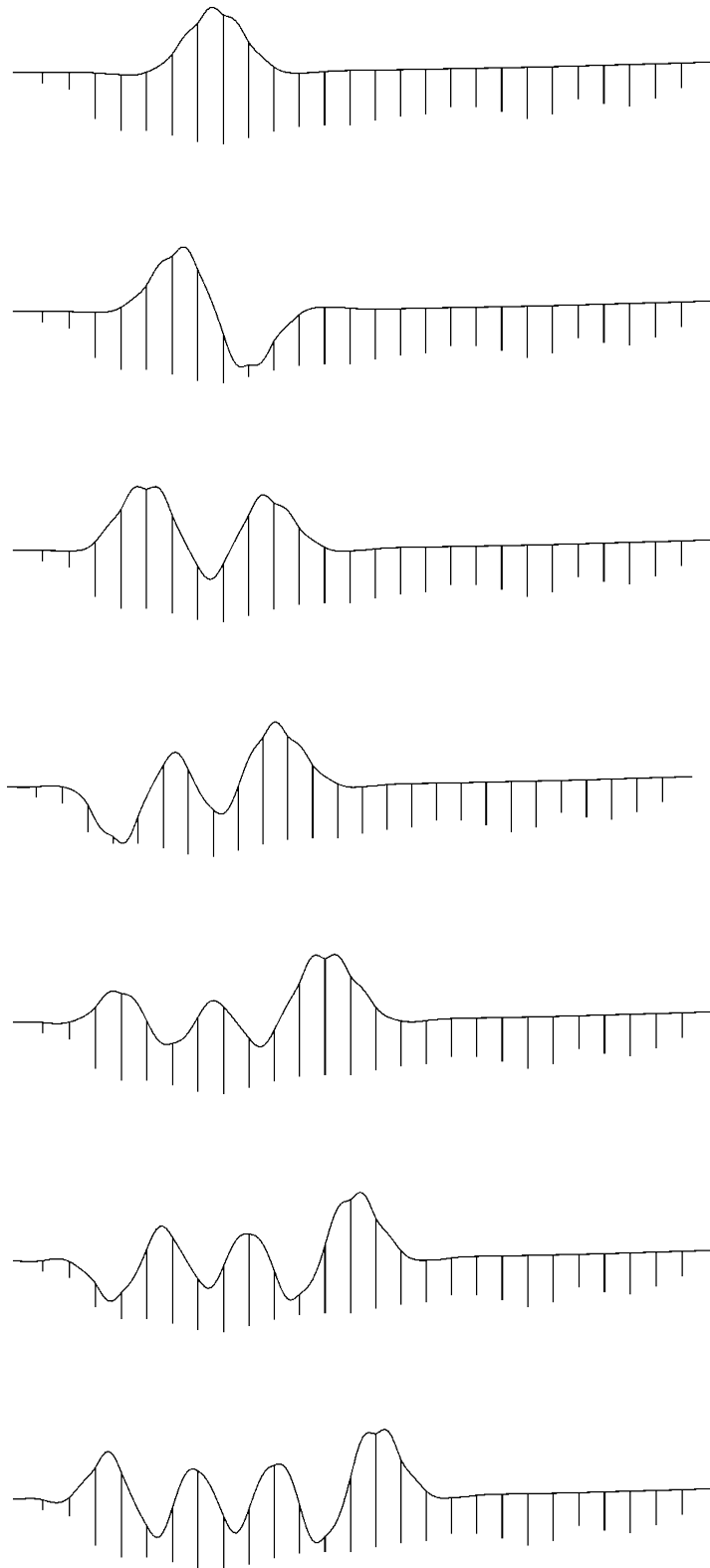


Figure A-1: Vertical eigenmode 1 (upper) to eigenmode 7 (lower) with corresponding effective mass given in Table 6.2-2.

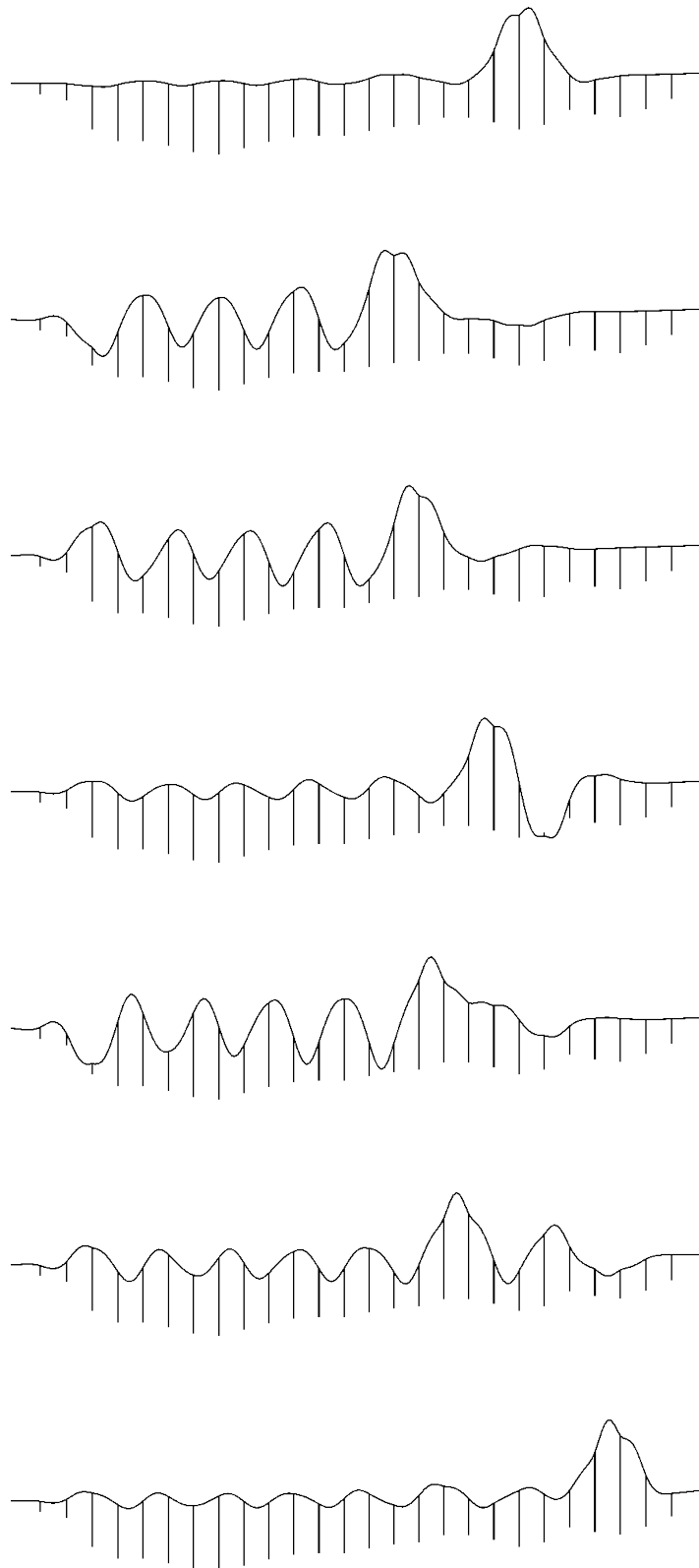


Figure A-2: Vertical eigenmode 8 (upper) to eigenmode 14 (lower) with corresponding effective mass given in Table 6.2-2.

Appendix

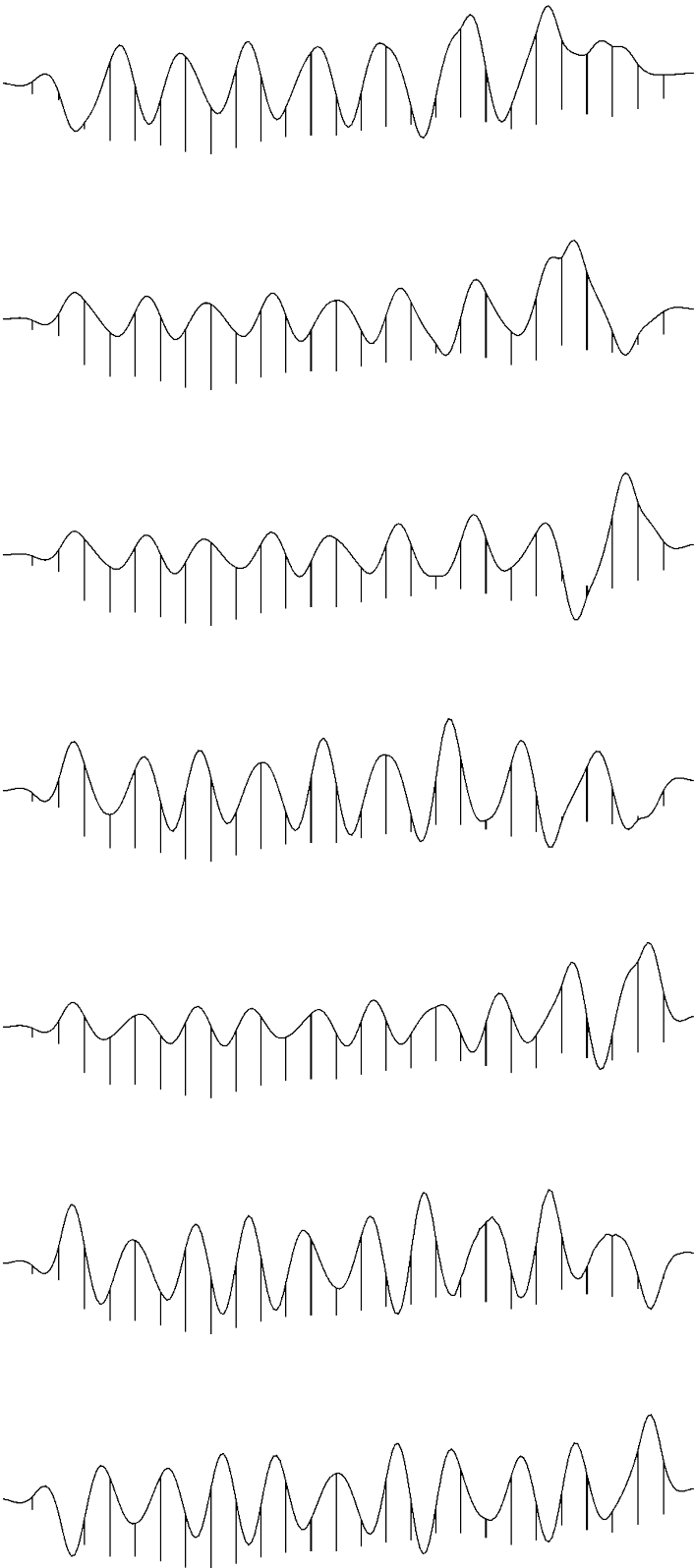


Figure A-3: Vertical eigenmode 15 (upper) to eigenmode 21 (lower) with corresponding effective mass given in Table 6.2-2.

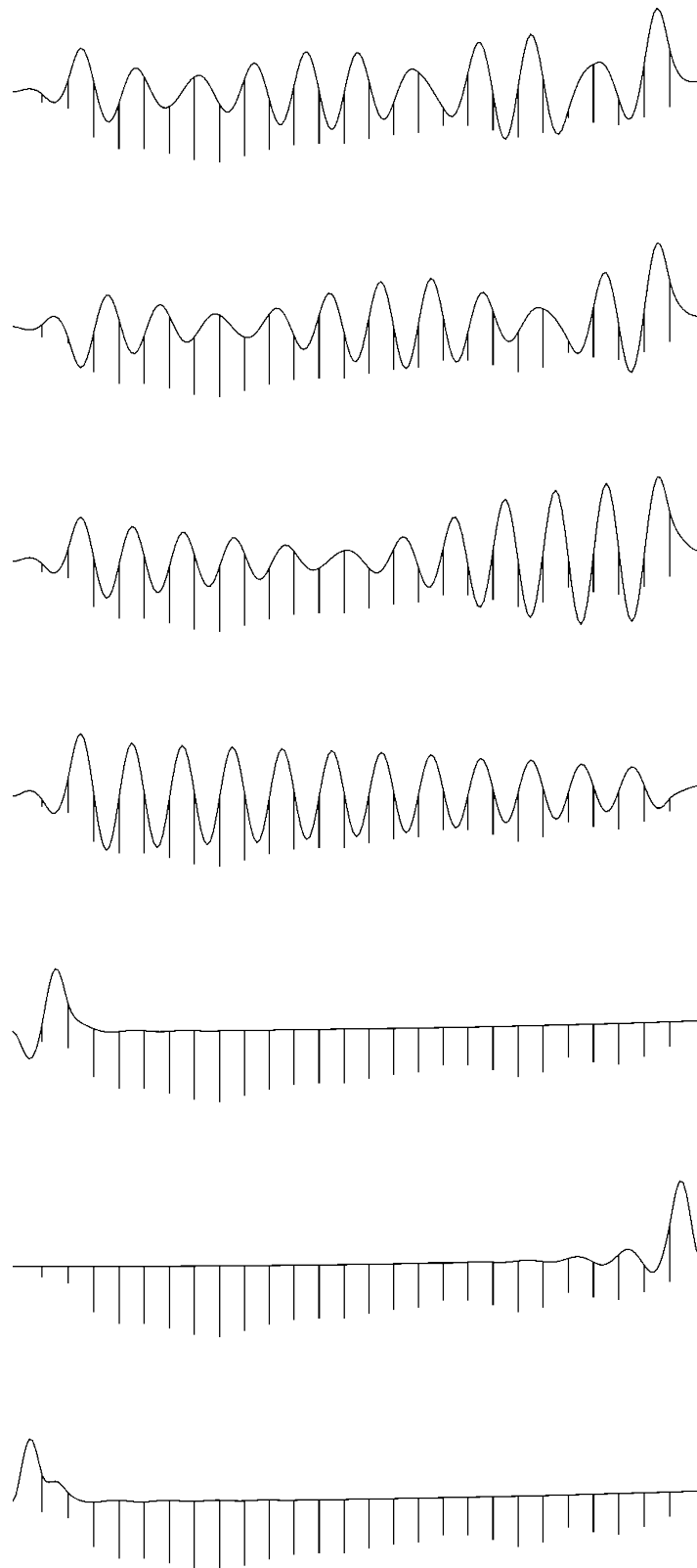


Figure A-4: Vertical eigenmode 22 (upper) to eigenmode 28 (lower) with corresponding effective mass given in Table 6.2-2.

Appendix

B. Net seaquake pressures for Friuli strong motion from analytic and ABAQUS numerical solutions

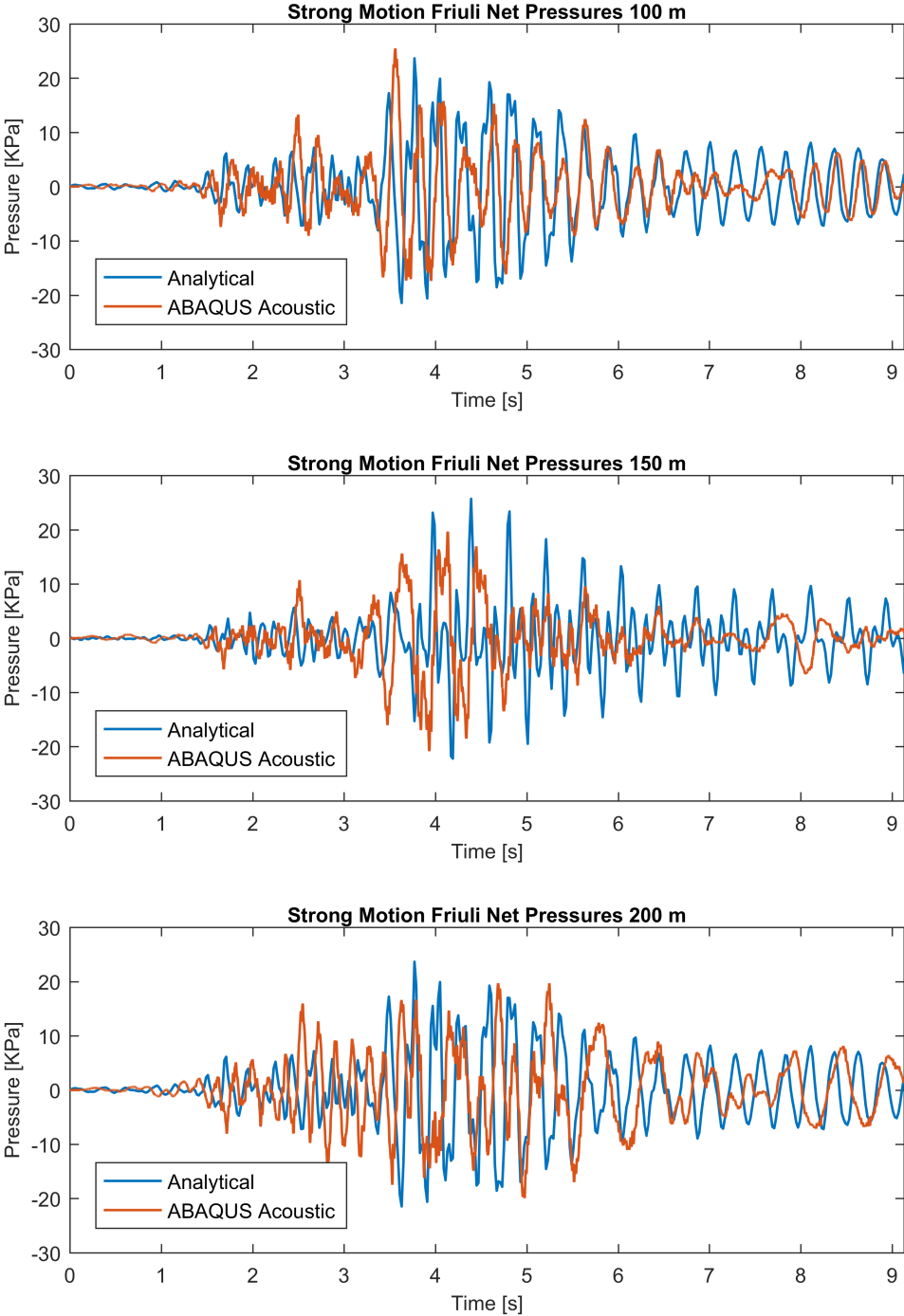


Figure B-1: Net seaquake pressures for Friuli strong motion from analytic and ABAQUS numerical solutions of depths 100 m, 150 m and 200 m.

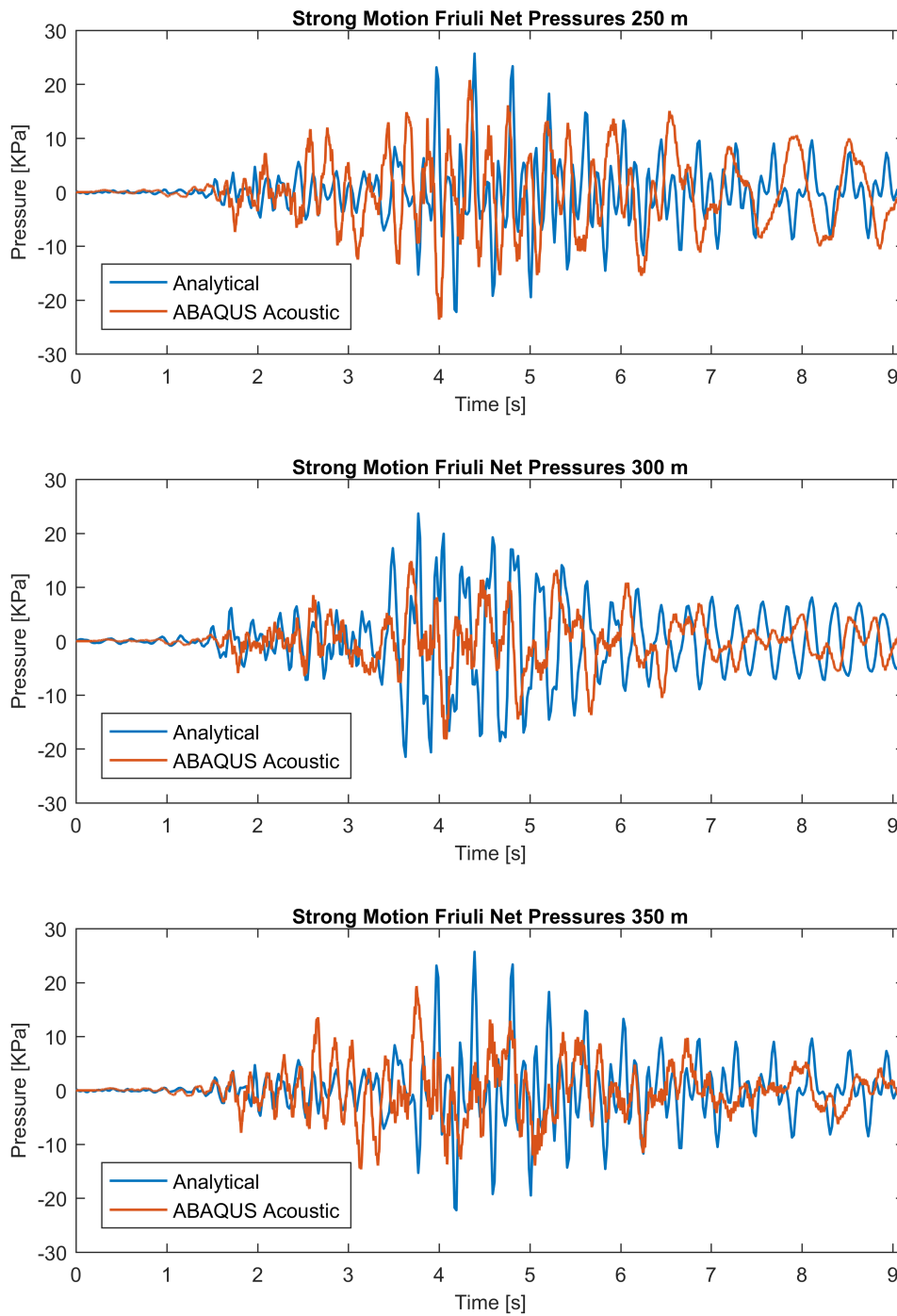


Figure B-2: Net seaquake pressures for Friuli strong motion from analytic and ABAQUS numerical solutions 250 m, 300 m and 350 m.

Appendix

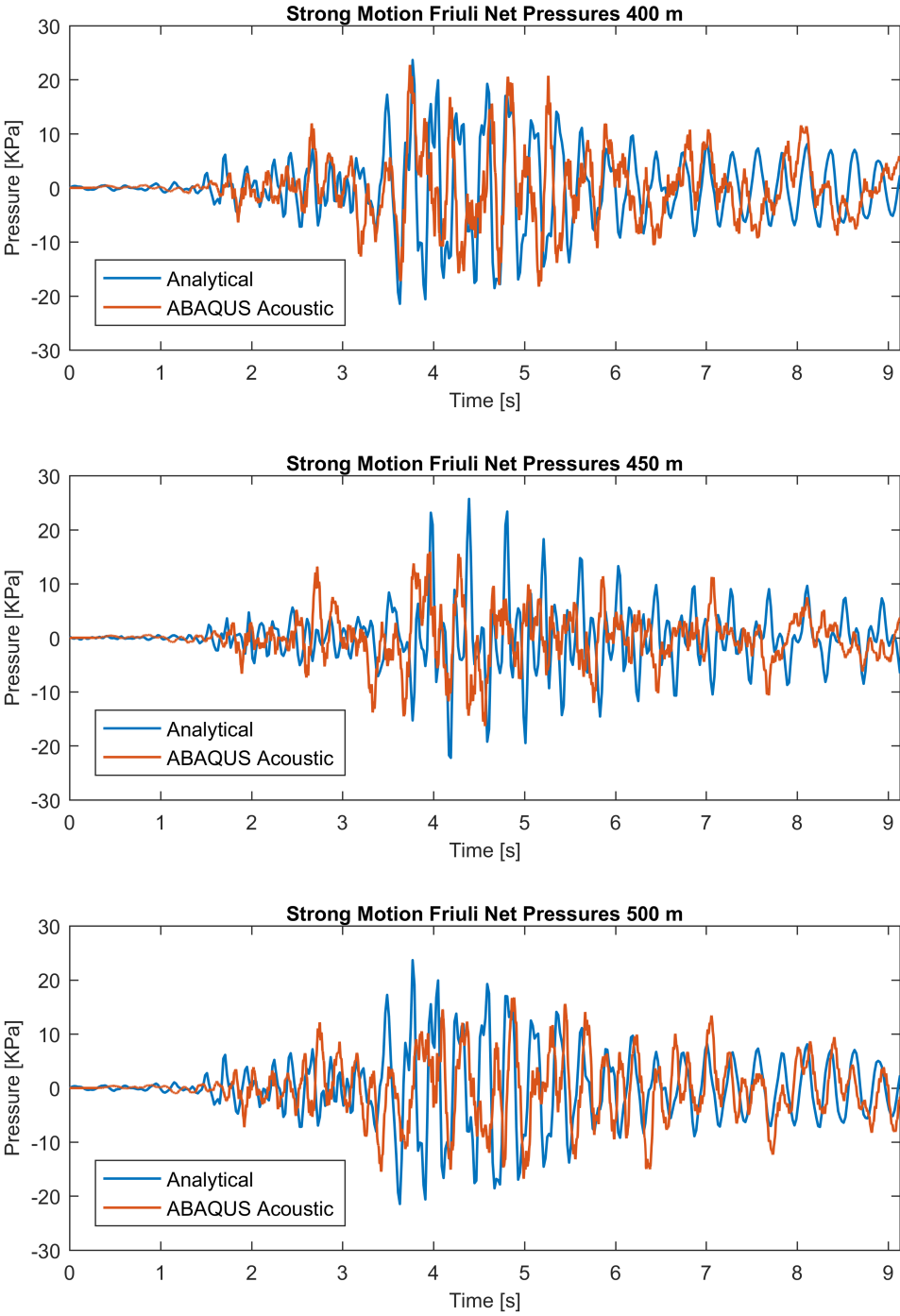


Figure B-3: Net seaquake pressures for Friuli strong motion from analytic and ABAQUS numerical solutions of depths 400 m, 450 m and 500 m.

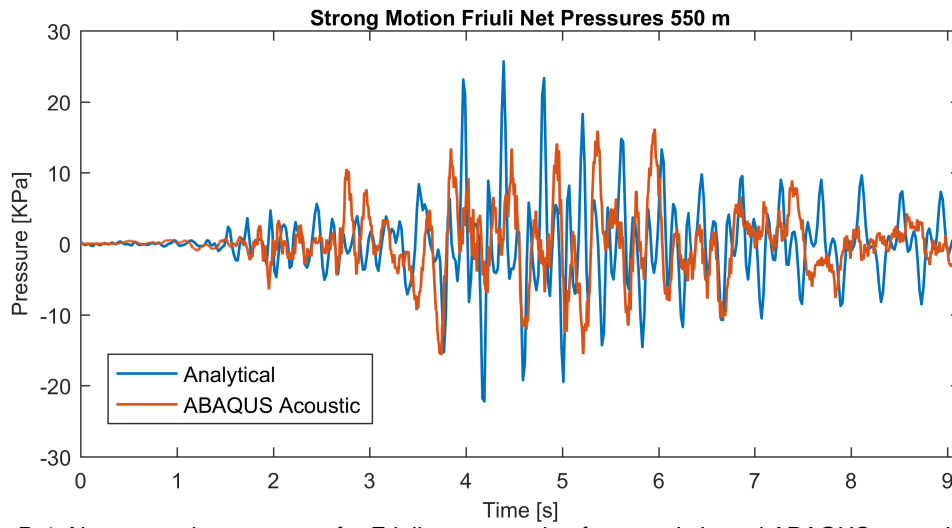


Figure B-4: Net seaquake pressures for Friuli strong motion from analytic and ABAQUS numerical solutions of depth 550 m.

Appendix

C. Net seaquake pressure for full Nahanni, Imperial Valley and Friuli time series from analytical solution in frequency domain

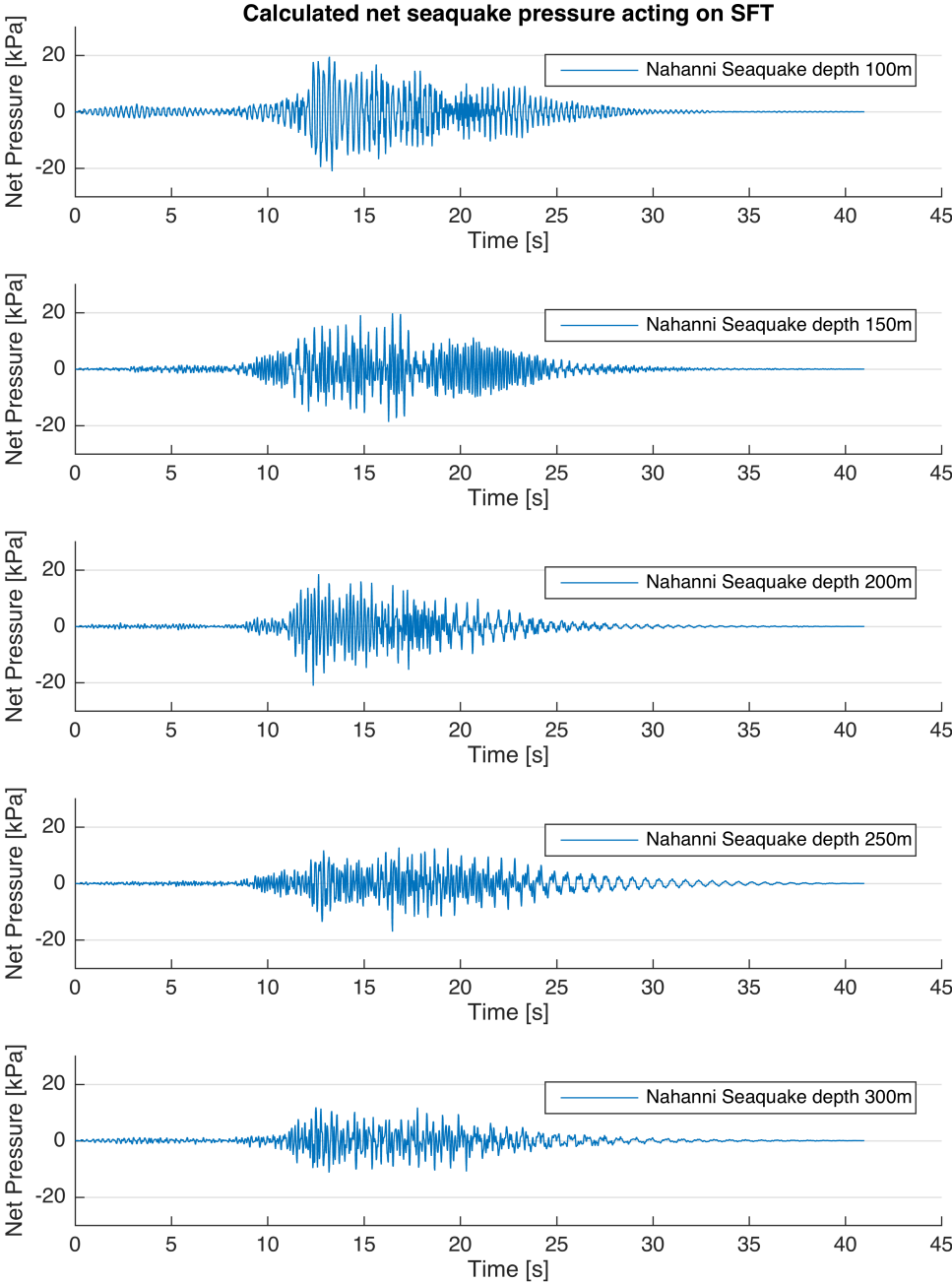


Figure C-1: Net seaquake pressures for Nahanni from analytic frequency domain solution with water depths from 100m to 300m.

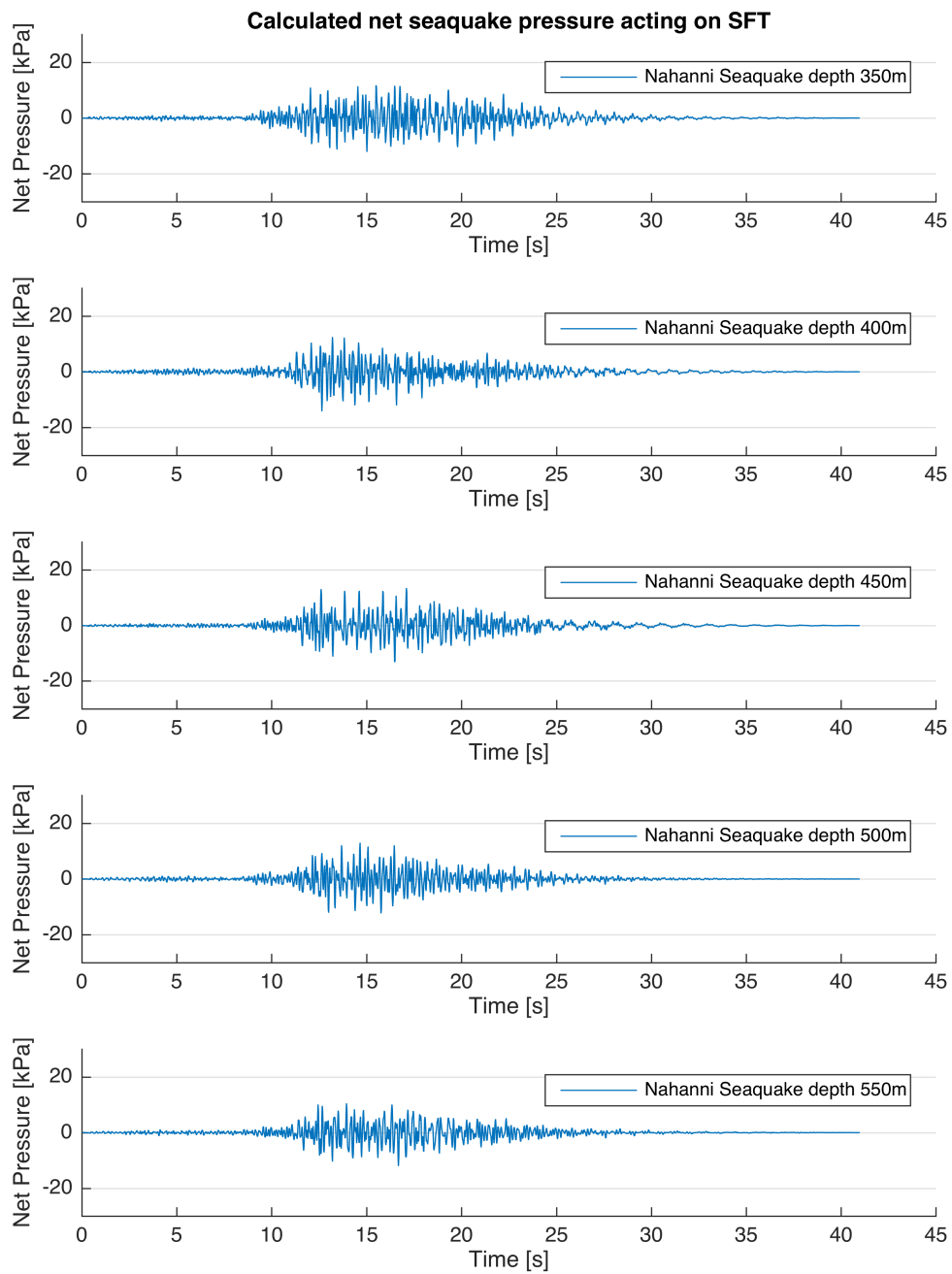


Figure C-2: Net seaquake pressures for Nahanni from analytic frequency domain solution with water depths from 350m to 550m.

Appendix

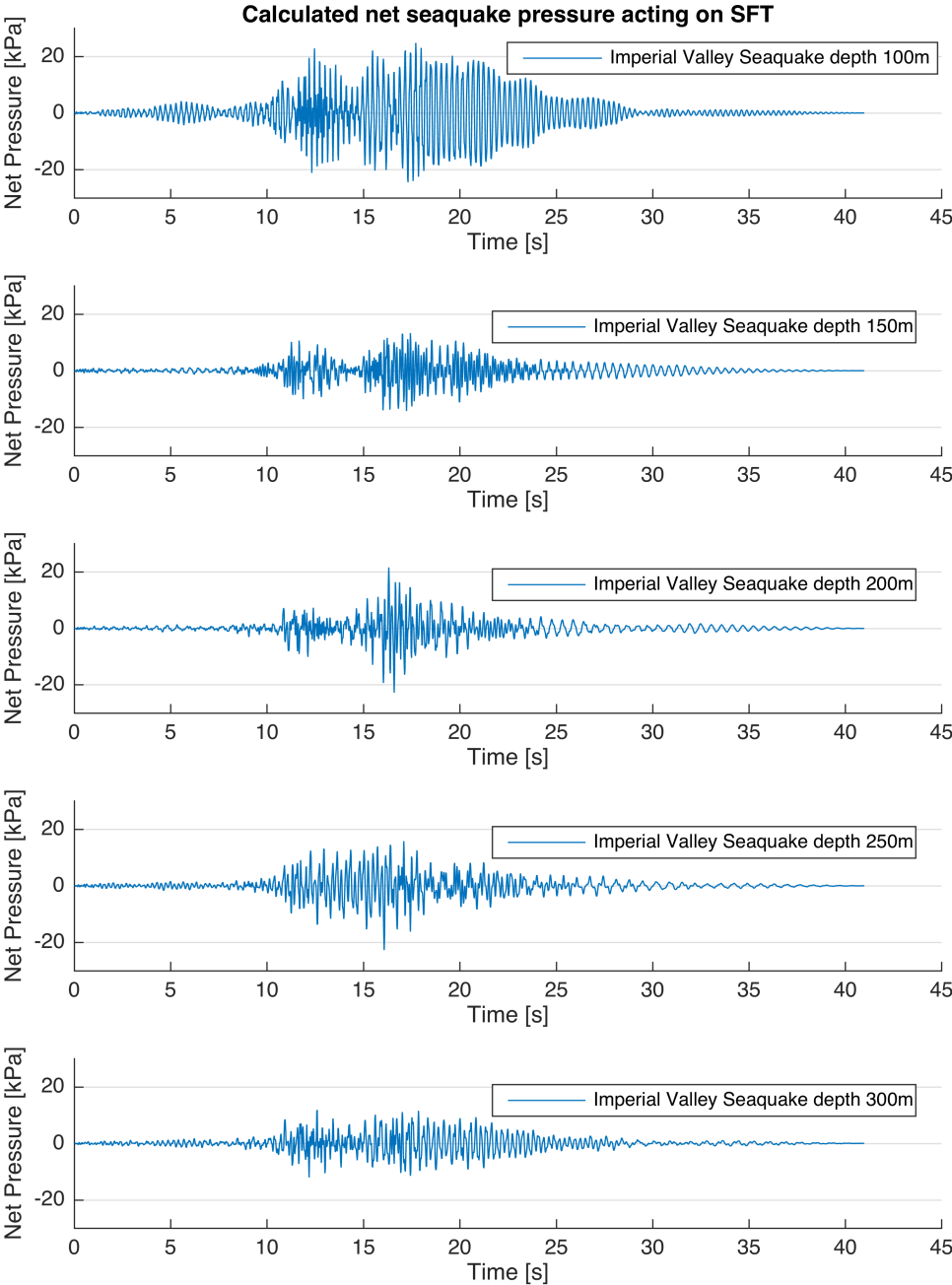


Figure C-3: Net seaquake pressures for Imperial Valley from analytic frequency domain solution with water depths from 100m to 300m.

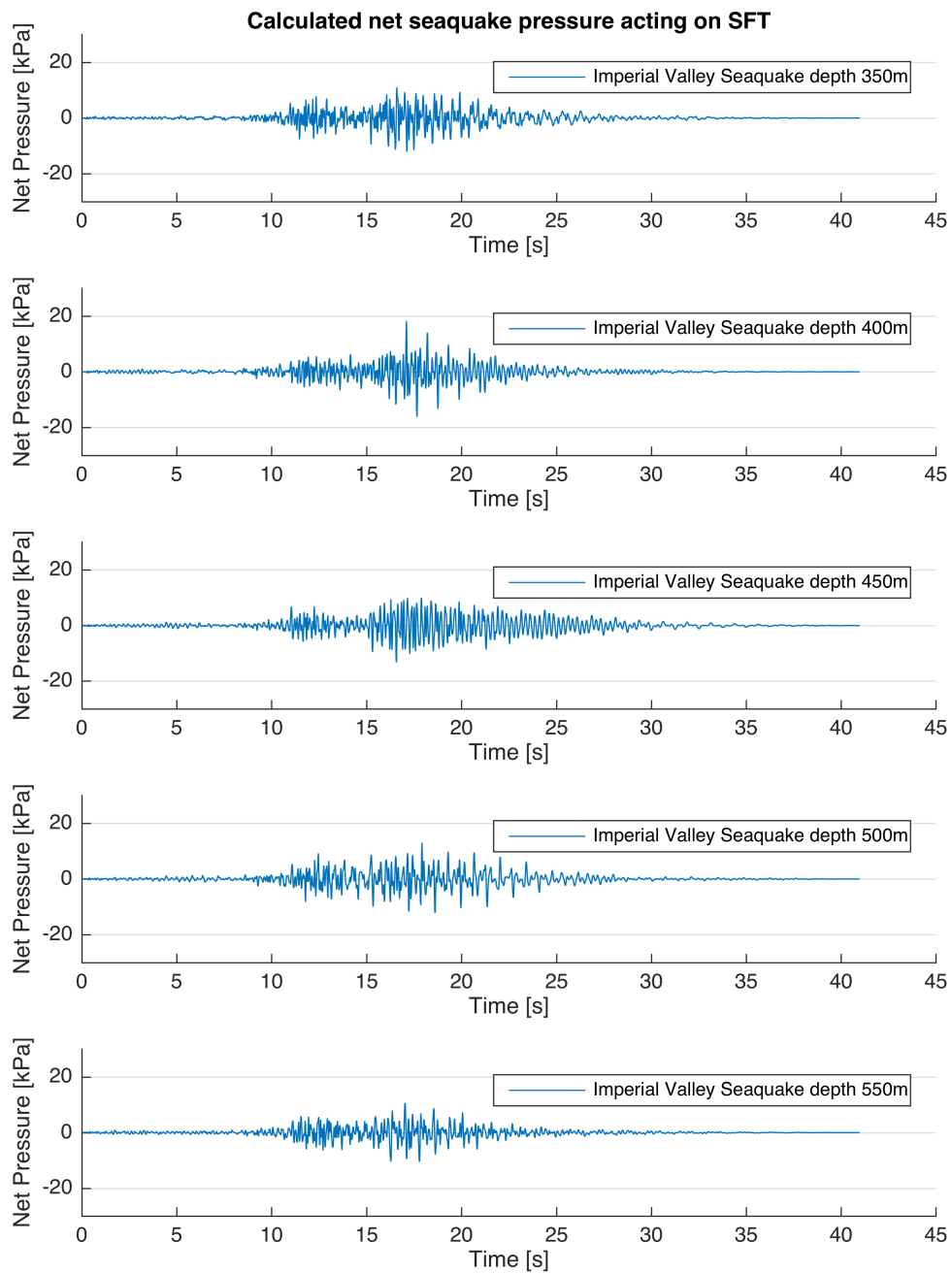


Figure C-4: Net seaquake pressures for Imperial Valley from analytic frequency domain solution with water depths from 350m to 550m.

Appendix

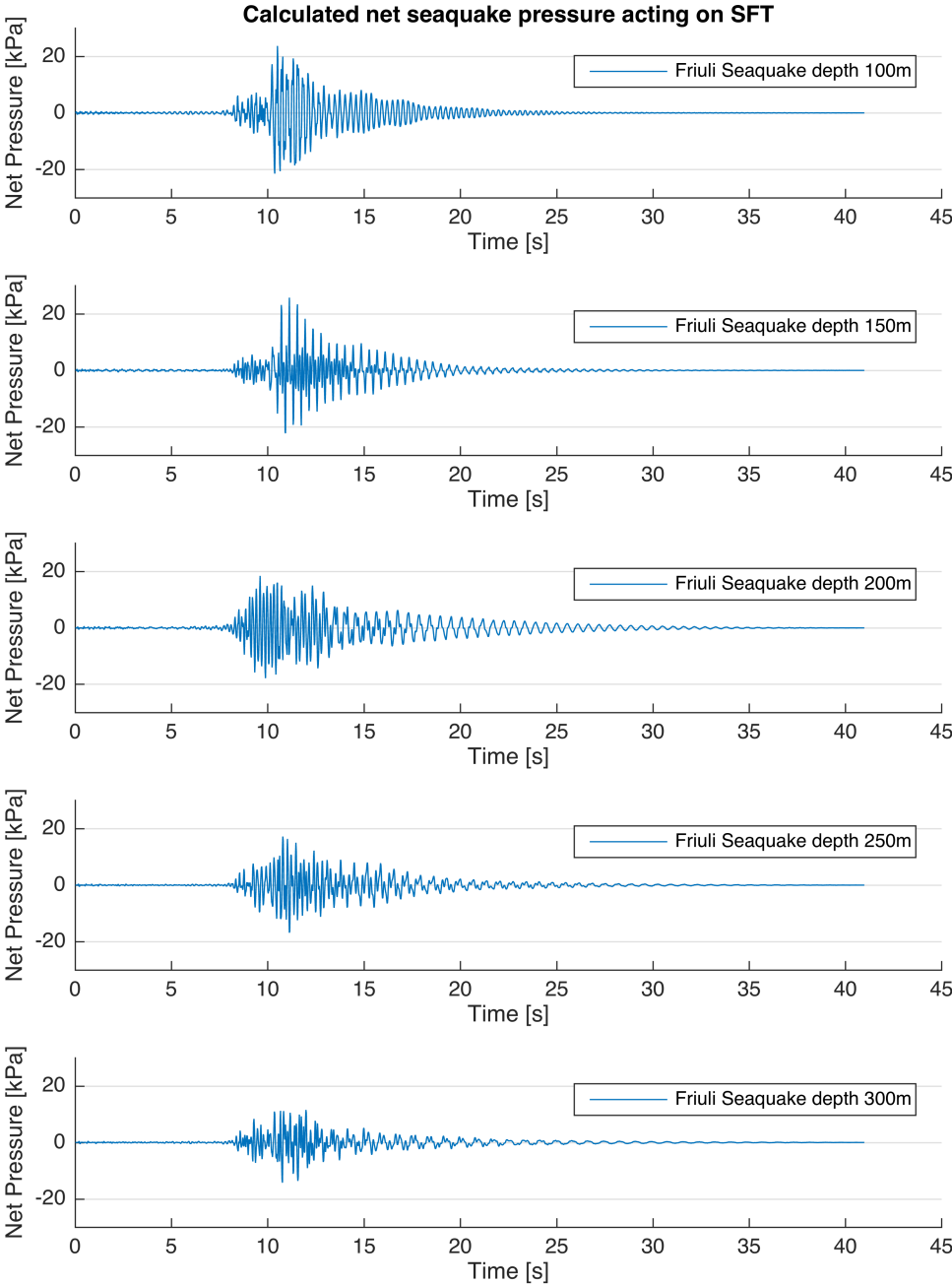


Figure C-5: Net seaquake pressures for Friuli from analytic frequency domain solution with water depths from 100m to 300m.

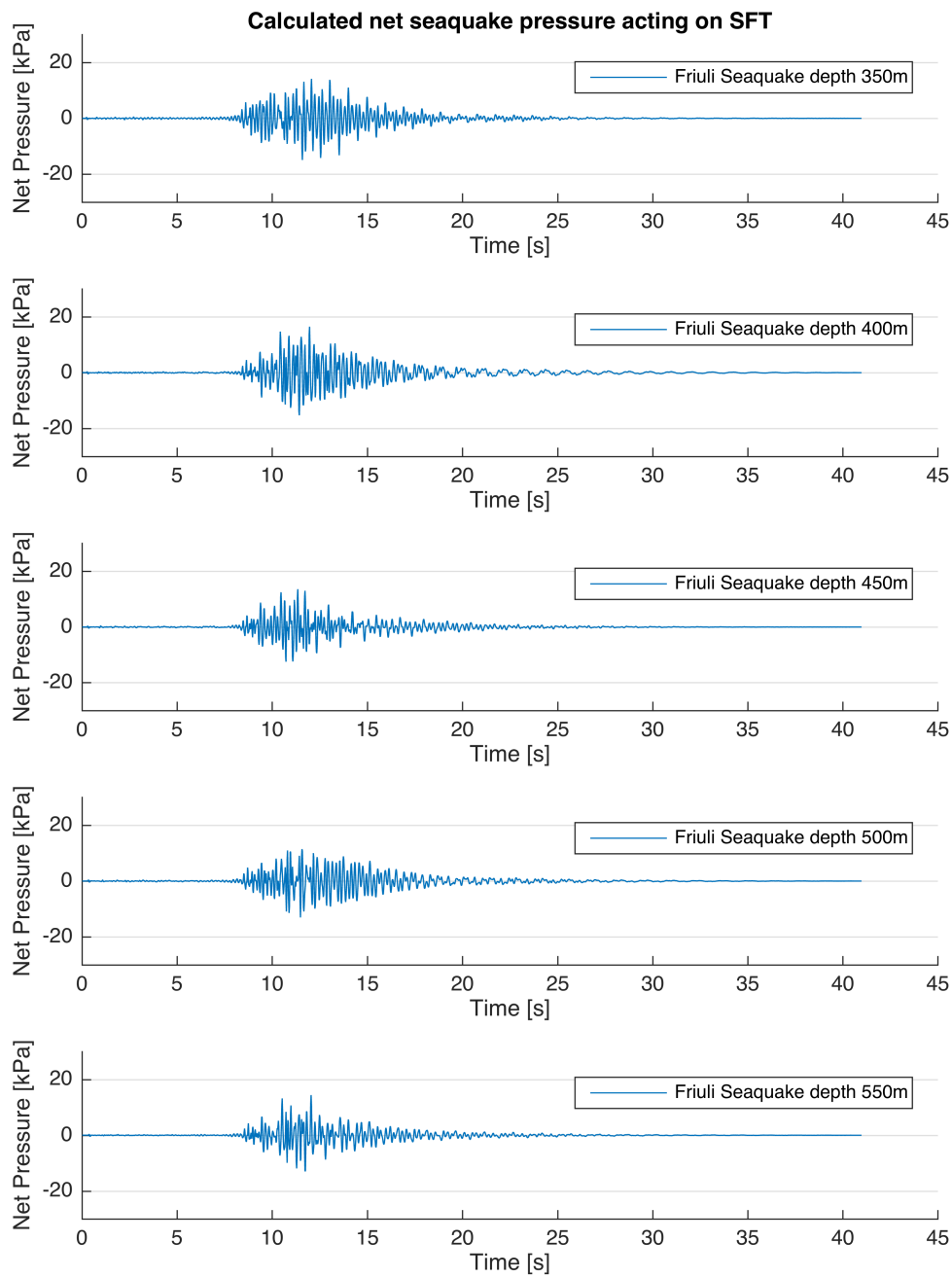


Figure C-6: Net seaquake pressures for Friuli from analytic frequency domain solution with water depths from 350m to 550m.